Université de Lille

Thèse de doctorat

L2EP Laboratoire d'électrotechnique et d'électronique de puissance de Lille

Portable instrument to rapidly assess mechanical properties of the skin

Système portable pour évaluer rapidement les propriétés mécaniques de la peau

Thèse de doctorat de l'Université de Lille
préparée au Laboratoire d'Électrotechnique et d'Électronique de Puissance (L2EP)

École doctorale des Sciences de l'Ingénierie et des Systèmes (ENGSYS-632)
Spécialité de doctorat: Génie électrique

Thèse présentée et soutenue à Lille, le 09/03/2023, par

YISHA CHEN

Composition du Jury :

Yves Perriard Professor, École Polytechnique Fédérale de Lausanne (Laboratory of Integrated Actuators)	Président
Micky Rakotondrabe Professor, Université deToulouse (ENIT Tarbes - INPT)	Rapporteur
Cédric Clévy Associate Professor, Université Bourgogne Franche-Comté (FEMTO-ST Institute)	Rapporteur
Betty Lemaire-Semail Professor, Université de Lille (L2EP)	Directrice de thèse
Frédéric Giraud Professor, Université de Lille (L2EP)	Co-directeur de thèse
Vincent Hayward Professor, Sorbonne Université (ISIR) | Actronika SAS, Paris	Co-directeur de thèse
Peter Worsley Associate Professor, University of Southampton (School of Health Sciences)	Invité

To my parents.

Résumé

Les escarres sont des maladies de la peau ou des tissus internes. Il est très couteux de traiter des escarres à des stades avancés. De plus, ce sont des pathologies très douloureuses, qui altèrent fortement la qualité de vie des patients atteints et peuvent même être fatals à un stade étendu. La détection précoce de ces escarres est donc primordiale pour pallier leurs effets. L'objectif de cette thèse est de développer une sonde portable pour mesurer les caractéristiques biomécaniques de la peau à risque « in vivo » et ainsi aider à prévoir l'apparition d'escarres.

Cette sonde est composée de deux benders piézo-électriques qui vont étendre la surface de la peau de manière contrôlée. La mesure simultanée de la force de réaction de la peau et de son déplacement est réalisée grâce à l'intégration de deux jauges de contrainte résistives. Les fonctions essentielles de la sonde, à savoir le contrôle du déplacement et l'acquisition des mesures mécaniques sont validées expérimentalement. Pour améliorer la mesure de la force, des stratégies de compensation de l'effet d'hystérésis sont présentées.

Les capacités de distinction de la sonde entre différentes surfaces sont tout d'abord testées sur des peaux artificielles dites « fantômes ». Ensuite, la sonde est appliquée pour mesurer les caractéristiques de peaux saines « in vivo », ceci sur différentes localisations. Il est montré que la sonde est capable de différencier ces localisations. La sensibilité et la fiabilité des paramètres mesurés par la sonde sont analysées en collaboration avec l'Université de Southampton. Des premiers résultats montrent que la sonde est capable de détecter des dommages de la peau dues à des dégradations mécaniques (arrachage d'un ruban adhésif par exemple).

Cette recherche peut donc contribuer à la détection précoce d'escarres mais également fournir des données sur la mécanique de la peau pour renseigner le développement de modèles.

Abstract

Pressure ulcers are a localized damage to the skin and/or underlying tissue. It's expensive to treat pressure ulcers at advanced stages. Moreover, they lower the patient's quality of life, being painful and life-threatening. Early detection is one of the solutions to prevent pressure ulcers. The objective of this thesis is to develop a handheld probe to measure skin biomechanics *in vivo* and to aid in the early diagnosis of skin at risk. This probe is composed of two piezoelectric bending actuators that stretch the skin surface and control the tip displacement. Simultaneous force and displacement sensing is achieved by integrating two pairs of resistive strain gauge sensors. The basic functions of the probe, simultaneous sensing and displacement control, are experimentally validated. Hysteresis compensation strategies are presented to improve force sensing. The discrimination capability of the probe is first justified with tests on phantom skins. Then, we apply this probe to measure skin properties *in vivo*. The anatomical-site-related differences are characterized by the probe. The reliability and sensitivity of the parameters derived from the probe are studied in a collaboration with the University of Southampton. Preliminary results show that the probe can detect skin damage caused by mechanical insult (tape strapping) with a reduced dynamic modulus. This research can contribute to not only the early detection of skin issues, but also provide valuable experimental data that can be used, for example, in the development of computational models.

Acknowledgments

I would like to express my deepest appreciation to my thesis director Pr. Betty Lemaire-Semail and my co-director Pr. Frédéric Giraud for involving me in this fascinating project. The completion of doctoral studies is inseparable from their constant guidance and support. Their immense knowledge and wealth of experience have inspired me throughout my studies. I'd also like to acknowledge the supervision of Pr. Vincent Hayward for all his guidance. He demonstrated scientific rigor from the subtleties, starting with the accurate use of mathematical notation. In addition, this endeavor would not have been possible without the generous support from the European Union's Horizon 2020 research and innovation program (STINTS project, No. 811965), which funded our research.

I also would like to express my gratitude to the jury members, Pr. Yves Perriard, Pr. Micky Rakotondrabe, Dr. Cédric Clévy, and Dr. Peter Worsley, for taking the time and effort to read and evaluate our work. Their insightful comments and suggestions from different perspectives have greatly enriched and deepened my thesis work.

I am deeply indebted to Michel Amberg. His wealth of experience and knowledge played an important role in the generation of the prototypes.

I would like to extend my sincere thanks to my colleagues in the STINTS project. It has been an exciting and unforgettable experience to work with you on this multidisciplinary project. Special thanks to Project Manager Dr. Simon Johnson and Coordinator Pr. Mike Adams, for their guidance and comments on our work. I am also grateful to our colleagues at the University of Southampton, for hosting us on the secondment.

Thanks should also go to the lab assistants, the librarians, print service technicians, and study participants, who helped, impacted, and inspired me.

Many thanks to Elis, thank you for always being there. You are my strong support. I am also grateful to my other colleagues at IRCICA, Anis, Angelica, Pierre, and Gérémie, who helped me quickly adapt to work and life here in the laboratory L2EP in France, and also to later joined members Detjon, Mondher, Rabii, and Milad..., for a cherished time spent together in the lab, and in social settings. I would also like to thank my friends, Dan, Yu, Yi, Yuan, and Qin. . . , for their company.

Lastly, I would like to mention my family. Thanks for their understanding and support, especially to Bu for the years of companionship and encouragement.

List of Symbols

T	stress
ε	strain
f	force
A_0	cross-sectional area
d	tested skin width
e_0	the thickness of skin
ΔL	displacement of skin
L	final length of the tested skin segment
L_0	initial length of the tested skin segment
t	time
$\boldsymbol{f}$	dynamic force
$\boldsymbol{v}$	dynamic velocity
$\boldsymbol{z}$	mechanical impedance
$\boldsymbol{S}$	strain tensor
$\boldsymbol{D}$	electric displacement vector
$\boldsymbol{T}$	stress tensor
$\boldsymbol{E}$	electric field vector
$\boldsymbol{s^E}$	elastic compliance matrix measured at a constant electrical field
$\boldsymbol{d}$	matrix of piezoelectric material constants
$\boldsymbol{\varepsilon^T}$	permittivity measured at a constant stress
V_{in}	input voltage
V_C	voltage across the capacitor
V_{si}	strain-induced voltage source
C_p	piezoelectric capacitance
Δ	nonlinear impedance modeling the nonlinear hysteresis
R_L	parallel resistor modeling current leakage.
q_p	charge on the capacitor ($q_p = C_p \times V_C$)

q_{in}	input charge
s	variable of Laplace
f_c	cutoff frequency
δ	tip deflection of piezoelectric bender
f_r	external force applied at the tip of piezoelectric bender, perpendicular to the bending beam
V	driving voltage (bender voltage)
d_{31}	piezoelectric coefficient
l	active length of the piezoelectric bender
w	width
h	piezo layer thickness
E	Young's modulus
M_p	uniform piezoelectric moment caused by the driving voltage
M_{tot}	total moment of a clamped piezoelectric bender
ϵ	strain at the surface of piezoelectric bender
I	moment area of inertia
x_1, x_2	positions of the strain gauge along x axis
l_s	center position of the strain gauges along x axis
ϵ_{ave}	average strain
$\epsilon_{\mathrm{free}}, \epsilon_{\mathrm{load}}, \epsilon_{\mathrm{diff}}$	strain when the bender tip is free and loaded at the same driving voltage ($M_p = cste$), strain difference $\epsilon_{\mathrm{diff}} = \epsilon_{\mathrm{free}} - \epsilon_{\mathrm{load}}$
R_1, R_2, G_1, G_2	components forming the Wheatstone bridge, two resistors (R_1 and R_2) and two strain gauges (G_1 and G_2)
V_{out}	output voltage
g	measured bending strain from strain gauges
$S_{\mathrm{dv}}, S_{\mathrm{df}}$	sensitivities of tip displacement to the driving voltage and to the external force
$S_{\mathrm{gv}}, S_{\mathrm{gf}}$	sensitivities of the gauge signal to the driving voltage and to the external force
$\widehat{\delta}, \widehat{f_r}$	estimated displacement and force
N	force factor of the piezoelectric bender
κ	gauge coefficient in blocking tests
PW	variable proportional to pulse width, used for DSP command
M	mass
D	damping
K	stiffness

ω_n	resonant angular frequency
Freq_n	resonant frequency
ξ	damping ratio
Q	quality factor
R_T	restoring force
z	imaginary hysteretic displacement
$\alpha, A, \beta, \gamma, n$	variables related to Bouc–Wen model
f^h	hysteretic force, with $f^h = (1-\alpha) Kz$
$V_{\mathrm{loaded}}, V_{\mathrm{free}}$	driving voltages needed to achieve the same displacement when the bender tip is loaded and free
K_P, K_I	proportionality constant and integral constant in PI control
τ	time constant
t_r	response time in closed-loop control
$\mathrm{OLTF}\,(s)$	open-loop transfer function
$\delta_{\mathrm{ref}}, \delta_{\mathrm{mea}}, \delta_{\mathrm{est}}$	reference displacement, measured displacement, and estimated displacement
H_A	area of the hysteresis loop
ε_0, σ_0, θ	the strain amplitude, the stress amplitude and the phase lag between stress and strain in dynamic mechanical analysis
E^*, E', E''	tensile dynamic modulus, storage modulus and loss modulus in dynamic mechanical analysis ($E^* = E' + iE''$)

Glossary

PVDF Polyvinylidene fluoride is a semi-crystalline thermoplastic fluoropolymer. It shows pieozoelectric properties.. 14

PZT Lead zirconate titanate is an inorganic compound with the chemical formula $Pb[Zr_xTi_{1-x}]O_3$ ($0 \leq x \leq 1$). 14, 18, 20

STINTS STINTS stands for Skin Tissue INTegrity under Shear. It is an European Union founded research programme under Horizon 2020 Framework. 1, 13, 17

Acronyms

CV coefficient of variation. 86, 87, 89, 91, 95, 96

DMA Dynamic Mechanical Analysis. 79, 102

FFT fast Fourier transform. 83, 86

LB Lower Bender. 42, 62, 63

LT Langevin Transducer. 17

MI mechanical impedance. 22, 23

MIP Mechanical Impedance Probe. 25, 27, 30, 44, 50–54, 56, 59, 79–81, 83, 87, 88, 91–93, 95, 98, 99, 102, 103, 105–107

NRMSE normalized root-mean-square error. 51, 52

PI proportional-integral. 73, 76

PU Pressure ulcer. 1–3, 5, 12, 13, 22, 107

PWM pulse width modulation. 36, 38

RMSE root-mean-square error. 70

SCI Spinal Cord Injury. 13

SD standard deviation. 86, 89, 90, 95

SEM Sub-epidermal Moisture. 13

UB Upper Bender. 42, 62, 63

Contents

List of Figures

List of Tables

General introduction

Motivation

Pressure ulcers (PUs) (also known as pressure injuries, decubitus ulcers) are a worldwide critical health issue. PUs are defined as a local damage to the skin and/or underlying tissues. They are caused by prolonged exposing to pressure and/or shear force, usually over a bony prominence, as shown in Fig. 1. The common sites involve the sacrum, the back, the buttocks, the heels, the back of the head, and the elbows [1]. Bader [2] has summarized several pathogeneses of the PUs, including pressure-induced ischaemia, impaired interstitial and lymphatic flow, ischaemia-reperfusion injury associated with load removal, cell and tissue deformation. The most vulnerable populations are people with impaired mobility or sensation, who are generally bed- or wheelchair-bound. Poor nutrition may increase the risk of ulceration, which is a common issue both for immobilized and elderly people. Generally speaking, anyone exposed to sustained pressure is susceptible to PUs, not limited to elder but also children and neonates [3]. Fig. 2 depicts PUs at different stages [4]. PUs are very painful and lower the quality of life. Moreover, on the economic point of view, it was reported that the total cost of treating PUs was up to £2.1 billion annually in the UK [5]. A following study showed that treating a PU at Stage I cost £1214, and it cost 10 times more to treat a PU at Stage IV, about £14 108. PUs in advanced stages cost more since they need longer time to heal and usually come with higher incidence of complications [6]. In all aspects, for individual or societal, the prevention of PUs is prior to treatment. As suggested by its etiology, repositioning of the patients to avoid prolonged pressure can help to prevent PUs. Specialized support surfaces and adequate nutrition are other two aspects related to the management of PUs [4].

The studies on PUs have received increased interests. From the academia point of view, the publication has increased more than four times from 1999 to 2022, based on a topic research with "pressure ulcers*" in Web of Science Core Collection. Most of the publications are from the USA, England and Peoples R China, with research areas covering surgery, dermatology, nursing, general internal medicine, and engineering, etc. STINTS is an European Union funded multi-discipline project to study skin tissue integrity. It is aimed to understand the biomechanical and biochemical pathologies of skin integrity losing. Consequently, practical solutions can be exploited to reduce the huge societal and financial costs of PUs. The main research tasks in this project are: designing more effective preventative aids (mattress, cushions, etc), developing early

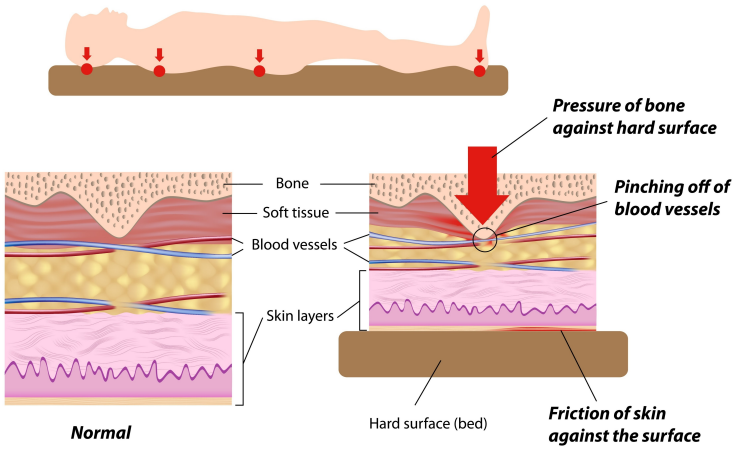

Figure 1: Etiology of pressure ulcers [7].

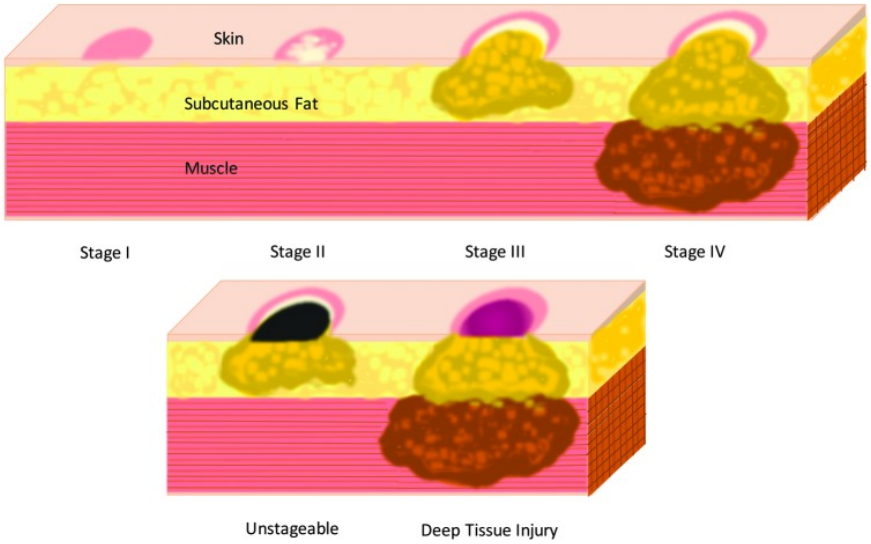

Figure 2: Illustration of different stages of pressure ulcers. From *left* to *right*. *Top diagram* showing pressure ulcers Stage I: skin intact. Stage II: partial skin loss. Stage III: full-thickness skin loss, subcutaneous tissue exposed. Stage IV: muscle, tendon, bone or organs exposed. *Bottom diagram* showing unstageable pressure ulcer with tissue damage hidden from observer by eschar over entire wound. Deep tissue injury hidden from observer by intact skin appears as a bruise from above [4].

stage diagnostic tools (biomarks, sensors), and treatment (debridement, utilizing ultrasound for therapy), taking benefits from the thorough understanding to etiology. Based on our expertise in L2EP (Laboratory of Electrical Engineering and Power Electronics), we are directing towards the development of early detection/diagnosis tools. By that way, we will take benefit of the skills of the research group in the design and control of piezoelectric actuators.

Previous work in [8] demonstrated the ability to distinguish skin responses at different anatomical locations, using two piezoelectric benders. We hypothesize that changes in skin biomechanics may indicate the development of PUs. To detect these mechanical changes, accurate measurements of the skin response (force and displacement) must be realized, with a “standalone" device if we want to easily apply this approach to a wider range of patients, located in a hospital or at home. The idea is to use an actuator-sensor system, consisting of two piezoelectric benders and a set of resistive strain gauges.

Objectives

To aid in the early detection of skin disease (PUs), the objectives of the thesis are:

- to develop a handheld probe to measure mechanical properties of the skin;
- to quantify the mechanical properties of the skin;
- to investigate the relationship between altered skin biomechanics and damaged skin.

With the light of early detection, prevention initiatives can be taken to prevent the onset of PUs or stop them from developing into advanced stages.

Thesis layout

This PhD thesis is organized as follows:

Chapter 1 presents the state of the art and the positioning of the project. First, the characterization of skin biomechanics is reviewed, which defines the general specification of our probe and provides references for *in vivo* testing. The efforts in early detection of PU are stated. This is followed by a review of piezoelectric materials and their applications to skin/soft tissue measurements. The constitutive equations and nonlinear behavior of the piezoelectric materials are also described.

Chapter 2 demonstrates the design of the mechanical impedance probe, based on two piezoelectric benders and a set of strain gauges. The model for simultaneous sensing of force and displacement is established. This sensing model is validated through experiments. Furthermore, we verify the discrimination capability of the probe with the tests on phantom skins.

Chapter 3 focuses on dynamic modeling to implement closed-loop control. Two hysteresis compensation strategies are presented to improve force sensing. The performance of the whole system (on estimator and controller) is evaluated by applying a spring load to the bender tips.

Chapter 4 shows the *in vivo* human skin tests performed with the probe. Two main studies are presented to illustrate the capabilities of the probe, in terms of skin biomechanical characterization. The first one deals with the intact skin of the inner forearm and the palm of the hand, while the second one tends to clinical conditions and proposes first results on skin insult discrimination.

Chapter 1

Piezoelectric materials and applications in soft tissue/skin characterization

1.1 Introduction

Characterization of skin bio mechanics is meaningful to deepen our understanding on skin behavior. Mechanical properties also show potential applications as evaluation indicators of skin/soft tissue states (aging, edema...). The clinical significance has been established between variations in mechanical properties and diagnosis. To prevent PUs, we dedicated to early detection of skin at risk. Our objective is to develop a portable probe to rapidly assess skin mechanical properties *in vivo*. This chapter gives the state of the art, which can be separated into two parts.

In the first part, we give general information on skin mechanical properties and conventional characterization approaches (tension, indentation, suction, and torsion). The typical physical quantities related to the mechanical properties of the skin (stress, strain, and Young's modulus) and quantification methods are introduced with examples. *Ex vivo* tensile tests are presented to explain the underlying mechanism of "J-shape" curve for skin in response to uniaxial tensile. This part is ended up with current efforts in early detection of PUs. Studies working on electrical and mechanical variations associated with the development of PUs are reviewed. It is noticed that these works are still in progress, and further investigation and more clinical evidence are required to realize early detection.

Inspired by a previous work [8], we plan to develop an actuator-sensor system based on piezoelectric benders and strain gauges to measure the skin mechanical behavior. In the second part, the working principles of piezoelectric materials and applications are presented (specially in soft tissue/skin characterization). The applications of piezoelectric actuator/sensor can be divided into two types based on the working modes, quasi-static and resonant. Examples are given to explain how to extract skin properties from these measurements. However, the application of piezoelectric actuators are suffering from inherent nonlinearities, which have an impact on the measurements. So we discuss about these nonlinear behav-

iors, especially hysteresis and creep effects. Moreover, the drive/control of piezoelectric actuators can be either in voltage approach or in charge approach, which is important for nonlinearity influence. The benefits and disadvantages of these two drive methods are further explained through a lumped parameter model. Last, we make our proposal using two piezoelectric bending actuators and a set of strain gauges, to characterize skin properties by tangential traction. A series of technical parameters (such as force or stress range, displacement or strain range, and excitation frequencies) are introduced and explained from related references.

1.2 General knowledge on skin: structure, function, and properties

Skin is the largest organ of human body. It has multi functions to meet the necessities of our daily life, such as sensation of the external world, barrier function between body and environment, protecting internal organ from damage (mechanical, thermal, and physical injury, and hazardous substances) and infection [9]. Meanwhile, it regulates our body temperature and prevents water loss. In general, skin can be separated into three layers, the outermost layer epidermis, the middle layer dermis, and the deepest layer hypodermis, as illustrated in Fig. 1.1. The whole thickness of skin is around $4\,\mathrm{mm}$ and it varies according to anatomical sites. Epidermis is relatively thin, its thickness is generally around $0.07\,\mathrm{mm}$–$0.12\,\mathrm{mm}$. While dermis is much thicker, $1\,\mathrm{mm}$–$2\,\mathrm{mm}$ in average [10].

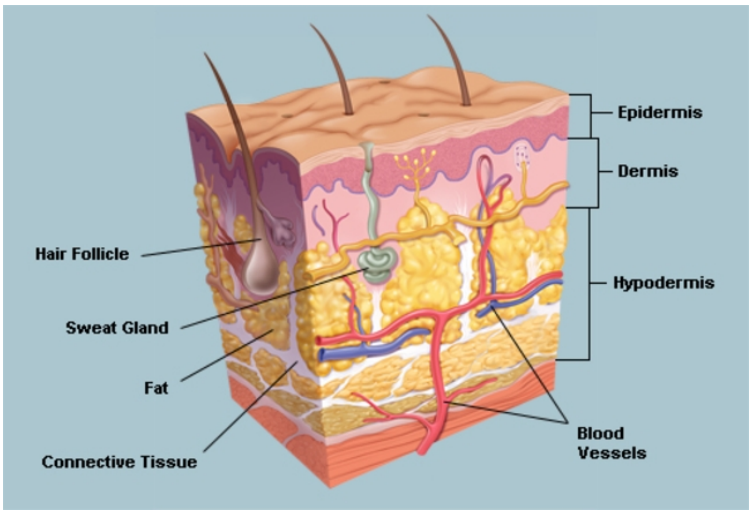

Figure 1.1: Skin structure [11].

Skin's function is determined by its structure and composition. The uppermost layer of epidermis, i.e., the stratum corneum layer accounts for the barrier function of skin. Resistance to friction is mainly related to the epidermis. Dermis mostly contains randomly oriented collagen and elastic fibers, which are surrounded by a viscous matrix, named as the *ground substance*. Dermis layer accounts for extensibility of skin. As for skin response to lateral compressive loading, both epidermis and dermis are counted [10].

Skin is known as a *non-homogeneous, anisotropic, non-linear viscoelastic multi-component* mate-

rial [10]. In the following section, research on skin properties are reviewed, focusing on the characterization of mechanical properties.

1.3 Characterization of skin mechanical properties

Researchers are interested in skin response with aging or when exposing to loading force. To maintain skin health, it is essential for us to understand the underlying mechanism of skin subject to deformation. The typical tests applied in skin characterization include continuous stretching, cyclic loading, step strain (for stress relaxation), and step stress (for creep). The nonlinear elasticity and viscoelasticity of skin can be characterized through these tests. Skin characterization is generally classified into two categories depending on the testing environment: *in vivo* tests and *ex vivo* tests. *In vivo* tests mean that the experiments are performed directly on the subjects, while *ex vivo* tests are conducted on samples excised from the subjects. It is known that *in vivo* measurements provide us more realistic results, with the influences from adjacent organs in the body considered. Extensometry (tension), indentation, suction, and torsion tests are four common tests to identify skin properties *in vivo* [12]. The force directions associated with each mechanical test are shown in Fig. 1.2. Different testing methods and studied skin properties are summarized in Table 1.1. In the following parts, details about each test are introduced, including the principles, the tools, the issues, and the studied skin properties.

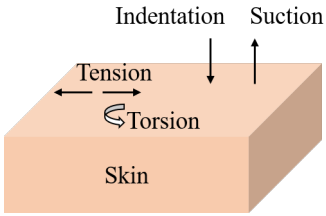

Figure 1.2: Four common types of force applied to the skin surface in mechanical testing. In plane: tension and torsion. Out of plane: indentation and suction. Arrows indicate direction of force.

Table 1.1: Common methods used to measure mechanical properties of skin.

Methods	**Properties or parameters**
Extensometry	elasticity (Young's modulus), viscoelasticity, anisotropy, extensibility (strain threshold)
Indentation	indentation force–indentation depth curve, elasticity (Young's modulus)
Suction	viscoelasticity, age-related parameters
Torsion	elasticity (shear modulus and Young's modulus)
Tensile tests (*ex vivo*)	stress–strain curve, elasticity (Young's modulus)

1.3.1 *In vivo* tests

1.3.1.1 Extensometry

Extensometry usually involves two tabs/pads/jaws attached to the skin. Lateral traction is applied to the skin, either by moving only one tab [13], or the two jaws simultaneously in the opposite direction [14]. An extensometer held by an articulated arm is shown in Fig. 1.3a [15]. A following prototype Fig. 1.3b can work without stand with an ultra-light extensometer [16].

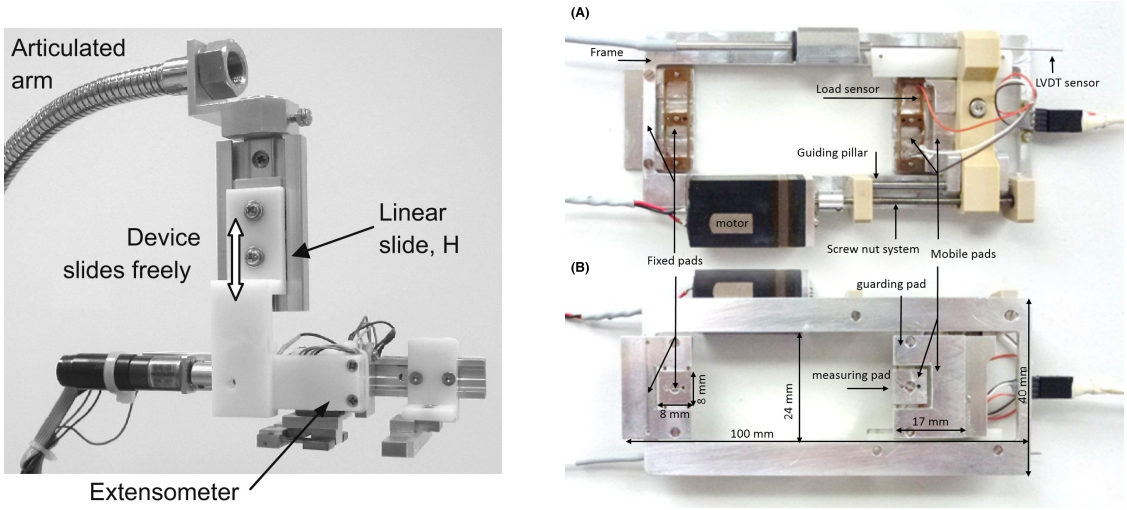

Figure 1.3: Prototypes of extensometer. (a) Photograph of shield pad extensometer mounted on an articulated arm with a linear slide attachment [15]. (b) Top (A) and bottom (B) views of the extensometer [16].

One recognized issue for *in vivo* characterization is the quantification of the mechanical properties, as the dimensions of the measuring gauge are hard to estimate [12]. Mechanical properties of skin are limited to linear [15, 17] or areal parameters [18]. The strain is easy to obtain from the changes in length. While the stress, or force per unit area, needs the knowledge of skin thickness and the tested skin width. For the ease of stress determination, researchers are interested to obtain a nearly uniform stress field during *in vivo* tests. To achieve this, an additional C-shaped shield pad is used to eliminate the influence of surrounding forces during *in vivo* measurements for the extensometer in Fig. 1.3a [15]. The guarding pads were also employed in Fig. 1.3b. In such a way, the width of tested skin is the same as that of the measuring pad [15]. The traction force was assumed to be homogeneously applied over the whole skin thickness (≈ 1 to $2\,\mathrm{mm}$), with an initial pad distance $30\,\mathrm{mm}$ and maximal strain rate about $0.03\,\mathrm{s}^{-}1$ [16]. The skin thickness is measurable by ultrasound. Knowing the cross-sectional area, the stress can be converted from the force. The stress and strain in the loading direction are determined as:

$$T = \frac{f}{A_0} = \frac{f}{d \cdot e_0} \tag{1.1}$$

$$\varepsilon = \frac{\Delta L}{L_0} = \frac{L - L_0}{L_0} \tag{1.2}$$

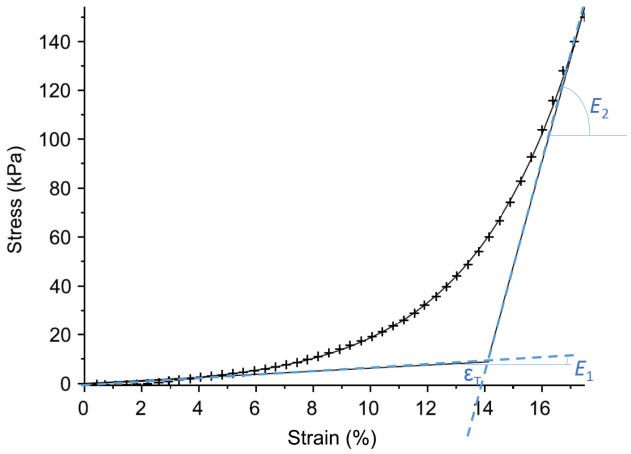

Figure 1.4: Experimental data (cross symbols) obtained on a right forearm solicited along 0°-axis; corresponding exponential model fit (solid line) from equation (1.3) and geometrical description of physical parameters. Obtained values: $A = 1.3$ kPa, $B = 27.4$, $E_1 = 62.7$ kPa, $E_2 = 4250$ kPa, $\varepsilon_T = 13.9\%$, and the quantified goodness-of-fit $R^2 = 99.95\%$ [19].

where f is the measured force, A_0 is the cross-sectional area, d is the tested skin width, and e_0 is the thickness of skin. ΔL, L, L_0 are, respectively, the displacement of skin, the final, and the initial length of tested skin segment.

To obtain skin parameters from the stress–strain curve, Jacquet et al., [19] proposed to use an exponential equation to fit the stress–strain curve in Fig. 1.4:

$$T = A\left[\exp\left(B\varepsilon\right) - 1\right], \tag{1.3}$$

where A and B are fitting parameters. Three physical parameters were identified from the stress–curve. E_1 and E_2 represent initial tangent modulus (corresponds to the contribution of the elastin fibers alone) and final tangent modulus (stands for the combined contribution of elastin and collagen fibers). ε_T in Fig. 1.4 is obtained from intercept of strain-axis with final slope of the stress-strain curve. The ε_T parameter is related to extensibility of the skin, a physiological load limit to maintain skin integrity, and a strain threshold, which should not be exceeded during a surgery to avoid medical complications [19]. Finite element simulation offers another approach to convert stress–strain from the force–displacement, which allows the identification of intrinsic parameters of skin, like modulus [14].

Viscoelasticity was also studied with an extensometer by creep and relaxation tests [14]. A four-parameter viscoelastic model based on the analogical Kelvin–Voigt model was proposed to describe skin behavior under single-axis extension. Furthermore, direction variations were explored with the extensometers [14, 19], which show the anisotropic properties of the skin. So the skin anisotropy is an aspect we should take into account when we study its mechanical behavior.

1.3.1.2 Indentation

A normal force is employed in the indentation tests, instead of the tangential force in extensometry. The schematic of an indentation device for *in vivo* application is presented in Fig. 1.5a. To identify mechanical properties of the skin, the indentation force and the indentation depth are measured (Fig. 1.5b). With static indentation tests, the reduced Young's modulus can be determined as [20]:

$$E^* = \frac{\pi}{4}\frac{k_z}{\delta}\tan\left(\frac{\pi}{2} - \alpha\right) \tag{1.4}$$

where $k_z = (\mathrm{d}F_N/\mathrm{d}\delta)\,|_{F_N=F_{N\max}}$ is the normal contact stiffness, δ is the penetration depth, and α is the half angle of the indenter.

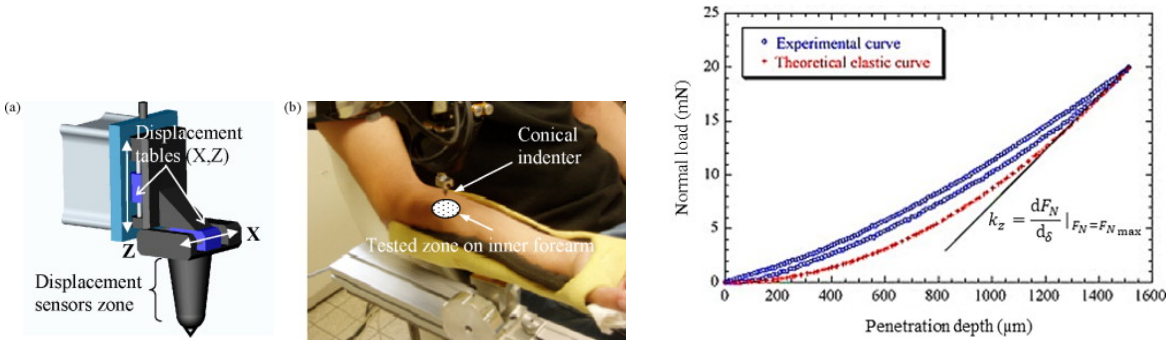

(a) (b)

Figure 1.5: Indentation setup (a) and obtained curve (b) [20].

However, the global apparent reduced Young's modulus was reported to increase with penetration depth, which was attributed to the influence of the subcutaneous tissues (muscle) [20]. With indentation tests, the influences of subcutaneous layers, like muscles, should be taken into account, to obtain accurate Young's modulus of skin.

1.3.1.3 Suction

The principle of suction tests is to apply a negative pressure and measure the vertical deformation of the skin. Fig. 1.6 shows a suction device Cutometer® and the typical results. The penetration depth is given by a non-contact optical measuring system inside the probe. The Cutometer® has been widely used to study skin elastic, viscoelastic properties, and skin aging. Two relative parameters, ratio of elastic recovery to distensibility (U_r/U_f) and the gross elasticity (U_a/U_f) are recommended to evaluate aging effects, considering their high correlation with age (Fig. 1.6b) [21]. A statistical study with suction tests indicates that female and male have different changes in skin mechanics during aging process. Compared to male's skin, a significant lower distensibility but higher elasticity were found in female's skin until the age of 40 [22]. Besides of studying the age-related and gender-related changes, suction tests can also be used to evaluate the efficacy of cosmetic products, such as antiaging treatment.

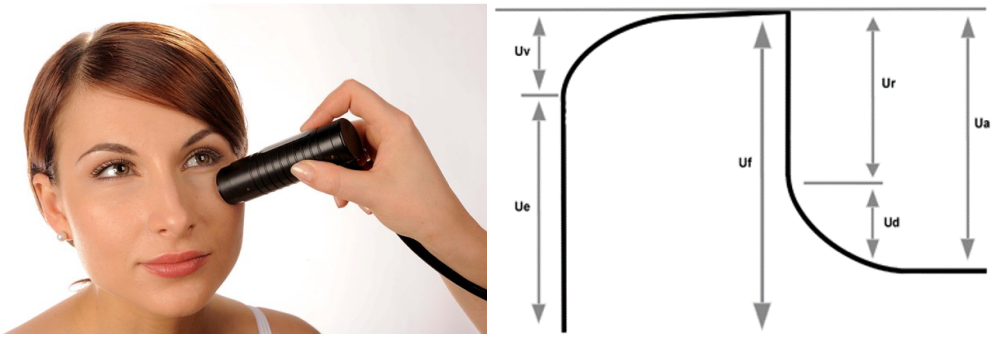

(a) (b)

Figure 1.6: Suction tests. (a) Cutometer® Dual MPA 580. (b) skin deformation-time curve obtained with suction tests, parameters presented in the figure are skin distensibility (U_f), immediate distensibility (U_e), delayed distensibility (U_v), maximum recovery(U_a), immediate recovery (U_r), delayed recovery (U_d) [21].

1.3.1.4 Torsion

Torsion tests are implemented by applying a constant torque and measuring the resulted angular deformation. The deformation curve obtained from torsion tests is similar to that of the suction tests [23, 24]. Torsional Ballistomer BLS 780 (Dia-Stron Limited, Hampshire, UK) was utilized to evaluate the efficacy of antiaging products [25] by measuring skin elasticity. An increased elasticity was observed after using the antiaging cosmeceutical product. Another application of torsion tests is on burn wound study [26].

1.3.2 *Ex vivo* tests

Previously, we introduced the working principles of four *in vivo* tests, which are also applicable for *ex vivo* study. Here, an example based on *ex vivo* tensile testing (also kown as tension testing) is presented. In the schematic of Fig. 1.7a, a pig skin sample (from dorsal or ventral) is mounted on the Instron 3300 and under uniaxial tensile test [9]. The *ex vivo* tests offer the possibility to strain the sample until failure, which is nearly impossible for *in vivo* tests with the code of ethics. The tensile response of skin is shown in Fig. 1.7b. It is characterized by an increasing slope of the stress–strain curve. The stress–strain curve in Fig. 1.7b is known as J-shape curve [9], which has four characteristic stages. A previous study from the same team investigated the structural evolution of skin under tensile loading [27]. Explanations were provided in Fig. 1.8 for the skin response in Fig. 1.7b at each stage:

- "Toe" and "heel" stages. Curved collagen fibrils are oriented and straightened along the tensile axis (Fig. 1.8 (a,e) and (b,f)). Strain is most due to straightening of the collagen fibrils rather than stretching at the beginning stage, leading to little increase of stress. In the heel region, a hardening response is presented with an increased slope.
- Linear region. All the collagen fibrils are stretching, sliding, delaminating and orientated completely along the tensile axis (Fig. 1.8 (c,g)). The modulus from this region E_{linear} is the highest (also referred to high strain modulus or "Young's" modulus in the literature). It is noticed that the definition of

modulus E_{linear} (Fig. 1.7a) is the same as the final tangent modulus E_2 (Fig. 1.4).

- Failure (fracture). The slop decreases at higher strains due to permanent damage.

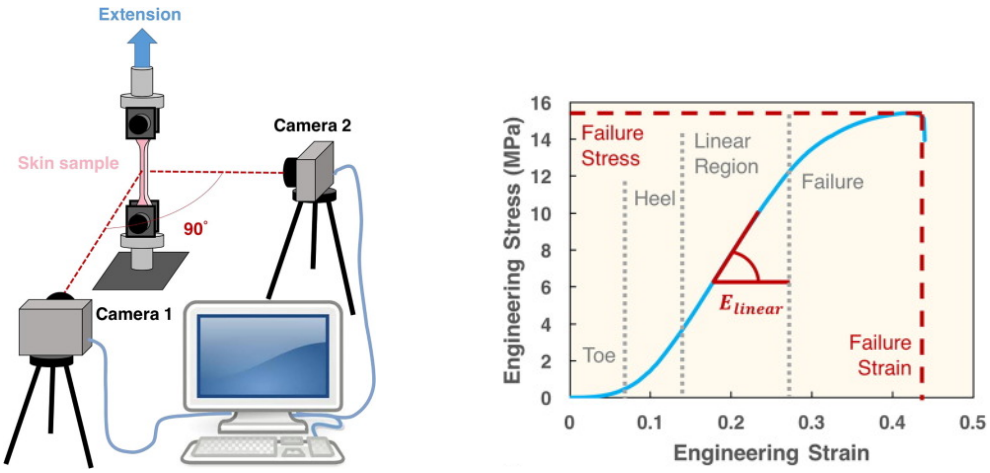

(a) (b)

Figure 1.7: *Ex vivo* uniaxial tests. (a) Experimental setup (b) Tensile response of skin, the "J-shape" curve. [9]

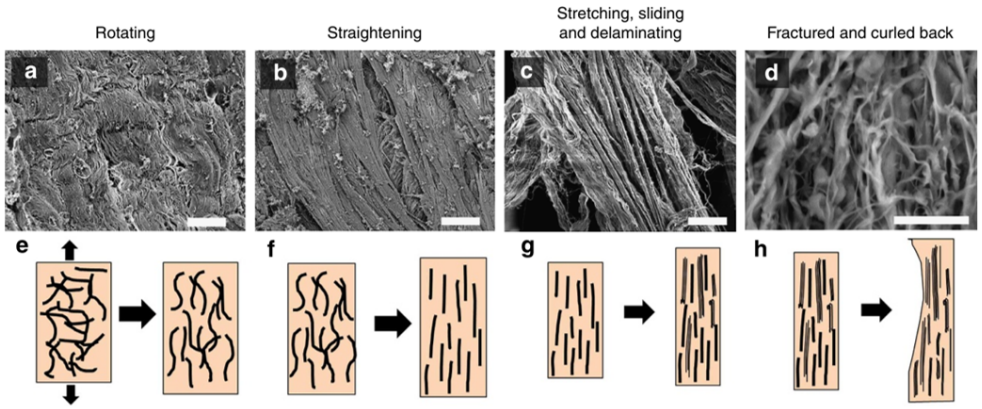

Figure 1.8: Mechanistic stages of the tensile loading of skin. Scanning electron microscopy images (a–d) and schematic drawings (e–h) of the mechanisms during the four stages of tensile loading of rabbit skin, black arrows in **a** and **e** represent the direction of tension testing. (**a**,**e**) Curved collagen fibrils are oriented along the tensile axis; (**b**,**f**) collagen fibrils are straightening, larger and larger amount of the fibrils re-orient close to the tensile axis; (**c**,**g**) collagen fibrils are stretching, sliding, delaminating and orientated completely along the tensile axis; (**d**,**h**) collagen fibrils are fractured and curled back. Scale bars in **a**–**d** are 20, 20, 20 and 50 µm, respectively. [27].

1.4 Efforts in early detection of pressure ulcers

Till now, the detection of PUs mainly relies on visual and tactile changes at the skin surface [28]. These traditional examinations have strong dependence on the expertise of health care providers. Besides, skin tone add difficulties in diagnosis of PUs [29]. Multiple studies attempt to explore new solutions for the diagnosis of PUs, objectively and timely. The detection principles lie in two main fields, involving variations in the electrical or in the mechanical properties.

Changes in the skin electrical properties have been considered for the early detection of PUs. A commercial product, Provizio^{TM} SEM Scanner (Bruin Biometrics, LLC, Los Angeles, CA, USA) intends to detect PUs at an early stage by measuring the changes of electrical capacity resulting from moisture variation [30]. Indeed, Sub-epidermal Moisture (SEM) has been related to the formation of PUs [28]. But the specificity of the device is limited, just around 32.9% [31]. In other words, there is a high chance around 67% that healthy people will be misdiagnosed with risk to PUs. Furthermore, SEM Scanner provides us only a delta value being the difference of the highest and lowest readings. The intrinsic physical parameters of skin are not accessible from these readings. On the other hand, Swisher et al. [32] designed an electronic sensing system based on a multiplexed electrode array to map the electrical impedance of tissue. They found pressure-induced tissue damage was correlated with a lower impedance magnitude in electrical impedance spectroscopy (10^2 Hz to 10^6 Hz) measured from rats.

Apart from electrical properties, skin mechanical properties have also been investigated for distinction of PUs. Indentation tests were used to study the viscoelastic difference between the subjects with Spinal Cord Injury (SCI) and a history of PUs and the subjects without SCI. The stress response with time and the initial Young's modulus were found significantly different between healthy skin and skin with PUs susceptibility [33]. Moreover, the skin affected by PUs tended to have lower elasticity compared to the healthy skin of SCI patients in the post-acute phase and able-bodied participants [34]. Additionally, clinical significance has been established with conformal piezoelectric system, where differences in modulus were discovered between lesion skin and normal one [35]. These researches highlight that skin mechanics are essential to evaluate skin conditions, even if more investigations and evidence are required to clarify the relationships in term of mechanical properties for the skin at risk.

Accounting for this state of the art, and in accordance with the other studies performed within the STINTS project, we focused on the mechanical behavior of the skin and on a portable device to measure the properties *in vivo*. Wang et al. [8] proposed a handled instrument for *in vivo* measurements of skin biomechanics, which could be used for early detection of PUs. The handheld instrument was composed of two piezoelectric benders, working as a "tweezer" to characterize skin biomedical properties. Results show that the device could distinguish skins from different sites. In quasi-static stretch (strain level: 16%), the palm skin (glabrous skin) was observed stiffer than the forearm skin (hairy skin). The skin response to sinusoidal signal (10 Hz) shows that the palm skin has a larger portion of viscosity than the forearm skin. This device has many advantages, such as the robustness, low cost, and compact size, making it easy to carry. It has drawbacks in terms of the measurement accuracy due to the nonlinearities of the piezoelectric bender. Therefore, it is the starting point of our work. To go further, a thorough knowledge on piezoelectric materials is vital for following applications (sensing and control). In the next sections, properties of piezoelectric materials are introduced.

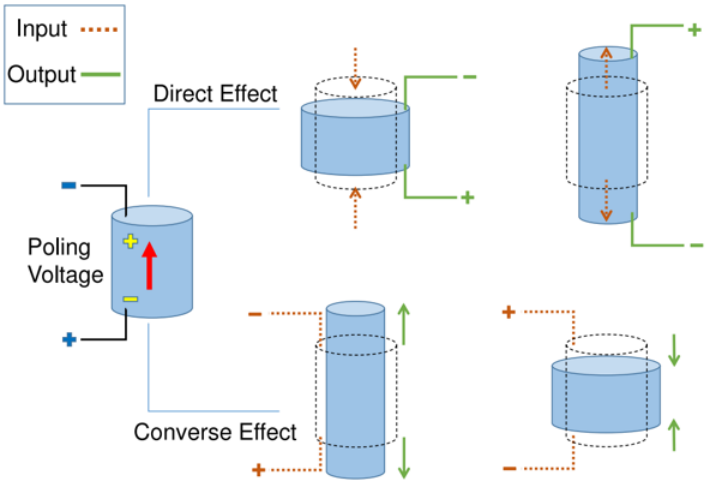

Figure 1.9: Direct and converse effects in piezoelectric ceramic [38].

1.5 Piezoelectric materials

The piezoelectric materials include crystals (quartz), ceramics (PZT, hard and soft), and PVDF for small systems applications [36]. Piezoelectric effect was first demonstrated by the brothers Pierre Curie and Jacques Curie in 1880 [37]. It refers to the direct phenomenon, where mechanical pressure induces electrical charge. While, inverse piezoelectric effect is referred to the converse phenomenon, which describes that the applied electric field will induce a mechanical deformation. These two effects are demonstrated through the schematics in Fig. 1.9.

1.5.1 Applications of piezoelectric materials (skin/soft tissue characterization)

The piezoelectric materials have a broad range of applications. Direct piezoelectric effect is usually employed in energy harvesting [39], sensing [40], vibration damping [41]. While inverse piezoelectric effect is commonly applied in actuation. The sensing and actuation applications are reviewed below, especially for skin or soft tissue characterization.

1.5.1.1 Piezoelectric bender

The representative structures of piezoelectric beam bending actuators are unimorph, bimorph, or multilayer bimorph. Unimorph or monomorph bender has one active piezoelectric and one passive flexible layer (Fig. 1.10a). Bimorph has two active piezoelectric layers. Fig. 1.10b shows two electrical configurations which are commonly used in bimorph fabrication, a series (or antiparallel) connection and a parallel connection [42]. The structure of a multilayer bimorph actuator is shown in Fig. 1.10c.

Concerning soft tissue/skin characterization, two main measurement principles are employed with respect to the working mode of the piezoelectric benders. One is based on resonant vibration. The characteristics (resonance frequency, amplitude) of resonant vibrating piezoelectric elements change when loaded

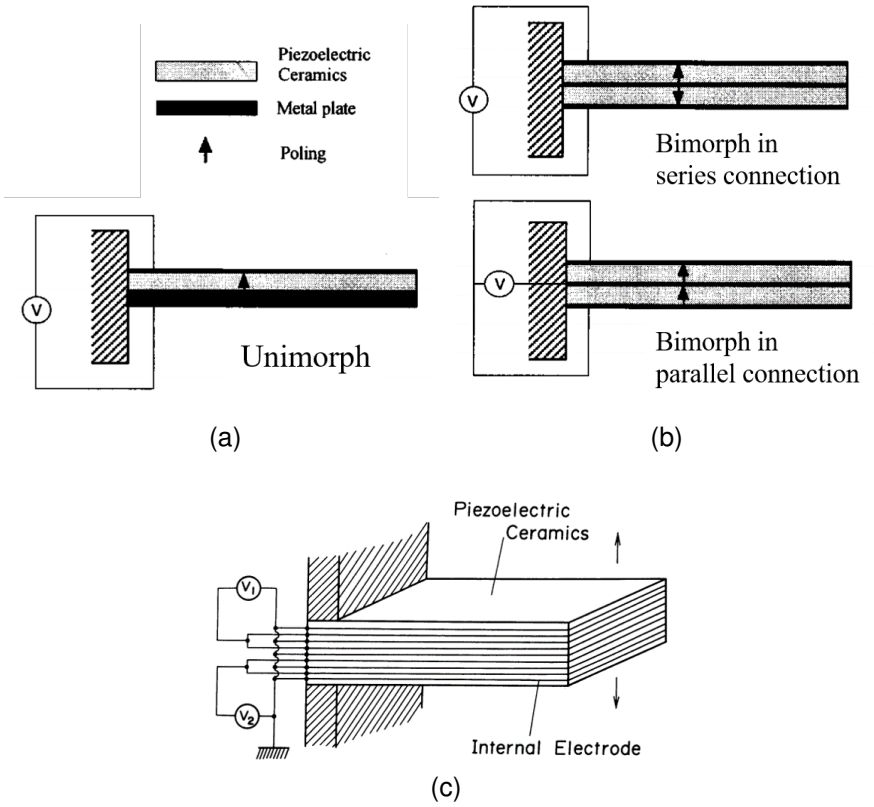

Figure 1.10: (a) Structure of a unimorph bender. (b) Structure of a bimorph bender [42]. (c) Structure of multilayer bimorph actuator [43].

with the testing materials. Fig. 1.11a shows a piezoelectric resonant sensor designed for tactile tissue differentiation, which was intended to assist surgical resection of brain tumors. This idea was demonstrated with experiments on tissue mimicking gel-phantoms by detecting frequency shift and amplitude variation of the sensor voltage [44]. Another example is using the resonant piezoelectric bender for indentation tests, as shown in Fig. 1.11b. A rigid sphere was glued to the free end of the actuator as an indentation device. The piezoelectric bimorph sensor/actuator was excited by a series of frequencies around the mechanical resonance of the structure. The frequency response of the system was measured by the 4294 impedance analyzer. The quantification of material properties was achieved based on Mason equivalent circuit, which is described in Fig. 1.12. The analogies between electrical and mechanical quantities are summarized in Table 1.2. The material properties were extracted by comparing the results of unloaded bimorph actuator and actuator loaded with the materials. Two parameters R_m related to viscosity and C_m related to contact stiffness were of interest. Based on those two quantities, the bimorph sensor/actuator could be used to differentiate the tested materials [45]. These two examples have demonstrated the feasibility of detecting different materials with resonant piezoelectric actuators. However, the measurements are indirect and the skin parameters are difficult to obtain.

A second working mode of the piezoelectric actuators is quasi-static (or low frequency, below $10\,\mathrm{Hz}$) [8, 47]. Fig. 1.13 shows an *in vivo* measurement system for the biomechanics of the fingerpad skin. A

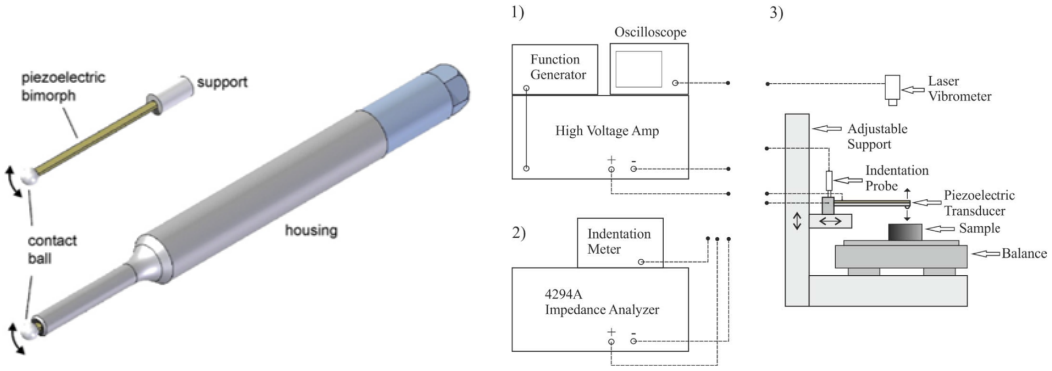

(a) (b)

Figure 1.11: (a) Piezoelectric bimorph sensor, arrows indicating direction of vibration [44]. (b) Test bench for the electromechanical impedance characterization of polymer samples [46]

Table 1.2: Analogies between electrical and mechanical quantities [46].

Electrical quantities	Mechanical quantities
Voltage V (v)	Force F (N)
Current I (A)	Speed of vibration $\dot{\delta}$ (m/s)
Electric charge q (C)	Displacement δ (m)
Capacitance C (F)	Elasticity/Compliance e (m/N)
Inductance L (H)	Mass M (kg)
Resistance R (Ω)	Damping D (Ns/m)

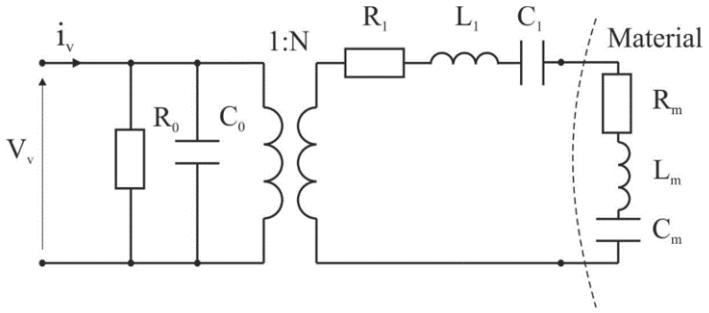

Figure 1.12: Simplified Mason's equivalent circuit for piezoelectric resonant actuator in contact with tested material (this circuit is valid only near resonance frequency considered) [46].

pair of piezoelectric bending actuators were used to apply tangential traction on the skin surface. The bender tip displacement δ was measured through a laser beam. The tip force was then calculated by $F = (\delta - k_2 V)/k_1$, where k_1 and k_2 denote two coefficients, deriving from the constituent equations of piezoelectric benders [47]. With this setup, the nonlinear elasticity and viscoelasticiy (creep, relaxation, and hysteresis) of skin were studied. The results may contribute to the numerical models and evaluation of skin conditions.

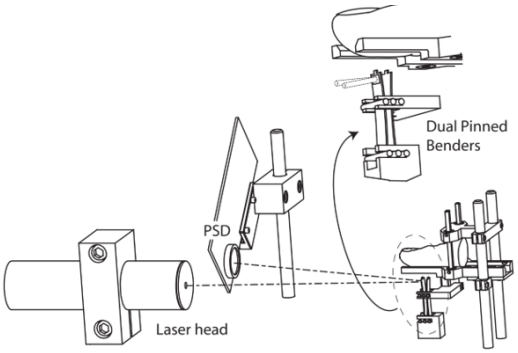

Figure 1.13: Apparatus for measuring finger pad skin under tangential traction. A pair of dual-pinned piezoelectric benders were used [47].

1.5.1.2 Langevin transducer

The bolt-clamped Langevin Transducer (LT), shown in Fig. 1.14 is recognized as the most common type of ultrasonic actuator. These actuators consist of piezoelectric discs sandwiched between metal electrodes. The centre bolt preloads the structure with a compressive force that is sufficient to prevent tensile forces during operation [48]. When applying an electric field to the piezoelectric layers, a force is generated in the vertical direction that displaces the two metal ends. Our colleague in the same STINTS project, works with a low-frequency ultrasound sensor based on LT [49, 50] to measure the acoustic mechanical impedance of skin.

The mechanical impedance z is a parameter relating the force and the speed of a structure under test, which is determined by:

$$z = \frac{f}{v} \tag{1.5}$$

where f denotes the dynamic force and v is the velocity. In Fig. 1.15, the LT is operating around its nominal resonant frequency (about $61\,\mathrm{kHz}$). A deformation sensor (piezoelectric sensor glued on the central part of the LT) is used to obtain the vibration velocity. The loading force is derived from a closed-loop velocity control, where the voltage difference between loaded and unloaded conditions enables the calculation of this external force.

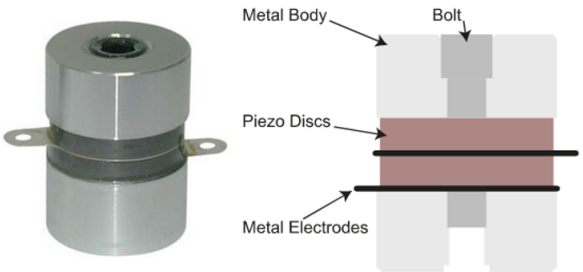

Figure 1.14: Bolt-clamped Langevin transducer with two piezoelectric layers [48].

It may be noted that this approach has also been applied by Torres et al.[51] to measure the acoustic force of a finger pad, within the framework of tactile feedback devices.

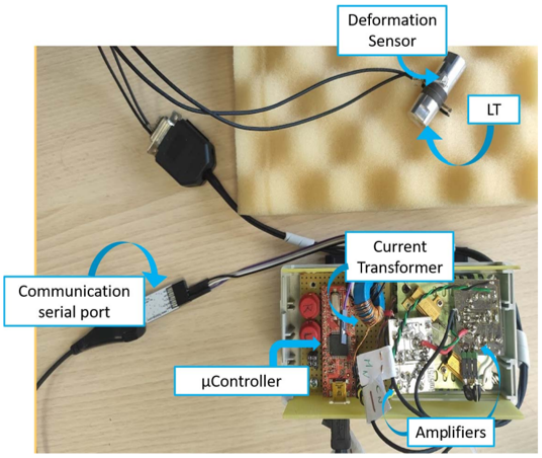

Figure 1.15: Langevin transducer used for mechanical impedance measurements [49].

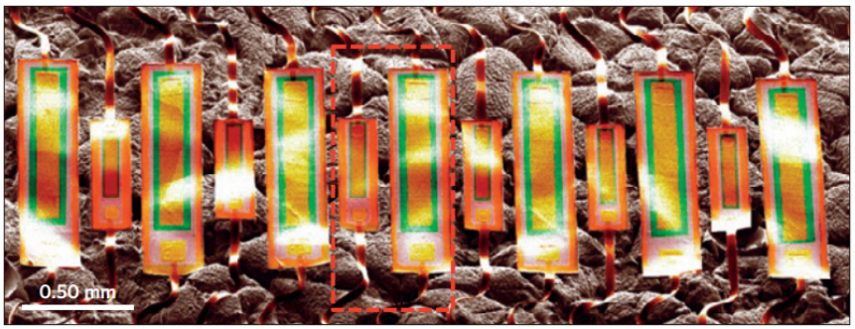

Figure 1.16: Thin, compliant modulus sensor (CMS) based on nanoribbons of PZT in arrays of mechanical actuators and sensors [35].

1.5.1.3 Piezoelectric film

An interesting application of the conformal piezoelectric devices was presented in [35]. The stretchable networks of actuators and sensors constructed with nanoribbons of PZT were used to characterize viscoelasticity of soft tissue *in vivo* [35]. The conformal and piezoelectric devices have clinical significance, which enable rapid and noninvasive characterization of skin mechanical properties.

1.5.2 Working principle of piezoelectric materials

Piezoelectric materials are active materials. They are characterized by a coupling between electric and mechanical fields. According to the IEEE standard on piezoelectricity approved in 1987 [52], the linearized constitutive equations were formulated to describe the piezoelectric behavior for general use as [53]:

$$S_p = s^E_{pq} T_q + d_{kp} E_k \tag{1.6}$$

$$D_i = d_{iq} T_q + \varepsilon^T_{ik} E_k \tag{1.7}$$

where on the left side, $\boldsymbol{S}$ represents the strain tensor, $\boldsymbol{D}$ is the electric displacement vector. On the right side, $\boldsymbol{T}$ denotes the stress tensor and $\boldsymbol{E}$ is the electric field vector. $\boldsymbol{s^E}$ is the elastic compliance matrix

when subjected to a constant electrical field. $\boldsymbol{d}$ is a matrix of piezoelectric material constants. $\boldsymbol{\varepsilon^T}$ is the permittivity measured at a constant stress. The subscript indices $p, q = 1, 2, 3, 4, 5, 6$ and $i, k = 1, 2, 3$, represent different direction in Cartesian coordinates. Equations (1.6) and (1.7) highlight that the material strain and electrical displacement (charge per unit area) are both linear to the applied mechanical stress and electric field [53]. It is noted that the mechanical and electrical dissipation and nonlinear behavior (hysteresis effects) are ignored in the constitutive equations. The standards based measurements are most meaningful for "piezoelectric materials with small dissipations and negligible nonlinearities" [52]. The nonlinearities of piezoelectric actuators will be discussed next.

1.5.3 On the nonlinear behavior of piezoelectric materials: hysteresis and creep

Piezoelectric actuators are popular attribute to their compact size, rapid response, and high resolution. They are widely used in nano/micro positioning or position track [54]. However, piezoelectric materials (particularly piezoceramics) suffer from nonlinear behavior such as hysteresis and creep, which deteriorates the overall performances, including the accuracy of sensing or control of the developed system [55].

The hysteresis in piezoelectric materials is generally explained by the residual misalignment of crystal gains in the poled ceramic [56]. The hysteresis behavior of piezoelectric actuators is a path-dependent memory effect. The output not only depends on the current state but also on the past output history [36]. The hysteresis of piezoelectric actuators between the applied voltage and the displacement have been widely discussed. The amplitude-dependent and frequency-dependent (rate-dependent) hysteresis (between the input voltage and the output displacement) are depicted in Fig. 1.17. The hysteresis loops vary with the input voltage amplitudes, as seen in the major and minor loops in Fig. 1.17a. Moreover, the input voltage frequency also has influences on the hysteresis behavior, where the hysteresis loop is expanded with an increased frequency as shown in Fig. 1.17b. So under a voltage value, the piezoelectric actuator can have multi displacement values, which can not be described by linear models [57, 58]. On the other side, the hysteresis between the applied force and endpoint displacement is barely discussed. Goldfarb and Celanovic [59] reported that the static hysteresis between the force and displacement existed when the electrode leads were shorted, see in Fig. 1.18. When the leads were open, no static hysteresis was exhibited.

Creep is another nonlinear behavior of the piezoelectric actuators. As shown in Fig. 1.19, the displacement continues to change after completing the voltage change. Creep "is related to the effect of the applied voltage on the remnant polarization of the piezoceramic actuator" [54]. At slow-speed (or low frequency) and open-loop operations, creep effect should be considered [60].

These nonlinearities pose challenging on characterization and modeling of the phenomenon. Rakotondrabe [36] suggested a frequency of $0.1\,\text{Hz}$ as a good trade-off to characterize static hysteresis behavior. Indeed, a frequency too high can introduce phase-lag effect (the effect of dynamics) to the static charac-

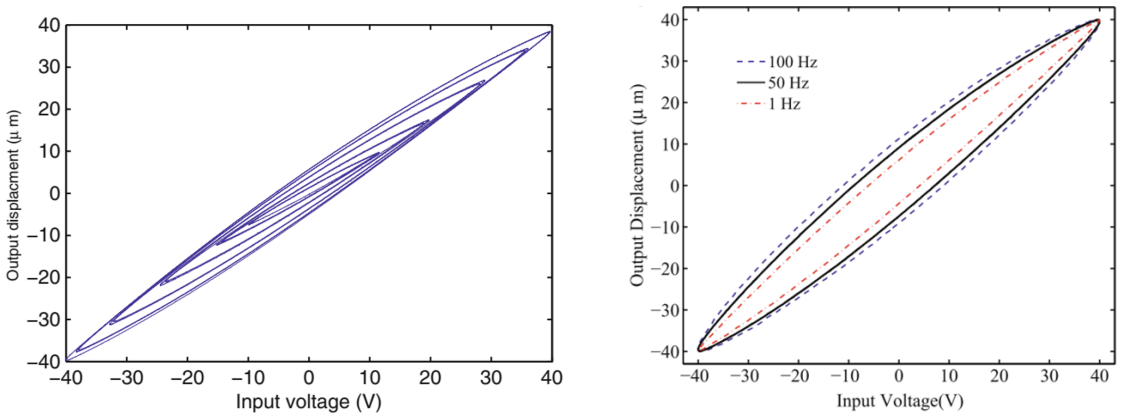

(a) (b)

Figure 1.17: Hysteresis between voltage and displacement. (a) Measured displacement of a piezo micropositioning actuator under sinusoidal input voltage. (b) Measured hysteresis loops of a piezo micropositioning actuator when a sinusoidal input voltage is applied at different excitation frequencies. Source: Fig.1.3 (a) (c) [36].

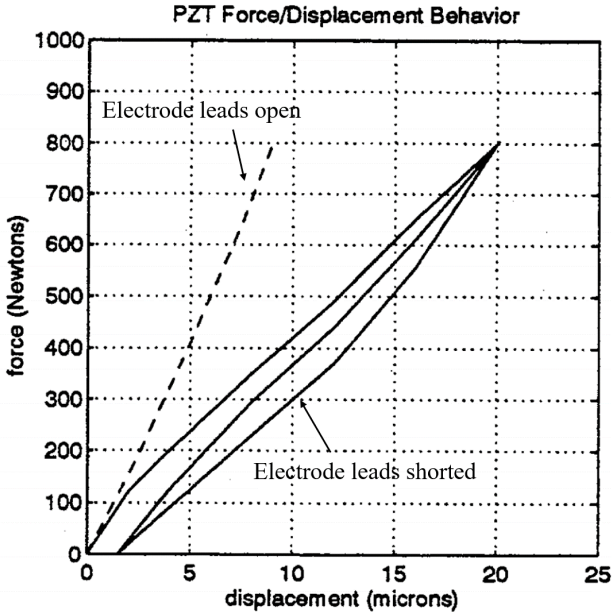

Figure 1.18: Quasi-static force-displacement relationship for a PZT stack actuator with open electrode leads and with shorted electrode leads [59].

teristic. On the other hand, a frequency too low may cause the creep phenomenon.

To improve the performance of the piezoelectric actuators, efforts have been devoted to their modeling and control, involving open-loop control techniques, closed-loop control techniques, or combining both [61]. For example, a feedforward charge control was applied to compensate the power losses in the piezoelectric actuator by feeding additional current to it [62]. The total amount of current was still controlled in closed loop. But the effects of external loads were not considered.

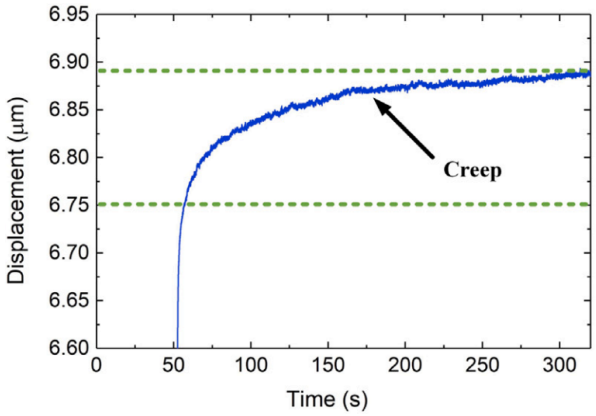

Figure 1.19: Typical creep effect of piezoelectric actuators when applying a step voltage signal to the positioning stage [60].

1.6 Voltage and charge drive/control

As mentioned previously, the behavior of piezoelectric actuators under voltage drive is subject to complex nonlinearities, which result in loss of accuracy, energy dissipation, and instability. On the other hand, it was reported that the rate-independent (static) hysteresis was not present between the displacement and the net electrical charge delivered to the actuator [59]. So charge drive was studied to increase the linearity of piezoelectric actuators.

The reduced hysteresis under charge drive can be explained by a simplified lumped parameter model of a piezoelectric actuator, as shown in Fig. 1.20. The model is composed of a strain-induced voltage source, V_{si}, a piezoelectric capacitance C_p, a nonlinear impedance Δ which models the nonlinear hysteresis, and a parallel resistor R_L modeling current leakage. The lumped parameter model was originally developed by Goldfarb and Celanovic in 1997 for describing the nonlinear behavior of piezoelectric actuators [59].

It is noted that the endpoint displacement is linear to the charge across the capacitor (q_p) [59]. The effect of R_L was initially ignored to analyze the hysteresis effect [58]. Under voltage drive (Fig. 1.20a), the charge on the capacitor ($q_p = C_p \times V_C$) is not linearly related to the input voltage (V_{in}), as the voltage across the capacitor V_C is not linear to the input V_{in} due to nonlinear impedance Δ. In consequence, the hysteresis is presented between input voltage and output displacement. On the contrary, operating with a charge drive (Fig. 1.20b), q_p is collected by the capacitor (C_p) and not affected by the nonlinear element (Δ) [63]. As a result, q_p is linear to the input q_{in}, and the relationship between the output displacement and input charge is linear. Hence, the nonlinear properties of piezoelectric actuators can be avoided by using charge drive.

However, current or charge drive suffers from poor low-frequency response. The DC impedance R_L causes parasitic current leakage, and consequently drift [58, 60]. To demonstrate the low-frequency limitation of charge drive, Clayton et al.simplified the model to C_p in parallel with R_L, and ignored the nonlinear

impedance (Δ) and the voltage (V_{si}) [63]. Thus, the transfer function between q_{in} and q_p is given by:

$$\frac{q_p\,(s)}{q_{\mathrm{in}}\,(s)} = \frac{R_L C_p s}{R_L C_p s + 1}. \tag{1.8}$$

Equation (1.8) is a high-pass filter, with a cutoff frequency $f_c = \frac{1}{2\pi R_L C_p}$. The high-pass filter leads to poor low-frequency tracking [63]. Therefore, the charge-driven method is not appropriate for low-frequency applications.

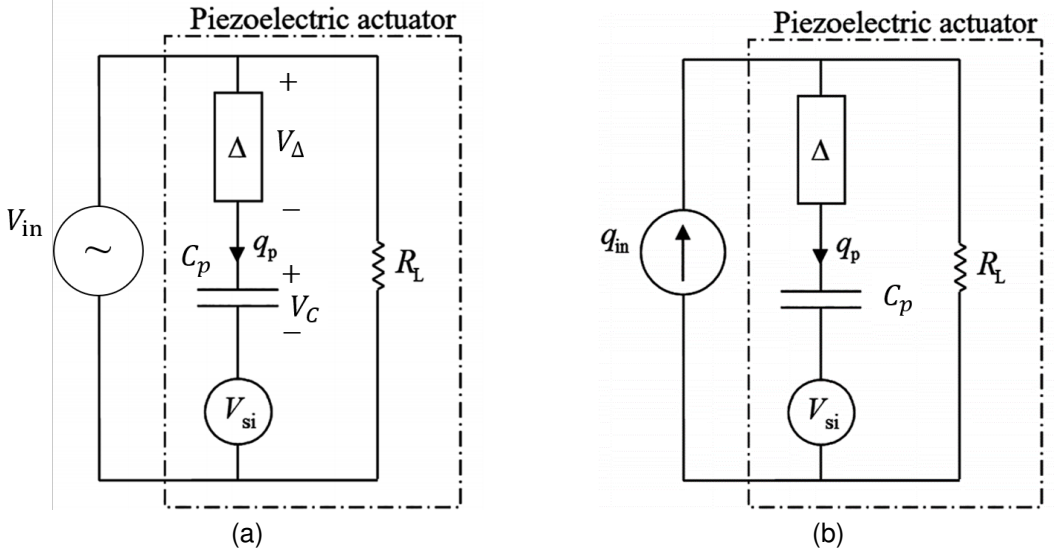

Figure 1.20: Lumped parameter model of a piezoelectric actuator. (a) Voltage drive. (b) Charge drive [58, 63].

1.7 Our proposal and experimental considerations

Accounted for the state of the art and inspired by the work in [8], we propose to develop a handheld probe based on two piezoelectric bending actuators and a set of strain gauge sensors to characterize biophysical properties of the skin. Beyond quantification of skin properties, we are interested in identifying the parameters highly related to PUs. It is aimed to provide a robust diagnosis tool to identify skin at risk.

The probe is designed to stretch the skin laterally, using two piezoelectric benders to deliver uniaxial tension. This testing technique can be classified into the family of "extensometry". We are primarily interested in the characterization of rheological properties of skin *in vivo* or *in situ* under quasi-static or low frequency deformation (below 10 Hz). But the operating frequency range can be extended, depending on the bandwidth of the developed system and the application scenarios. This probe will be able to measure the mechanical impedance (MI) of the skin. Indeed, changes in MI was used to characterize subcutaneous oedema [64]. The frequency responses of gels and lower legs at 10 Hz, 30 Hz, 100 Hz, 300 Hz and 1000 Hz were obtained using an impedance head (Bruel & Kjaer, 8001; Denmark). Results show that the MI decreased with an increased frequency. The differences in MI were greater at lower frequencies (up to 30 Hz)

for the gels with different water content. The gel with higher water content was associated with a lower magnitude of impedance. Further *in vivo* applications show that the MI of the pitting edematous tissues (soft tissues) was lower than that of the normal tissue, and lower than that of nonpitting edema (hard tissues). The differences between normal and abnormal tissues were also distinct at low frequencies. These suggest that at low frequencies we are more likely to detect changes in the material (skin or soft tissue). This evidence further justified our focus on the low frequency range.

It is clear that voltage control is the preferred method over charge/current control because we are working with low frequencies. The advantage of voltage control also lies in the relative simplicity of the drive and measurement circuits compared to charge/current control. Meanwhile, the nonlinear hysteresis in piezoelectric actuators under voltage control should be addressed.

Based on literature review, multi tests can be performed with the developed probe to study the mechanical properties of interest. For example, continuous quasi-static stretch is suit to study nonlinear elasticity. Cyclic loading can be performed to characterize viscoelasticity (hysteresis dissipation). Moreover, step stretch with constant displacement or force is realizable under closed-loop control, which can be used to study stress relaxation or creep effect. The technical requirements for the developed probe are specified, concerning:

- the strain level (displacement)–16% [8, 19]
- the range of stress (force)–$0.75\,\mathrm{N}$ [8]
- and the frequency applicable for *in vivo* skin measurements–below $10\,\mathrm{Hz}$.

On the other hand, the application of extensometry inevitably includes a loading component vertical to the skin surface. Hence, the range of indentation force (normal force) or indentation depth should also be in consideration. For example, a force of less than $1\,\mathrm{N}$ was required to indent a $17\,\mathrm{mm}$-diameter pressure head by $2\,\mathrm{mm}$ in the upper and lower arms [64].

1.8 Conclusion

Skin is known for nonlinear elasticity, viscoelasticity, and anisotropy. In this chapter, we summarized the testing methods, suitable for *in vivo* characterization. It was noted that the loading types (tension, indentation, suction, and torsion), amplitudes, and rates all have impacts on the characterized mechanical properties. The testing protocol should be standardized to have comparable measurements.

Further on, the piezoelectric materials were presented, focusing on their constitutive equations and existing nonlinearities. The applications of piezoelectric elements in soft tissue/skin characterization were used to elaborate two measuring principles, one based on resonant vibration, and the other based on quasi-static equation. We are in the latter case. The start point of our research relies on a previous work [8] using two piezoelectric bending actuators and strain gauges sensors to develop a mechanical impedance probe.

The work performed in [8] showed the possibilities to distinguish by that way the responses of the skin over different anatomical locations. Our assumption is that changes in skin biomechanics may indicate the development of skin issues, such as pressure ulcers. We are expected to provide a diagnosis tool based on the differences identified from healthy and abnormal skins. On the other hand, it can be used as a daily assessment tool to monitor potential changes in mechanical properties, and the development of pressure ulcers before they become visible.

The technical parameters of the developed probe were defined based on the literature. To achieve *in vivo* measurements, the first issue is on simultaneous sensing of force and displacement, which will be discussed in the next chapter. The inherent nonlinearities of piezoelectric actuators must also be addressed to have accurate measurements.

Chapter 2

Design of the mechanical impedance probe

2.1 Introduction

To characterize skin mechanical properties, the idea is to apply stimuli to the skin and measure its mechanical response. As previously explained, piezoelectric benders are used as the actuators to deliver a tangential traction force on the skin surface. Strain gauges are employed to build up the sensing system (i.e., force and displacement sensing). When subjected to an electric field, the free ends of clamped cantilever piezoelectric benders deflect. This tip deflection can be employed as a stimulus to the skin. The deformed skin then generates a reaction force that acts on the bender tips.

Direct measurements of displacement and force are essential to characterize skin biomechanics. These are achieved by integrating strain gauge sensors on the surfaces of the piezo benders. The stimulation and measurement are accomplished attributed to the actuator-sensor configuration. The piezoelectric benders and strain gauges form the probe for skin measurements. In the following, the probe is also referred to as Mechanical Impedance Probe (MIP), since it measures tip displacement and force, which can extend to the measurement of mechanical impedance.

This chapter details the design of the MIP and the validation of its functions. Starting from the requirements, the layout of the mechanical structure and the electrical parts of three prototypes are described. Here, we focus on the prototypes V1 and V2. The prototype V0 implemented with a dual-pinned structure is described in the Appendix A. The difficulties in mechanical realization of V0 have led to the development of prototypes V1 and V2, which are based on a clamped cantilever structure. Prototype V2 is an upgraded version of V1, with a normal force sensor embedded inside the MIP and a designed floating base. System characterization is performed to obtain knowledge on the behavior of the electromechanical system when subject to voltage excitation and (or) external load. Thanks to this prior knowledge, a linear sensing model is developed to estimate the tip force and the displacement from the driving voltage and the gauge signals. Experiments are performed to validate and evaluate the sensing model. Then, the MIP is used to

characterize different phantom skins. Effects of the normal force are discussed as well.

2.2 General requirements and overview of the probe structure

The mechanical impedance probe was designed to fulfill the following requirements. Some of them were already given in section 1.7:

- noninvasive,
- cost-effective,
- *in vivo* characterization of human skin properties,
- simultaneously measurements of force and displacement,
- high integration to be standalone and handheld,
- apply tangential traction to the skin (force below $0.75\,\mathrm{N}$),
- stimulate the skin by quasi-static displacement or low frequency vibration (below $10\,\mathrm{Hz}$), with a maximum strain level about 16%.

These requirements are satisfied thanks to the structure in Fig. 2.1, inspired by the previous work of [8]. To apply tangential strain to the skin, two piezoelectric benders are employed as actuators. The benders are clamped to each other at one extremity. The free ends stick out of the casing. When subject to voltage, each bender tip deflects due to the inverse piezoelectric effect. Taking parallel bimorph as an example, a typical configuration is depicted in Fig. 2.1. When the electric field is applied in the same direction as the polarization of the piezo element, such as the bottom layer, it tends to contract in the plane perpendicular to the applied field [65]. While for the upper layer, the electric field is antiparallel with the polarization and it tends to expand along the planes perpendicular to the field. As the upper layer extends and the bottom layer contracts, the bender tip bends downward in this case. If the electric field is applied in parallel with the polarization of the upper layer, then the piezo bender will bend upward. Under the actuation, the skin between the two tips is stretched or pinched by the piezoelectric benders, similar to a uniaxial tensile test. Consequently, the reaction force from the skin (perpendicular to the piezoelectric bending beam) acts on the bender tips, affecting the deflection of the benders. To deduce the skin force, additional strain gauges are used to measure the force-induced change in the bending strain. Note that no slip is allowed between the contact surfaces to ensure that the skin displacement is the same as the bender tips' displacement. Concerning skin tissue characterization, the derivation of skin force and displacement is explained later.

We aim to characterize the quasi-static mechanical properties of the skin *in vivo*. To avoid electric shock to the human body, insulation boots are added to the bender tips, as seen in Fig. 2.1. The level of tangential force/displacement applied to the skin surface should be taken into account to avoid any uncomfortable experience to the participants. Last, the normal force should be decided from a multi-criteria consideration, such as the compression tolerance of piezoelectric benders, the comfort of participants, and

the contact conditions between the bender tips and the skin.

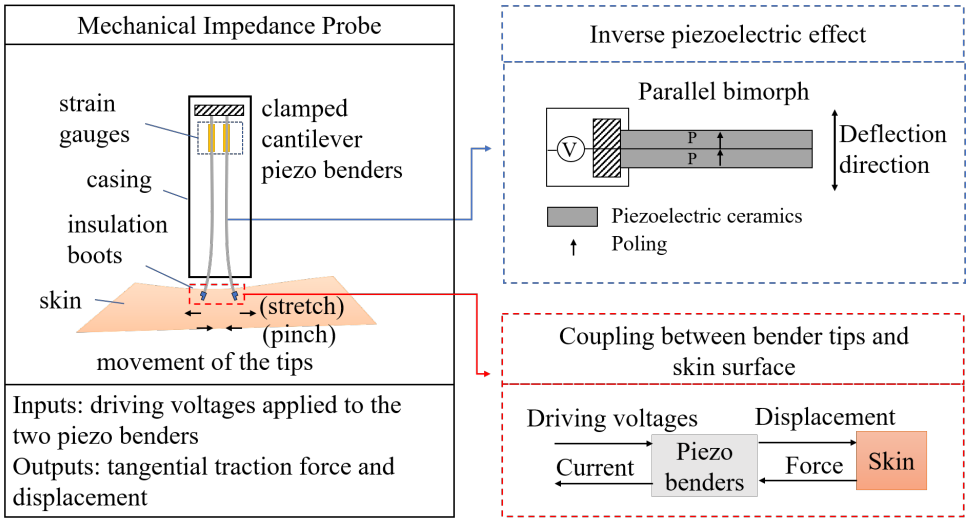

Figure 2.1: Scheme of the portable MIP. Force and displacement are in the tangential direction.

A standalone and handheld device is favorable for clinical application. It is achievable thanks to the small size of the piezoelectric bending actuators and the strain gauges. The following sections describe the design and implementation of the mechanical impedance probe, focusing on the mechanical structure and the driving and sensing circuits.

2.3 Design of the portable probe

2.3.1 Mechanical structure and piezo bender capabilities

The main body of the probe is the piezoelectric benders. Based on literature, we can mount the piezoelectric bender in two ways, as depicted in Fig. 2.2. The conventional way is to use a clamped cantilever condition, where the bender is clamped at one end and free at the other end (Fig. 2.2a). The dual-pinned structure was then proposed to increase the stiffness of the piezoelectric bender, which was applied in skin measurements [47]. The dual-pinned bender is hinged at two places with a distance l_1 along x axis, as seen in Fig. 2.2b.

Referring to Fig. 2.2a, for a clamped cantilever bimorph piezo bender, the vertical tip deflection δ in steady state is given by [65]:

$$\delta = \frac{-3d_{31}l^2}{4h^2}V - \frac{l^3}{2Ewh^3}f_r \tag{2.1}$$

where V is the driving voltage and f_r is the external force applied at bender tip, d_{31} is the piezoelectric coefficient (negative), E is the piezo material's Young's modulus, l, w and h are the effective length, width and thickness of the piezoelectric layer (dimensions refer to Fig. 2.3). Sign convention refers to Fig. 2.2a.

As previously mentioned, the dual-pinned structure was proposed to increase the stiffness of the piezo-

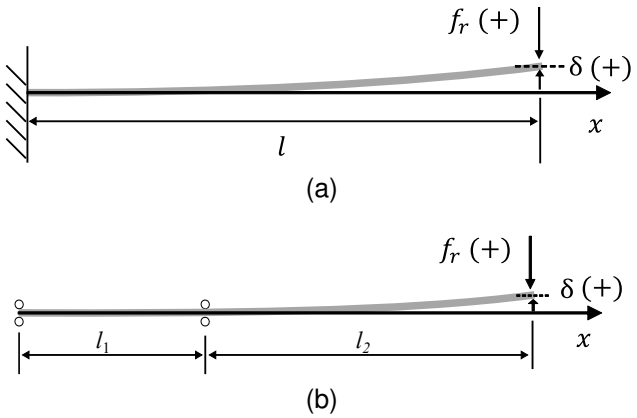

Figure 2.2: Mechanical structures. (a) Clamped cantilever piezoelectric bender. (b) Dual-pinned piezoelectric bender. l denotes the active length of the piezoelectric bender. l_1 is the distance between the two groups of pins along x axis and $l_1 + l_2 = l$.

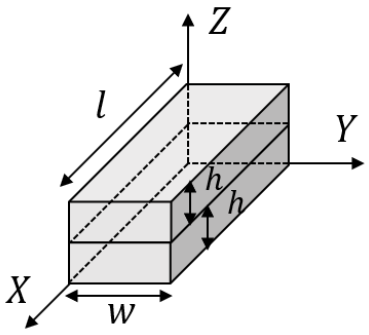

Figure 2.3: Schematic of bimorph piezoelectric bender.

electric bender. Referring to Fig. 2.2b, the tip deflection of dual-pinned piezo bender is changed to (2.2) [8].

$$\delta = \frac{-3d_{31}ll_2}{4h^2}V - \frac{ll_2{}^2}{2Ewh^3}f_r \tag{2.2}$$

Based on (2.2) and (2.1), we can compare the free deflection and stiffness of the two mounting approaches, see in Table 2.1. It can be seen that the free deflection of dual-pinned bender is reduced by a factor l_2/l, but the stiffness is increased by a factor $(l/l_2)^2$. By adjusting the position of the second pins along x axis, we change the ratio of l_2 to the total length of the bender l, leading to a trade-off between free deflection and stiffness of the piezoelectric bender.

Finite element analysis was performed to illustrate the mechanical differences between these two mounting approaches. The simulation was realized with software FreeCAD 0.20. Here, we consider the piezo bender as a passive beam (no piezoelectric effects were considered). The geometry and material

Table 2.1: Free deflection and stiffness of a cantilevered bimorph against a dual-pinned bimorph.

Mounting method	Free deflection	Stiffness
Clamped cantilever	$\frac{-3d_{31}l^2}{4h^2}V$	$\frac{2Ewh^3}{l^3}$
Dual-pinned	$\frac{-3d_{31}ll_2}{4h^2}V$	$\frac{2Ewh^3}{ll_2{}^2}$

Table 2.2: Parameters of finite element model.

l (mm)	w (mm)	$2h$ (mm)	l_2 (mm)	Pin's diameter (mm)	Density (kg/m^3)	Young's modulus E (GPa)	Poisson ratio	External force (N)
28	7.8	0.8	18	1.5	7600	80	0.23	1

Table 2.3: Numerical and analytical results of the cantilevered bimorph and the dual-pinned bimorph ($l_2 : l = 18 : 28$).

Parameter	Mounting method	Numerical	Analytical	Error
Displacement (mm)	Cantilever	0.27	0.27	0
	Dual-pinned	0.10	0.11	9%
Derived stiffness (N/mm)	Cantilever	3.70	3.64	2%
	Dual-pinned	10.00	8.80	14%

properties used for the simulation are listed in Table 2.2. A fixed constraint is applied at one end to model the clamped boundary condition for the clamped cantilever (Fig. 2.4a). While the dual-pinned condition is modeled by setting boundary conditions at the positions of the pins. A null displacement is imposed along Y and Z axes at the pins locations, and free displacement is allowed along X axis. Nevertheless, the bender is not supposed to slide along X axis, a fixed constraint is additionally applied at $X = 0$ (Fig. 2.4b). The two structures are subject to the same load, which acts at the bottom edge of the free end with a force value of 1 N.

The tip displacement of the bender loaded by an external force is shown in Fig. 2.4. It can be observed that the deflection of the dual-pinned bender is much smaller than that of the cantilevered bender. Under the same load, the cantilevered bender is displaced around 0.27 mm, while the displacement is reduced to 0.10 mm ($l_2 = 18$ mm) for the dual-pinned bender. This is related to the increased stiffness of the dual-pinned structure. The stiffness can be further calculated dividing the applied force by the simulated displacement response. Numerical simulation shows that the stiffness of the dual-pinned bender is more than two times higher than that of the cantilever bender (Table 2.3). On the other hand, the analytical stiffness is determined from the geometry and material properties, as described in Table 2.1. Analytical results shows that the dual-pinned bender is about 1.4 times stiffer than the cantilevered one. The analytical displacements are derived from (2.1) and (2.2), where $V = 0$ (no piezoelectric effect).

Table 2.3 compares the numerical results obtained from finite element simulation and the calculated analytical ones. For clamped cantilever bender, the numerical results are in a great agreement with the analytical ones. For dual-pinned bender, the boundary conditions are more complicated. The increased discrepancies between numerical and analytical results may rely on the approximation of the boundary conditions.

Numerical and analytical analysis have demonstrated that dual-pinned structure can enhance the stiffness of piezoelectric bending actuator. This was applied in [8, 47, 66], where the actuator's stiffness was adjusted by varying the ratio of l_2/l so that the bender's stiffness is sufficient to strain the skin to a desired

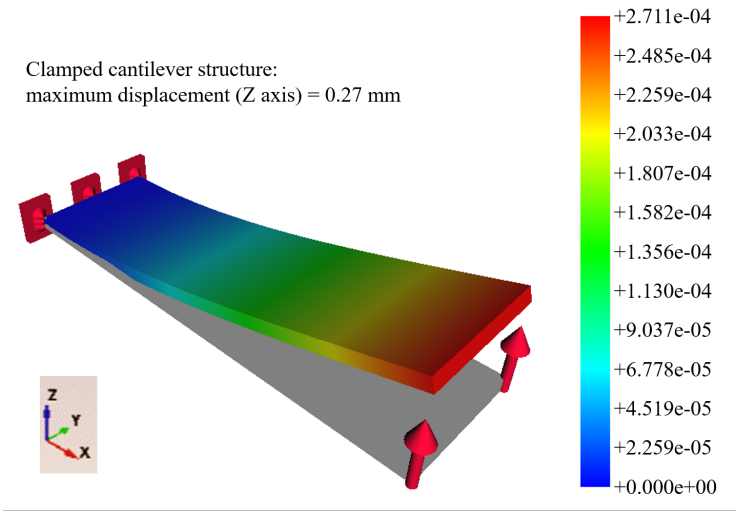

(a)

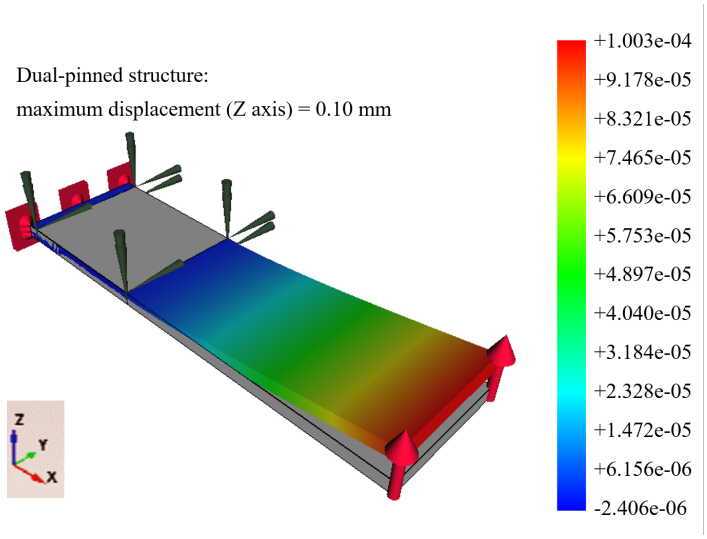

(b)

Figure 2.4: Tip displacement when subject to an external force of 1 N, represented by the upward red arrows. (a) cantilever bender, resulting simulated displacement about 0.27 mm. (b) dual-pinned bender, resulting simulated displacement about 0.10 mm.

level. However, a dual-pinned structure is hard to build since it requires a set of pins that have to be positioned with high precision. The pins also add difficulty to the miniaturization of the MIP. On the other hand, with the improvement of piezoelectric bending actuators, it is possible to construct the MIP with a clamped cantilever structure, without impairment of performance. In the following, we will analyze the properties of several piezo benders, regarding the requirements of a clamped cantilever structure.

We compared six commercial piezo benders from different manufacturers to select a suitable one for skin tests. The specification of each bender can be seen in Appendix B. The travel range of piezo benders when loaded by skin and the operating voltage are two main considerations for the bender selection. In the study of Wang et al. [8], the force of palm skin reached 0.6 N with a strain around 16% (initial gap 1 mm). In a following study on finger pad skin, a traction force around 0.5 N was needed to strain the skin to

80% with an initial gap of $0.25\,\mathrm{mm}$ [47]. The skin force–displacement curve can be derived from the original force–strain curve of fingerpad skin given in Fig. 3 ($l_2 = 11\,\mathrm{mm}$) [47]. The skin strain is determined from the change in length over its initial length. In our case, the initial length of skin segment is defined by the initial gap between the two benders. Larger displacement is required when the initial gap is larger to achieve the same strain. In Fig. 2.5, the skin curves are plotted by converting the skin strain to displacement, considering an initial gap of $0.25\,\mathrm{mm}$ and $1\,\mathrm{mm}$, respectively.

The performance of different piezo benders are compared in Fig. 2.5, based on their free stroke and blocking force. The skin force–displacement curves are plotted as a reference. The intersections of the bender curve and the skin curve show the strain level to which the skin can be stretched by the benders. It can be seen that PB4NB2S from ThorLabs has the highest stiffness. Piezo benders PI PL128.10 and ThorLabs PB4NB2S are able to stretch the skin to a large strain level, when the initial gap is small like $0.25\,\mathrm{mm}$. If the initial gap is increased to $1\,\mathrm{mm}$, piezo bender from ThorLabs has a better performance. The largest skin displacement could be achieved with bender model PB4NB2S from ThorLabs, referring to the intercept points of piezoelectric bender curves with skin curves. Besides, a relatively low voltage was required for PB4NB2S to reach the same displacement, comparing the nominal voltage (denoted as $V_{\max}$ in Fig. 2.5).

It is obvious that among all the benders, the PB4NB2S from ThorLabs is a preferred bender model, considering its high stiffness, large enough deflection when loaded with skin, and relative lower nominal voltage. Once the basic functional requirements are met, the cost and the dimensions of the piezo bender are other two factors to be considered. Once again, the piezo bender PB4NB2S from ThorLabs is more interesting from this point of view. So, according to the piezo bender PB4NB2S capabilities and given the effortlessness in mounting, a clamped cantilever structure is chosen with this bender model.

2.3.2 Positioning and choice of the strain gauges

Besides the selection of the piezo bender and the mounting method of the two benders, the choice of the strain gauges and their positioning are the other aspects to be considered. The total moment M_{tot} of a clamped cantilever bender along its length x can be written as (2.3) [67]

$$M_{\mathrm{tot}} = M_p - f_r(l - x) \tag{2.3}$$

where M_p is the uniform piezoelectric moment caused by the driving voltage applied across the piezo layers, and $f_r(l - x)$ is the bending moment caused by the external force f_r applied perpendicularly to the tip of the piezo bender. The surface strain ϵ of the piezoelectric bender along its length is then determined by

$$\epsilon = \frac{M_{\mathrm{tot}} t_p}{2EI} \tag{2.4}$$

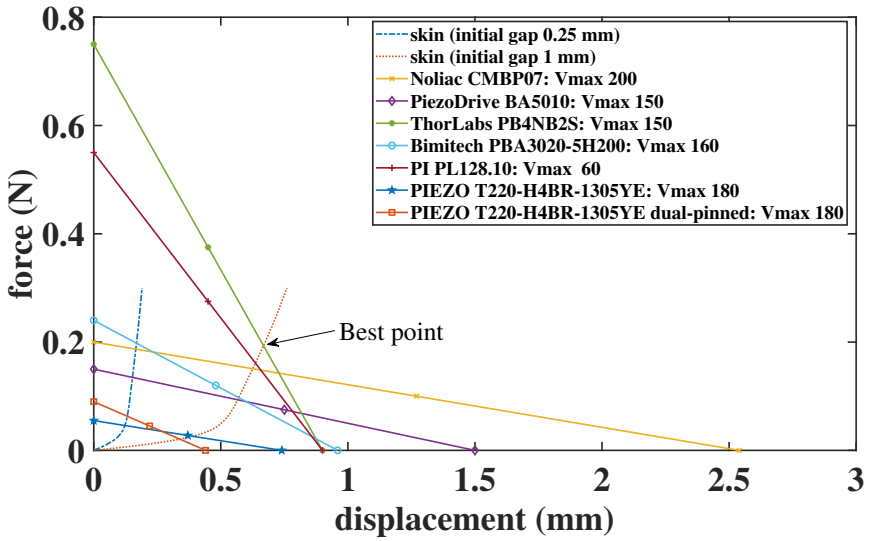

Figure 2.5: Piezoelectric bender selection. The parameters used to draw the bender curves are from manufacturers' data sheets, except for PIEZO T220-H4BR-1305YE adopted from [66]. This bender from PIEZO (used to be T220-H4-303Y) was used in [8, 47, 66] and its behavior with dual-pinned structure was added to compare. Skin curves were derived from data in [47]. Note that the proposed probe has two benders working symmetrically, thus, the displacement value here represents the relative displacement between the two benders.

where t_p is the thickness of the piezoelectric bender (depending on layer thickness h and the number of layers), E is the Young's modulus, I is the moment area of inertia.

A strain gauge glued to the bender surface, between the positions x_1 and x_2, measures the average strain ϵ_{ave} along its length:

$$\epsilon_{\text{ave}} = \frac{1}{x_2 - x_1} \int_{x_1}^{x_2} \epsilon \, dx = \frac{t_p}{2EI} \left[M_p - f_r \left(l - \frac{x_1 + x_2}{2} \right) \right] \tag{2.5}$$

with x_1, x_2 as the starting and ending positions of the strain gauge. Referring to Fig. 2.6, (2.5) is simplified to

$$\epsilon_{\text{ave}} = \frac{t_p}{2EI} [M_p - f_r(l - l_s)]. \tag{2.6}$$

When driving the bender with a given constant voltage, if there are changes in the strain, they are due to changes of the external force. The strain difference ϵ_{diff} can be presented as

$$\epsilon_{\text{diff}} = \epsilon_{\text{free}} - \epsilon_{\text{load}} = \frac{t_p}{2EI} f_r (l - l_s) \tag{2.7}$$

where ϵ_{free} and ϵ_{load} represent the strain measured by the gauge when the bender tip is free and loaded, respectively, under the same driving voltage ($M_p = cste$). Hence, f_r can be derived from ϵ_{diff}.

From (2.7), it is clear that the smaller l_s, the larger ϵ_{diff}. To enhance the sensitivity of the strain gauge to external force, a small l_s is desired. This can be achieved by placing the strain gauge as close as possible to the clamped edge of the piezoelectric bender. In addition, the shorter the gauge length, the smaller l_s we can achieve. The performance of strain gauges with different lengths and positions (Fig. 2.7), so different

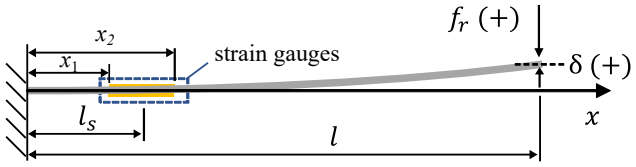

Figure 2.6: Geometry of the clamped cantilever bender with strain gauges glued on the top and bottom surfaces. x_1 and x_2 denote the starting and ending positions of the strain gauges. l_s indicates the center position of the gauges.

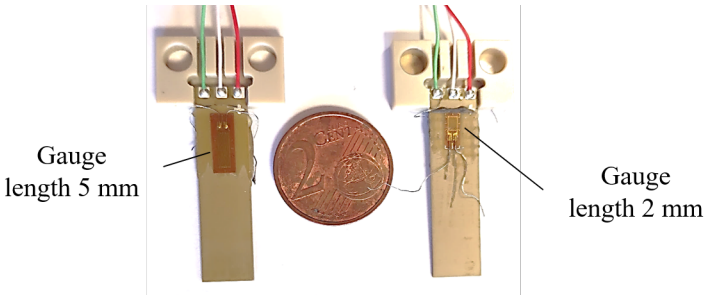

Figure 2.7: Layouts of strain gauges relative to the piezo bender. The strain gauges with gauge length of 5 mm (on the left) were glued with their soldering leads close to the clamped edge. While the strain gauges with gauge length of 2 mm (on the right) were glued with their soldering leads away from the clamped edge

values for l_s, are compared in Table 2.4. The sensitivity of ϵ_{diff} to the external force f_r is increased by 50% by reducing the gauge length (from 5 mm to 2 mm) and placing the gauge closer to the clamped end. Moreover, a safety distance to the driving electrodes is needed to avoid crosstalk. Last, for each piezo bender, to improve the measurement of the bending strain, two strain gauges (not a single one) were glued on the top and bottom surfaces. In our final design, foil strain gauges (RS PRO 632-124) with a gauge length of 2 mm were used. In our case, the distance is kept around 1 mm. The layout of the strain gauges relative to the piezo bender can refer to Fig. C.1a in Appendix C on strain gauge installation.

The strain is measured through a Wheastone bridge, which is formed by the two strain gauges and two other resistors, see in Fig. 2.8. Electrically, they are mounted in differential mode. It is the difference between the strain of the gauges that is measured. The benefits include temperature compensation and exclusion of the strain arising from the pressing along X axis. The second bender is configured in the same way. More description on the electronics is given later.

Table 2.4: Strain gauge sensing performance in response to the external force.

Strain gauge type	Base length (mm)	Gauge length (mm)	l_s(mm)	$\frac{\mathrm{d}\epsilon_{\text{diff}}}{\mathrm{d}f_r}$ (V/N)
RS 632-168	9.5	5	7.5[a]	0.24
RS 632-124	6	2	2.5[b]	0.36

[a] corresponding to Fig. 2.7 (left)
[b] corresponding to Fig. 2.7 (right)

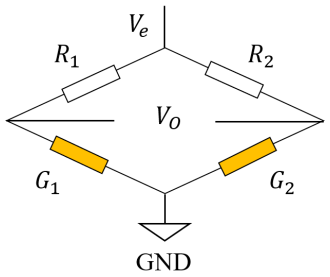

Figure 2.8: Wheatstone bridge. G_1 and G_2 represent the two strain gauges. R_1 and R_2 denote two resistors.

Table 2.5: General information on selected piezoelectric benders and strain gauges.

Components	Model	Material	Length (mm)	Width (mm)	Height (mm)
Piezoelectric benders	PB4NB2S	PZT	active length 28	7.8	0.8
Strain gauges	RS 632-124	Foil (mild steel)	gauge length 2, base length 6	2.5	/

2.3.3 Prototypes V1 and V2: clamped cantilever structure

As previously explained, the better choice we considered is the clamped cantilever structure. That is our conclusion after the first trials we performed with a dual-pinned structure, described in the Appendix A (prototype V0). As suggested in Fig. 2.5, multilayered bimorph benders PB4NB2S from ThorLabs were employed to build the new prototypes V1 and V2 with a clamped cantilever structure. The properties of the piezoelectric benders and the strain gauges are listed in Table 2.5.

Compared to the prototype V0 relying on a dual-pinned structure, following modifications are highlighted for prototypes V1 and V2:

- mechanical clearance by mounting the two piezoelectric benders with a clamped cantilever structure (bender model PB4NB2S),
- separated strain signals for each bender instead of a relative strain between the two benders,
- design of switching amplifiers for a better system integration (instead of a linear amplifier).

Prototype V1 is presented in Fig. 2.9. The holders of piezoelectric benders were clamped together by two cap screws. A pair of strain gauges were glued on the top and bottom surfaces of each bender, close to the clamped edge. The installation process of strain gauges is explicitly described for prototypes V1 and V2 in Appendix C. White heat shrinks were used to hold gauge wires in place. For the sake of safety and increase traction [8], a pair of boots were added to the bender tips to avoid electric shock and slipping. The boots were made out of FR4 (the substrate layer of PCBs).

Based on preliminary measurements with prototype V1, it was confirmed that the normal force F_n applied to the skin surface is important for *in vivo* tests. To strengthen the repeatability and reproduciblity of measurements, a prototype V2 (Fig. 2.10) was developed, with an additional function of normal force measurement. The inner part of Prototype V2 is composed of a fixed part and a mobile part. These two

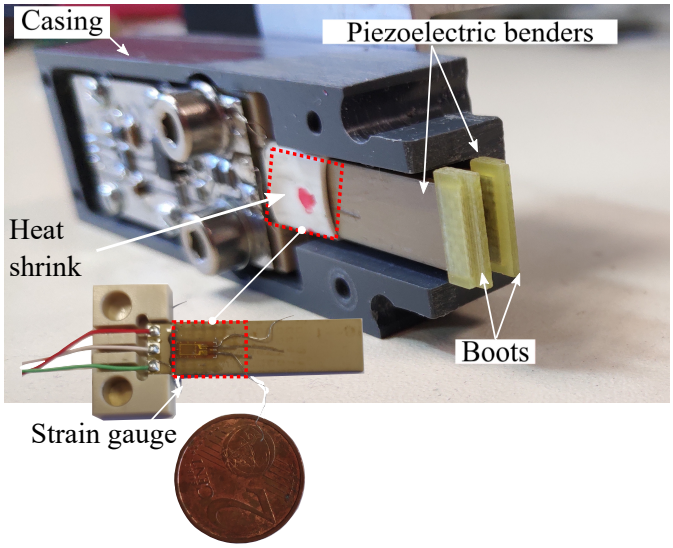

Figure 2.9: Prototype V1. Piezoelectric bender PB4NB2S from ThorLabs. Insulating boots (material FR4, the substrate layer of PCB) are attached to the free ends. The coin is used as a scale reference.

parts are connected by two pairs of magnets (one pair on each part) and two springs. A force sensor (Honeywell, FSS low profile force sensor) is embedded on the mobile part as shown in Fig. 2.10c, to measure the normal force (longitudinal direction of the piezo bending beam) applied to the bender tips when they are in contact with materials. By screwing in, the flat end of the screw will be in contact with the force sensor. Continuing screwing in, we can push the mobile part away from the fixed part so that the bender tips get out of the casing with a reasonable distance, such as shown in Fig. 2.10a.

Another feature of prototype V2 is the floating base. The two piezoelectric benders are clamped together. A rectangular frame surrounded by foam is attached to the base as well. Rather than being tightened to the casing, the clamped base is floating inside the casing. The floating base is designed for the security sake of the piezoelectric benders, which allows a global lateral shift of the two benders which may appear due to breathing, blood flowing, or other body movements.

2.3.4 Electrical part

To realize the measuring functions of the probe, we need to enable the actuation of the piezo benders and the sensation of the bending strains. The electrical circuits presented are designed for the prototypes V1 and V2 employing piezo benders PB4NB2S. The diagram of Fig. 2.11a shows the electrical connections of the system, taking one piezo bender as example. The second bender is configured in exactly the same way so that the two benders can work symmetrically. The implemented control box is shown in Fig. 2.11b. The main functions of the control box are to drive the two benders and to collect the gauge signals. In addition, information about the driving voltages of the piezo benders is sent back to the microcontroller unit (MCU) for control purposes. The MCU we used is a “through hole” G80 (G80 TH), with a processor STM32F427VGT6. The MCU is connected to the PC by a USB cable. A voltage regulator is used to convert the 5 V provided by USB connection from the PC into a clean (noiseless) 3.3 V power source for

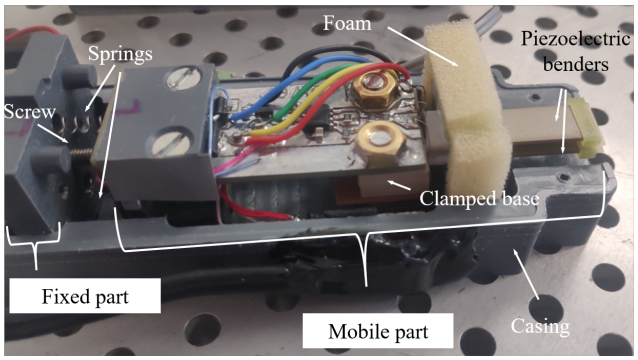

(a)

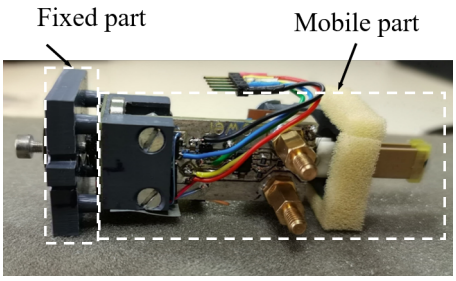

(b)

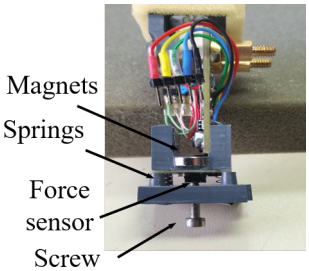

(c)

Figure 2.10: Prototype V2, piezoelectric bender model PB4NB2S from ThorLabs. Insulating boots (material FR4, the substrate layer of PCB) are attached to the free ends. (a) Global view of V2. The mobile part is pushed away from the fixed part by a screw. (b) Inner part of V2, it consists in a fixed part and a mobile one and can be removed out of the casing. (c) Contact profile of the immobile and mobile parts.

the MCU. As the maximum driving voltage of PB4NB2S is 150 V, we chose a DC/DC converter (R12-150B) to convert 12 V DC power supply to a bus voltage of 150 V. The design of the driving and measuring circuits is detailed in the following sections.

2.3.4.1 Driving and measuring circuits of the piezoelectric bender

To reduce power losses and obtain compact size, switched inverters were used to supply the two benders. A pulse width modulation (PWM) method was adopted to regulate the voltage supplied to the bender. The switching frequency was set to 25 KHz to avoid generating audible noise. To be less redundant, we still use one piezo bender as an example.

The bending actuator PB4NB2S is constructed with multiple co-fired piezoceramic layers made of PZT (THP51) and Pb(Zr,Ti)O3. Ag/Pd are used between these ceramic layers. The bender works in differential voltage control mode, see in Fig. 2.12. The red wire and green wire are connected to 150 V and 0 V (ground), separately. The white wire is connected to the driving voltage with a range of 0 V to 150 V. Varying the driving voltage, the bender can be controlled to bend upward and downward. Tip deflection occurs as the top and bottom layers elongate by different amounts. The driving and measuring circuits of the piezo bender are depicted in Fig. 2.13a. The piezoelectric bimorph bender (PB4NB2S) is modeled by two capacitors with a capacitance 0.55 µF on each side of the bimorph. Each piezoelectric bender is driven

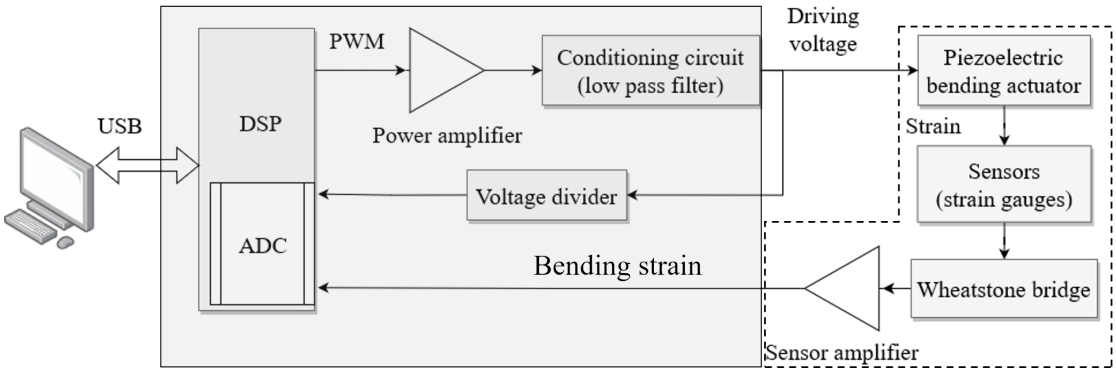

(a)

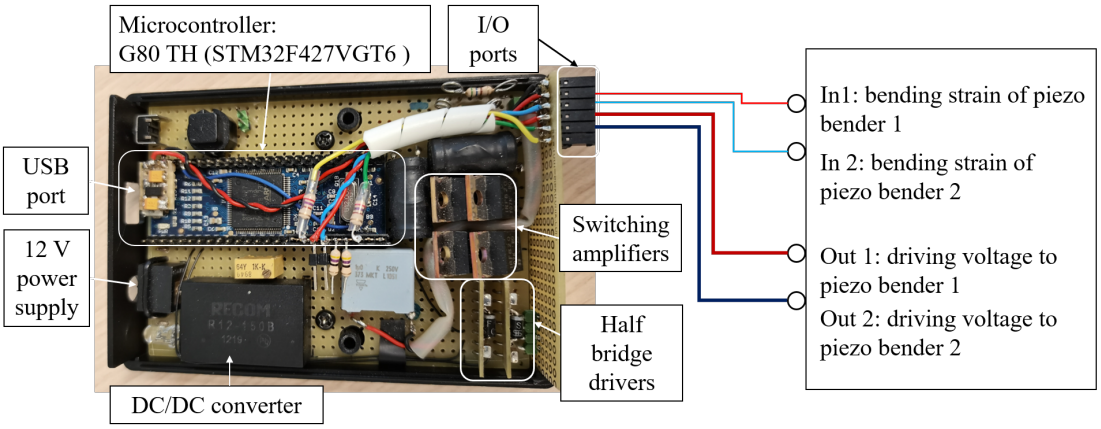

(b)

Figure 2.11: Supply and control system. (a) Scheme of system organization, taking one piezo bender as example and the second one configured in the same way. (b) Hardware implementation.

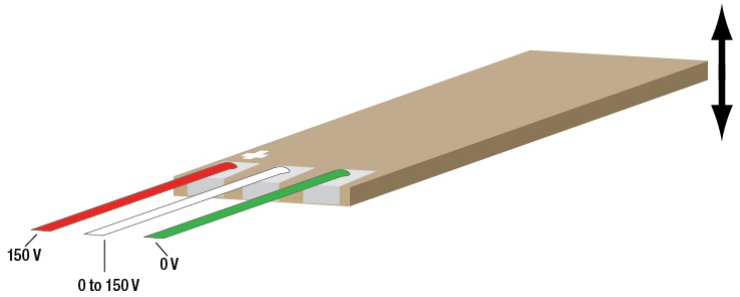

Figure 2.12: Driving mode of piezo bender PB4NB2S using differential voltage control (the multi-layer structure is not presented here). Source: adopted from the manufacturer ThorLabs.

by a switching amplifier, separately. A half-bridge driver (IR2302) is used to drive the two N-channel power MOSFETs, which form a leg. The amplified voltage passes through a low pass filter, which is composed of the inductor (L_1), the damping resistor (R_8) and the capacitance of the bender. Voltage dividers are added to scale the high voltages, such as the driving voltage, to be within the measuring range of DSP.

In order to tune the inductance and the resistance of the power circuit, we performed AC analysis with the software LTspice XVII. Fig. 2.13b shows the simulation circuit of the second order low pass filter, represented by the bender with its equivalent input capacitance ($1.1\,\mu$F), together with the inductor (L_1) and the damping resistor (R_8). The frequency response (Fig. 2.13c) shows that with $L_1 = 100\,$mH and $R_8 = 560\,\Omega$, the cut-off frequency of the low pass filter is about $280\,$Hz, which is relevant with our specifications. Moreover, the high frequency components are attenuated efficiently with a magnitude of $-68\,$dB at the switching frequency of $25\,$KHz.

To examine the power supply, we sent a pulse width command to the DSP and measured the pulse width signal, the output of one leg, and the voltages before and after the damping resistor (R_8) through an oscilloscope (PicoScope 6). The results are shown in Fig. 2.14. The driving pulse (blue curve, duty cycle of 30%, ranging from $0\,$V to $3.3\,$V) is the input of the half-bridge driver. At the output of one leg, an amplified voltage is obtained (red curve, $0\,$V to $150\,$V). This voltage is then filtered by the low pass filter. The yellow and green curves show the voltages before and after the damping resistor (R_8). Finally, a DC driving voltage around $45\,$V (green curve) is obtained through PWM with a duty cycle of 30%. It indicates that the driving voltage of the bender is successfully generated through the designed electrical circuits.

2.3.4.2 Electrical connection of the strain gauges

On a piezo bender, two strain gauges are glued on the top and bottom surfaces to measure the bending strain. The working principle of strain gauges relies on the change of their resistance when a stress is applied. Thus, the resistances of the two gauges are changing in an opposite way when the bender bends, with one increased and the other one decreased. The Wheatstone bridge is used to measure the bending strain. As shown in Fig. 2.15, the bridge is formed by two fixed resistors (R_1, R_2), and two strain gauges (R_{g1}, R_{g2}). Electrically, they are mounted in differential mode. It is the strain difference between the

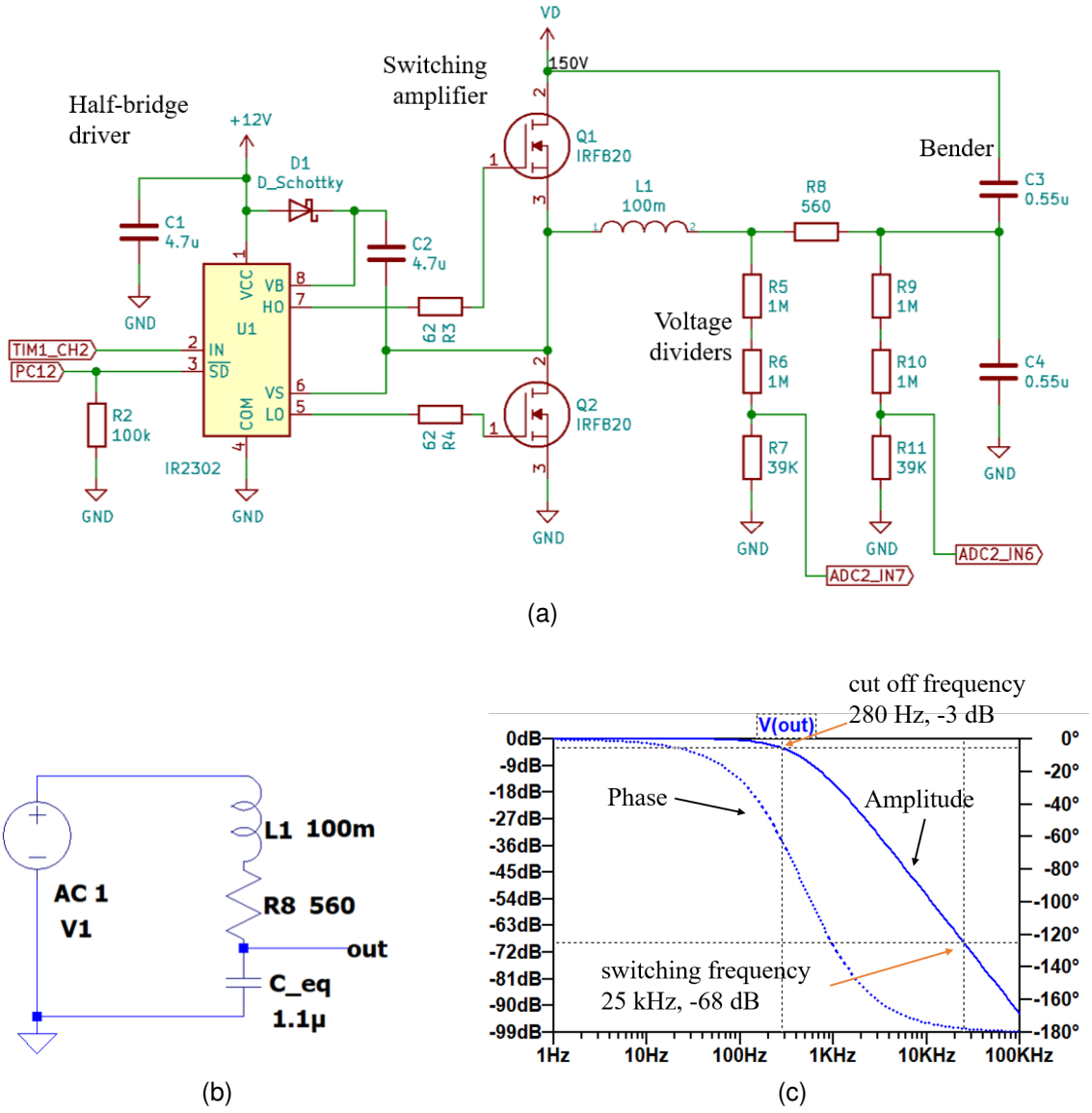

Figure 2.13: (a) Driving and measuring circuits of one piezoelectric bender. The bender is represented by its capacitance ($2 \times 0.55\,\mu F$, C_3 and C_4). AC analysis was performed with the software LTspice XVII with (b) equivalent circuit of the second order low pass filter. (c) Frequency response of the low pass filter. The solid blue curve is amplitude response and the dash blue curve is phase response.

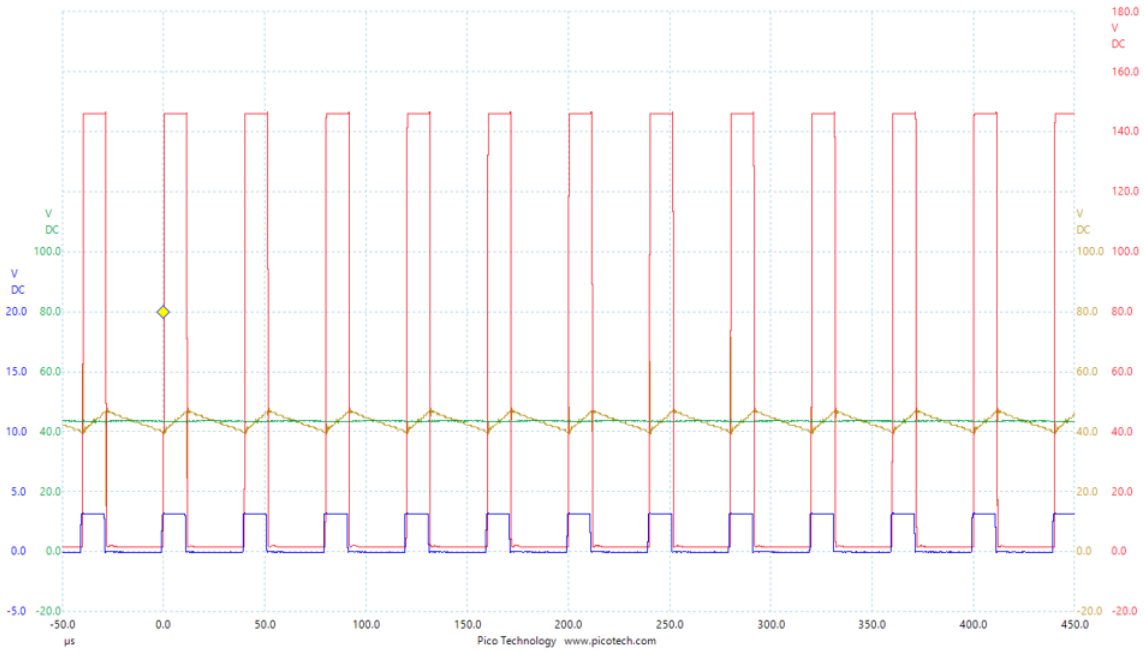

Figure 2.14: Example of pulse width modulation (duty cycle 30%). The blue curve is the pulse signal given to the half-bridge driver. The red curve is the output of the switching amplifier (the leg). The yellow curve is the voltage before the damping resistor (R_8). The green curve is the voltage after R_8, i.e., the driving voltage of the bender.

two surfaces that is measured. The output of the bridge is then amplified by an instrumentation amplifier (INA826).

It may be noticed that the output of Wheatstone bridge can be positive or negative. While DSP can only measure voltage within a range of 0 V to 3.3 V. So it is necessary to add a voltage bias. Referring to the data sheet of INA826, as shown in Fig. 2.16, an input common-mode voltage around 0.5 V leads to the widest range of output voltage. When the reference voltage $V_{\text{ref}} = 0\,\text{V}$, the common-mode voltage is restrained around 0.5 V to have the largest range of output voltage. In the case of $V_{\text{ref}} = 1.5\,\text{V}$, we have more flexible common-mode voltages to obtain the same output range. Therefore, we decided to add a reference voltage around 1.2 V, which is the average value of the output voltage. In Fig. 2.15, TL431 is used to provide a low impedance voltage reference at 1.24 V. The fixed resistors R_1 and R_2 were then selected to have a common-mode voltage around 0.5 V.

The output of Wheatstone bridge is amplified with a gain G, which can be tuned through the resistance R_G. In our case ($R_G = 200\,\Omega$), the gain G is around 250. The output of the amplifier is given by:

$$V_{\text{out}} = G\left(\frac{R_{g1}}{R_1 + R_{g1}} - \frac{R_{g2}}{R_2 + R_{g2}}\right)V_e + V_{\text{ref}} \tag{2.8}$$

where $V_e = 3.3\,\text{V}$ is the voltage supplied to the Wheatstone bridge and V_{ref} is the reference voltage.

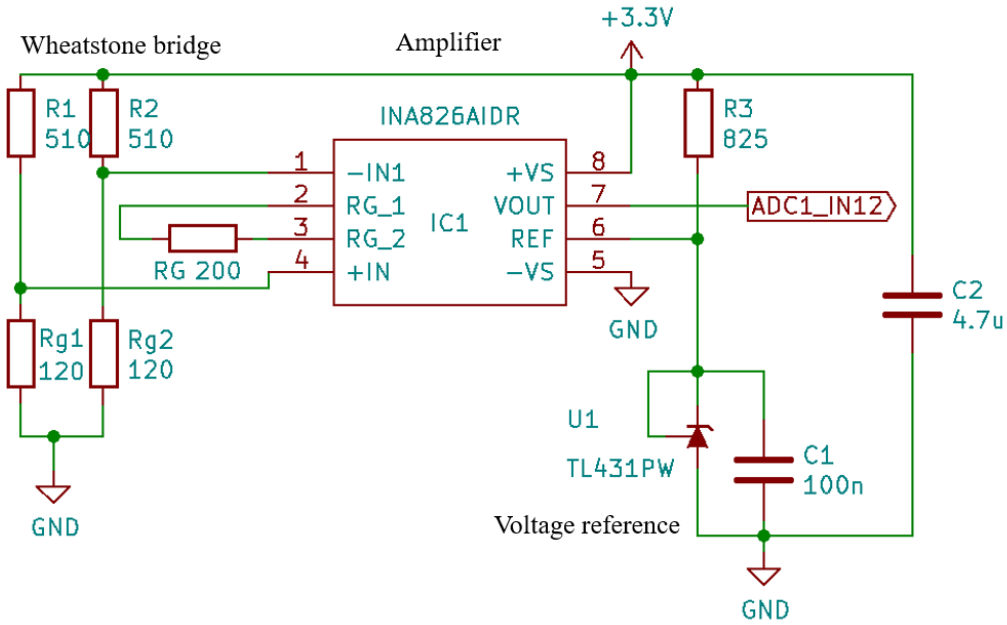

Figure 2.15: Measuring circuit of the strain (example for one piezo bender).

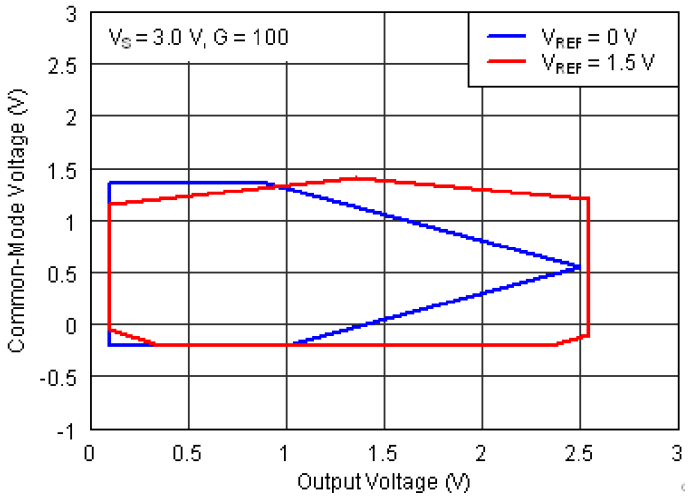

Figure 2.16: Input Common-Mode Voltage vs Output Voltage of INA826. Source from data sheet.

Table 2.6: Gauge performance when the piezo benders are driven by a sinusoidal voltage 142.5 V (peak-peak) at 1 Hz.

Related bender	Gauge bias (V)	Gauge dynamic range (mV)
UB	1.4	527
LB	1.3	509

In an ideal configuration of the two strain gauges (i.e., symmetrical), as

$$R_1 = R_2$$

$$R_{g1} = R + \Delta R$$

$$R_{g2} = R - \Delta R$$

where R is the unstressed resistance of the gauge and ΔR denotes the resistance variation of the gauge under stress, the output in (2.8) can be rewritten as:

$$V_{\text{out}} = G\frac{2\Delta R(R_1 + R)}{(R_1 + R + \Delta R)(R_1 + R - \Delta R)}V_e + V_{\text{ref}}. \tag{2.9}$$

The resistance change is proportional to the length change of the gauge, which is expressed as:

$$\frac{\Delta R}{R} = k\epsilon_{\text{ave}} \tag{2.10}$$

where $k = 2$ is the gauge factor given by the data sheet, and ϵ_{ave} is the strain of the gauge.

Since $\Delta R \ll R$, equation (2.9) can be further simplified to:

$$V_{\text{out}} = G\frac{2\Delta R}{R_1 + R}V_e + V_{\text{ref}} = G\frac{2k\epsilon_{\text{ave}}}{\frac{R_1}{R} + 1}V_e + V_{\text{ref}}. \tag{2.11}$$

Each bender is assigned with two gauges and a measuring circuit (Fig. 2.15) to measure the strain. The strain range in volts (V_{out}) is obtained by applying a low frequency sinusoidal driving voltage (3.6 V to 146.1 V) to the piezo benders. We use Upper Bender (UB) and Lower Bender (LB) to distinguish the two benders. The performance of the measuring circuits are summarized in Table 2.6. It can be seen that V_{out} is reasonably biased to 1.4 V and 1.3 V, with a dynamic range around 0.5 V. The voltage bias of the strain signal can be tuned by changing the fixed resistors of the Wheatstone bridge. It is important to have a DC bias around $V_{\text{ref}} = 1.24$ V to guarantee a sufficient dynamic measuring range of the gauge, considering possible positive or negative effects when loaded with the skin. The amplified output of the Wheatstone bridge is referred to here and in the following as the "gauge signal".

Considering the potential asymmetry in the mechanical mounting, it is reasonable to assign strain measurement circuits to each piezoelectric bender separately.

2.4 Sensing model of tip displacement and force

Concerning *in situ* measurements, simultaneous sensing of force and displacement at the bender tips is desired. The sensing principle of the actuator-sensor system is described in this section.

When subjected to voltage excitation and to an external force, the tip displacement of a clamped cantilever piezoelectric bender can be generalized from its constitutive equation (2.1) to:

$$\delta = S_{\mathrm{dv}} V - S_{\mathrm{df}} f_r \tag{2.12}$$

where S_{dv} and S_{df} represent the sensitivities of tip displacement to the supplied voltage and to the external force, respectively.

In (2.12), both δ and f_r are the desired measuring outputs of the probe. On the other hand, strain gauges are used to derive the external force perpendicular to the bender tip, by measuring the strain difference between tip-free and tip-loaded conditions, as explained by (2.7). The bending strain is determined from M_p and f_r, referring to (2.6), where M_p is a linear function of the driving voltage V [65]. Thus, the resultant strain gauge signal g can be generalized as a linear function of V and f_r:

$$g = S_{\mathrm{gv}} V - S_{\mathrm{gf}} f_r \tag{2.13}$$

where S_{gv} and S_{gf} are the sensitivities of the gauge signal to the driving voltage and to the external force, respectively.

Equations (2.12) and (2.13) state that the tip displacement and the bending strain are a linear function of applied voltage and external force, which can be summarized as below:

$$\begin{bmatrix} \delta \\ g \end{bmatrix} = \begin{bmatrix} S_{\mathrm{dv}} & -S_{\mathrm{df}} \\ S_{\mathrm{gv}} & -S_{\mathrm{gf}} \end{bmatrix} \begin{bmatrix} V \\ f_r \end{bmatrix}. \tag{2.14}$$

To achieve displacement sensing, Seethaler et al. [67] managed to estimate the tip displacement from the bending strain, thanks to the equalized sensitivity of strain to displacement under voltage and force excitation. However, this requires a special geometry layout of the strain gauges, where the gauge length should span over two thirds of the length of the bender starting from the clamped edge. Our sensing model is developed in a different way. Experimental observation shows that the relationship between the tip displacement and the bending strain is not identical when subject to voltage excitation and external force, respectively. When the bender tip is deflected the same amount, the bending strain induced by external force is larger than that due to voltage excitation, as displayed in Fig. 2.17. Hence, to build up the sensing model, we identified the sensitivities of displacement and strain in response to voltage excitation and external loads, instead of customizing the gauge length relative to the bender. This characterization of

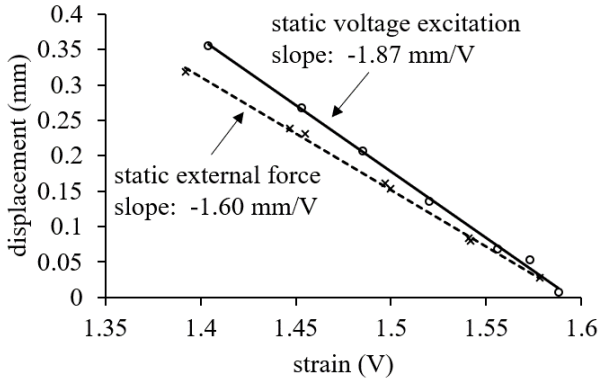

Figure 2.17: Strain-to-displacement curves in response to static voltage excitation and static tip force (perpendicular to the bending beam), respectively.

the electromechanical system is described in the next section.

For the electromechanical system, the driving voltage V and the gauge signal g are two internally accessible variables, while the external force f_r is not directly accessible. So we swap g and f_r in (2.14) to estimate the tip displacement and the force from the driving voltage V and the gauge signal g, as described by

$$\begin{bmatrix} \widehat{\delta} \\ \widehat{f}_r \end{bmatrix} = \begin{bmatrix} S_{\mathrm{dv}} - S_{\mathrm{df}} \frac{S_{\mathrm{gv}}}{S_{\mathrm{gf}}} & \frac{S_{\mathrm{df}}}{S_{\mathrm{gf}}} \\ \frac{S_{\mathrm{gv}}}{S_{\mathrm{gf}}} & -\frac{1}{S_{\mathrm{gf}}} \end{bmatrix} \begin{bmatrix} V \\ g \end{bmatrix}. \tag{2.15}$$

Here, the sensing model of tip displacement and force is established based on the variable pair (V, g).

2.5 Characterization of the electromechanical system

In this section, the responses of the piezoelectric bending actuator and the gauge sensor under electrical supply and electro-mechanical loading are investigated. To specify the identification process of the sensing parameters, we first characterized the behavior of the system considering the effects of:

- voltage frequency, which is related to the bandwidth and hysteresis;
- voltage amplitude, which also affects hysteresis behavior;
- external force.

Even though the MIP is designed for quasi-static applications, it is interesting to explore its capability or limitation in a wider frequency range. Here, we characterize the system response up to 200 Hz. A dynamic characterization up to 900 Hz is presented in the next chapter. It may be noted that in the following sections of this chapter, the tests are performed with prototype V1. The prototype V2 was processed with the same steps and gave very similar results.

2.5.1 Characterization protocol

To characterize the system, a laser displacement sensor (vibrometer, Polytec OFV-534) and a force sensor (Honeywell, FSS low profile force sensor) were employed so as to measure the tip displacement and force. The characterization apparatuses are shown in Fig. 2.18. The bending strain (in volts) is measured by the strain gauge. Data is collected by an oscilloscope (PicoScope 6). The signals and corresponding measuring devices are listed in Table 2.7. Relevant experiments were performed referring to the technical data of the bending actuator PB4NB2S, see in Table 2.8. The vibration of piezo bender is amplified when the operating frequency is close to the resonant frequency (370 Hz, no load, from data sheet). For the sake of safety, it is vital to impose a lower enough driving voltage to the piezo bender when the frequency is approaching its resonance.

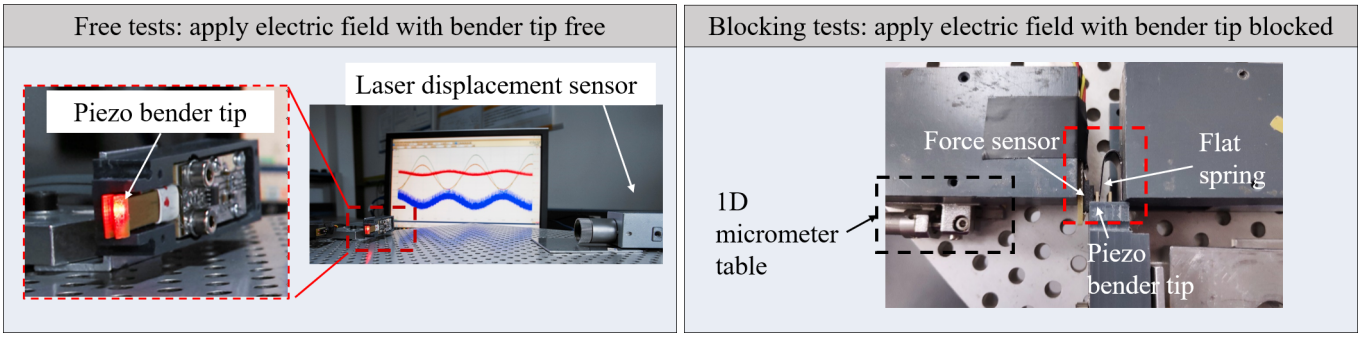

Figure 2.18: Apparatuses for free and blocking tests. (a) Free tests by supplying an electrical field. Tip displacement is measured by a laser displacement sensor. (b) Blocking tests. The piezo bender is blocked between a force sensor and a customized spring. The blocking force is measured by the force sensor.

Table 2.7: Equipment used in experiments.

Signal	Tip displacement	Tip force	Bending strain
Device	Laser sensor	Force sensor	Strain gauge

Table 2.8: Technical data of the piezoelectric bending actuator PB4NB2S.

Nominal displacement (µm @150 V)	Blocking force (N @150 V)	Resonant frequency (Hz, no load)
$\pm 450 \pm 15\%$	1.5	370

It may be noted that the driving voltage of the piezoelectric bender is ranging from 0 V to 150 V. In data processing, to correlate with positive and negative displacements, a centering voltage 75 V is subtracted from the original driving voltage. This leads to a voltage varying from -75 V to 75 V in all related figures. To take precautions, we limited the full-scale voltage from 150 V to 143.5 V (peak-to-peak). For the gauge signal, the DC bias obtained from centering position (no deflection of the bender) is removed.

2.5.2 Effects of voltage frequency and amplitude on tip-free and tip-blocked tests

2.5.2.1 Applying full-scale sinusoidal voltage (tip free)

To study the effects of the supply frequency, the behavior of the electromechanical system was first characterized by applying sinusoidal voltage excitation with frequencies varying from 1 Hz to 200 Hz, while the tip was free. Fig. 2.18a shows the setup for tip-free tests. The commands with a full-scale voltage at different frequencies were given to the DSP. As shown in Fig. 2.19a, the hysteresis behavior between the input voltage and output tip displacement remains similar when the working frequencies are relatively low (below 100 Hz). While the loop size and inclination of the curves start to change from 100 Hz. The width of the hysteresis loop is increased at a frequency of 200 Hz. This may be caused by the combination of hysteresis and viscous effects [68]. Another cause to the different behavior at 200 Hz could be the operating frequency, which is close to the resonance one. The voltage-to-bending strain curves show similar behavior, see in Fig. 2.19b. Plotting the strain-to-displacement curves (Fig. 2.19c), the output displacement is found to be linear to the strain when no external force is applied.

To sum up, the behavior of piezo bender is not affected by the working frequency when it is below 100 Hz. Specifically, the voltage-displacement relationships maintain the same if the frequency is lower than 100 Hz. Same conclusion is drawn for the bending strain as a function of the driving voltage. Moreover, the tip displacement is linear to the bending strain. No significant change is observed between the bending strain and displacement when the driving frequency is increased from 1 Hz to 200 Hz.

2.5.2.2 Varying voltage amplitude (tip free)

The effects of voltage amplitude are demonstrated in Fig. 2.20. The piezoelectric bender was driven at 10 Hz under four different voltage amplitudes and no external force was applied. To have a better presentation of minor loops, we used a Savitzky-Golay filter in MATLAB to smooth the raw data. It can be seen that minor loops and major loop are both exhibited in the voltage-to-displacement curves (Fig. 2.20a) and the voltage-to-strain curves (Fig. 2.20b). The loop size (hysteresis width) and the loop inclination are varied with the voltage amplitudes. Whereas, no hysteresis loop is presented in the displacement–strain curves. As seen in Fig. 2.20c, the relationship between the strain and tip displacement is not changed with the voltage amplitudes in no load case.

The tip-free tests under varying frequencies (up to 200 Hz) and under varying amplitudes demonstrate that the frequency and amplitude of the driving voltage have impacts on voltage-to-displacement and voltage-to-strain relationships. The effects of frequency can be neglected if it is below 100 Hz. Nonetheless, the strain-to-displacement relationship remains the same for all the frequencies and amplitudes studied under tip-free condition.

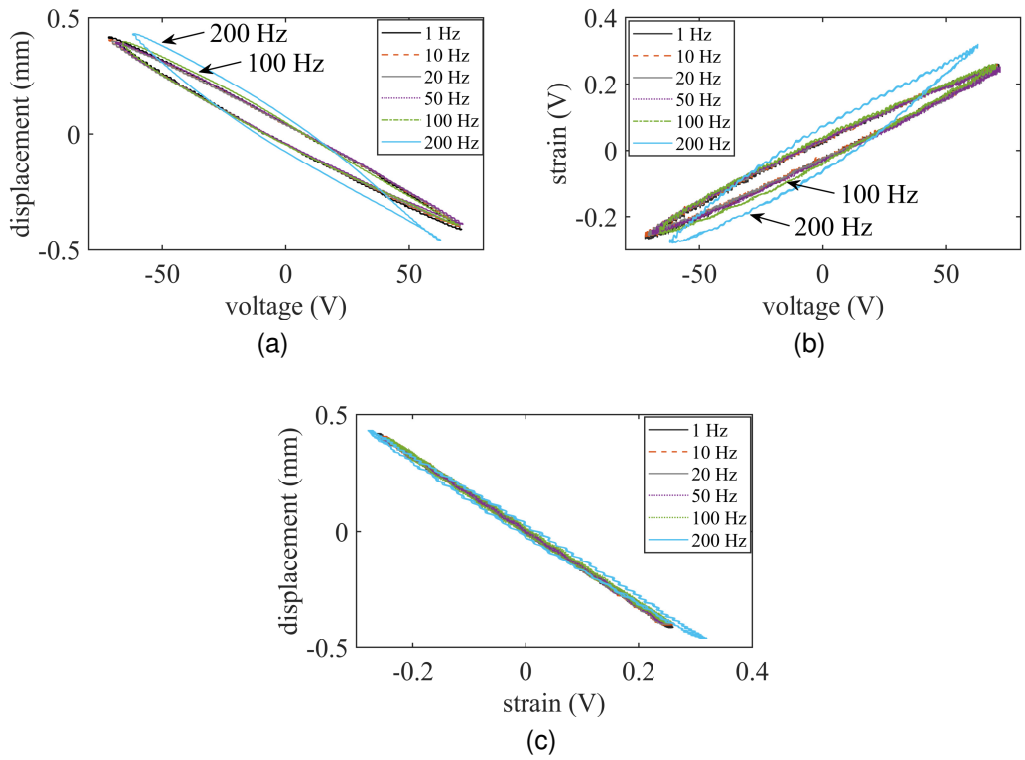

Figure 2.19: System responses to high voltage excitation at various frequencies (a full-scale voltage command was sent to the DSP). Tip displacement δ (a) and bending strain g (b) in response to voltage excitation V. The relationship between displacement and bending strain is presented in (c).

2.5.2.3 Applying full-scale sinusoidal voltage and external force (tip blocked)

To further study the system response when an external force is applied, we performed blocking tests by applying a sinusoidal voltage to the piezo bender and blocking its tip with a setup shown in Fig. 2.18b.

The blocking force and the corresponding output bending strain are shown in Fig. 2.21. A quasi-linear relationship is found between the driving voltage and the blocking force (Fig. 2.21a). For the voltage-to-strain curve, no significant hysteresis loop is observed in blocking tests (Fig. 2.21b) compared to the curves obtained under free tests (Fig. 2.19b). Experimental results show that the hysteresis phenomena are significantly reduced when the bender tip is blocked under full-scale voltage supply (tested up to 100 Hz).

As a general conclusion for this subsection 2.5.2, when the bender tip is free, the voltage frequency (above 100 Hz) and voltage amplitude affect the displacement curves with hysteresis phenomena. Likewise, these are shown in the bending strain signal. But the strain-to-displacement curves are linear. On the other hand, when the bender tip is blocked, a quasi-linear relationship is found between the blocking force and voltage.

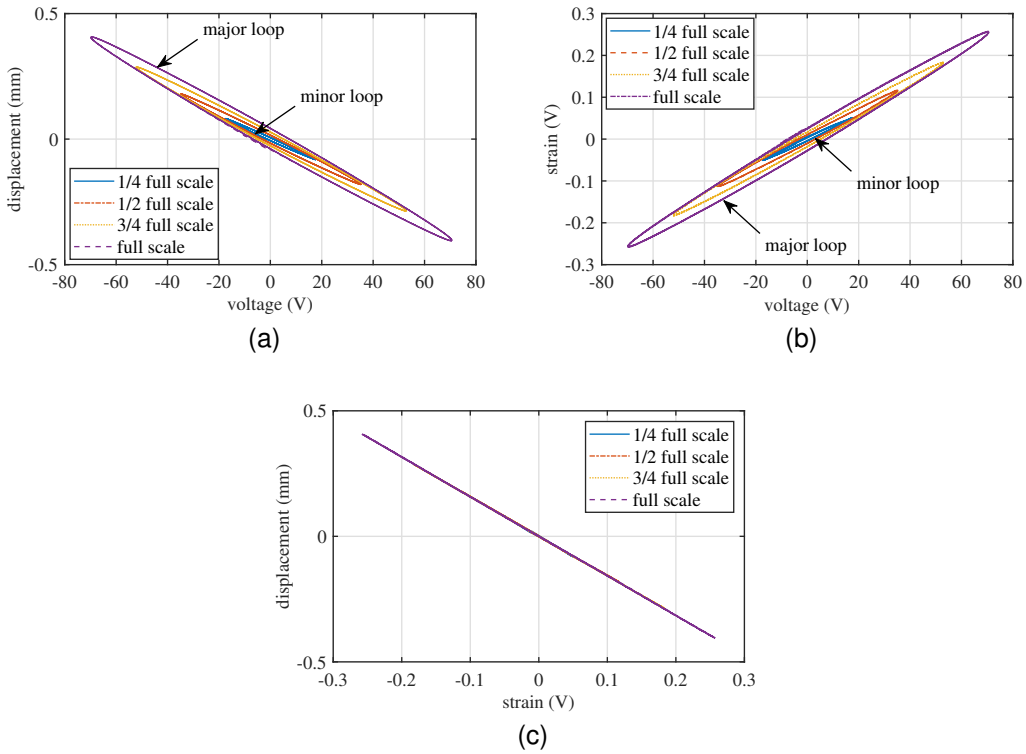

Figure 2.20: Effects of voltage amplitude, input frequency 10 Hz (tip free). Displacement responses are plotted in (a) and strain responses are plotted in (b). Strain-to-displacement curves are presented in (c). Data were smoothed using a Savitzky-Golay filter.

2.6 Identification of sensing parameters

The effects of frequency and amplitude of the voltage supply have been explored in previous section. Based on these results, an identification protocol was developed to obtain the sensing parameters (S_{dv}, S_{gv}, S_{df}, and S_{gf}) in the model (2.15) from two types of tests, termed as free and blocking tests. System characterization (in section 2.5) has demonstrated that below 100 Hz, the piezo bender behaves the same, whatever the supply frequency. Thus, we chose to perform the tests with full-scale voltage excitation at 1 Hz.

- Free tests, bender tip free ($f_r = 0$)

  We excite the piezo benders with the full-scale voltage at 1 Hz. When the bender tip is free, S_{dv} and S_{gv} can be identified as follows:

$$S_{\mathrm{dv}} = \frac{\mathrm{d}\delta}{\mathrm{d}V}|_{f_r=0} \qquad\qquad S_{\mathrm{gv}} = \frac{\mathrm{d}g}{\mathrm{d}V}|_{f_r=0}. \tag{2.16}$$

  The tip displacement (free stroke) is measured by the laser sensor. Fig. 2.18a depicts the setup for free tests. To have a better focus of the laser beam, two 1D micrometer tables are used to fine-tune the relative positions between the bender tip and the vibrometer sensor head.

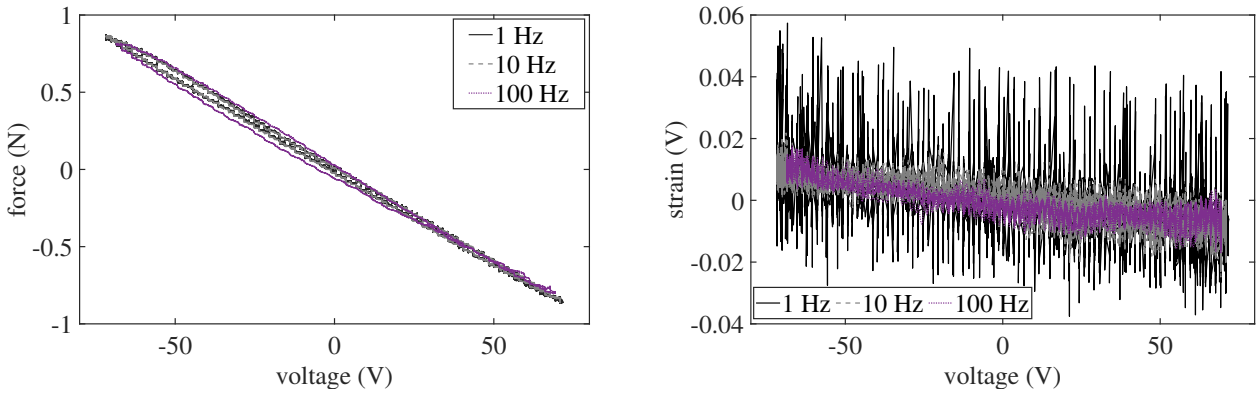

(a) (b)

Figure 2.21: Blocking force (a) and strain (b) when the piezo bender is subject to full-scale sinusoidal voltage with its tip blocked.

- Blocking tests, bender tip blocked ($\delta = 0$)

  We apply the same voltage excitation to the piezo benders as in free tests and block the bender tip. The experimental setup used for blocking tests is shown in Fig. 2.18b. The bender tip is blocked between the high stiffness external force sensor and a customized flat spring. The force sensor is fixed to a 1D micrometer table, which can be adjusted to maintain a centered position ($\delta = 0$) of the bender tip. The spring, attached to a 1D micrometer table, is used to keep the bender tip in contact with the force sensor, such that we can measure the full dynamic range of blocking force when subjected to a sinusoidal voltage. In practice, the spring was prestrained to provide a large enough biased force to block the bender tip.

  In blocking tests, the strain gauge signal, blocking force and the driving voltage are collected. The force factor N of the piezoelectric bender and the gauge coefficient κ are obtained by

$$N = \frac{\mathrm{d}f_r}{\mathrm{d}V}|_{\delta=0} \qquad \kappa = \frac{\partial g}{\partial V}|_{\delta=0}. \tag{2.17}$$

  With $\delta = 0$, S_{df} and S_{gf} can be derived from (2.12) and (2.13) by

$$S_{\mathrm{df}} = \frac{S_{\mathrm{dv}}}{N} \qquad S_{\mathrm{gf}} = \frac{S_{\mathrm{gv}} - \kappa}{N}. \tag{2.18}$$

Parameters S_{dv}, S_{gv}, κ, and N are identified directly through linear regression of the curves at $1\,\mathrm{Hz}$, i.e., free stroke (Fig. 2.19a), gauge signals under free and blocking conditions (Fig. 2.19b and Fig. 2.21b), and blocking force (Fig. 2.21a) against the supplied voltage, respectively. Then, S_{df} and S_{gf} are calculated from (2.18). The identification results are listed in Table 2.9. Finally, an estimator of the tip force and displacement can be established with (2.15).

Table 2.9: Identified sensing parameters.

Free tests		Blocking tests		Derived	
S_{dv} (mm/V)	S_{gv} (V/V)	N (N/V)	κ (V/V)	S_{df} (mm/N)	S_{gf} (V/N)
-0.005671	0.003562	-0.011771	-0.000117	0.481820	0.312572

2.7 Experimental validation of the sensing model

In this section, the sensing model of the MIP, relying on (2.15), is validated and evaluated. First, we validate and evaluate the sensing model with the same data used for identification and then with new experimental data.

2.7.1 Self validation

We estimated tip displacement and force under tip-free and tip-blocked conditions and compared them with the measurements given by the external laser sensor and the force sensor. The estimated tip displacement matches well with the measured values in free tests (Fig. 2.22, top right). A null tip displacement is expected for the blocking tests, and the error range shown in Fig. 2.22 (bottom right) is 36 µm, around 4% of the full-scale displacement (900 µm, see in Table 2.8). As for the tip force, the estimated blocking force matches with the measured one (Fig. 2.22, bottom left). However, when the tips are free (Fig. 2.22, top left), the force estimation shows discrepancy with the reality, where the force is null. The error range of force sensing is 0.2 N, around 13% of the force measurement range (1.5 N, see in Table 2.8). We can conclude that with the linear sensing model (2.15), the estimation of displacement is accurate for tip-free and tip-blocked cases, while the force estimation shows large hysteresis when the bender tips are free.

2.7.2 Validation with new experimental data

Afterwards, the robustness of the sensing model was further validated with two intermittent cases (a succession of free and blocking cases) by hard stops at two different positions. The setup is depicted in Fig. 2.23. The benders are still driven by a sinusoidal full-scale voltage at 1 Hz. The external force sensor and the laser sensor are used to measure tip force and displacement. The force sensor, which also loads the bender tip, is placed at two different positions by adjusting the 1D micrometer table toward or away from the bender tip. These two positions result respectively in a large external force and a smaller one. Signals measured by the force sensor and laser sensor, the driving voltage and the gauge signal were collected through the oscilloscope (PicoScope 6) with a digital low pass filter at 1 kHz. The estimates from the sensing model are compared to the measurements, as shown in Fig. 2.24. The bender bends freely when it is not in contact with the force sensor, and the external force is null. Once the bender contacts the force sensor, the bender tip is stopped by the force sensor. The force increases as the driving voltage increases, while the displacement should not change. As a result for the large force, the maximum displacement error

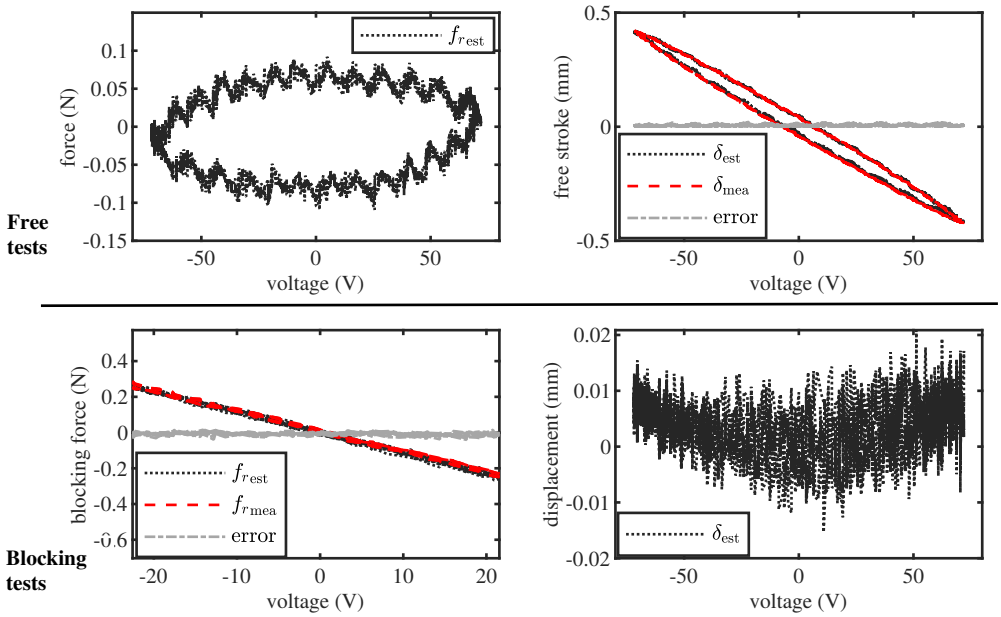

Figure 2.22: Sensing performance under extreme cases (tip free and tip blocked). Estimated force and displacement ($f_{r\text{est}}$, δ_{est}) are compared to measured results ($f_{r\text{mea}}$, δ_{mea}). The piezoelectric benders were subject to a full-scale voltage at 1 Hz. Top row: free tests, under voltage excitation only. Bottom row: blocking tests, under voltage and force excitation.

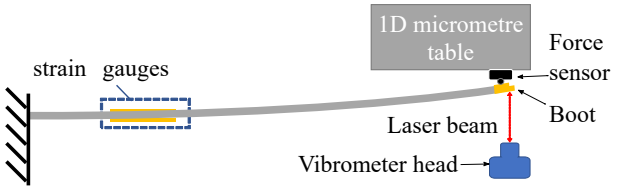

Figure 2.23: Setup for sensing validation.

is about 3.6% of the full scale, while the maximum force estimation error is 4.1%. However, when the force is smaller and the displacement is larger, the error in displacement is 5.3%, which is still acceptable, but the force estimation error becomes 11.1%, which is not acceptable.

This validation with new data is consistent with the self validation. The displacement is relatively large under low force level, which leads to a less accurate force sensing. Considering the normalized root-mean-square error (NRMSE), the force sensing error becomes significant, about 33.0% at small force level, which correlates with a relatively large displacement as seen in Table 2.10. Overall, the displacement sensing is satisfying, while the force sensing is influenced by hysteresis, especially at large displacements. Hysteresis issue and compensation strategies are discussed in the next chapter.

2.8 Application to phantom skin measurements

With the sensing model validated, the next step is to investigate the capability of the MIP to discriminate different materials. The discrimination capabilities of the MIP are evaluated with phantom skins. Three

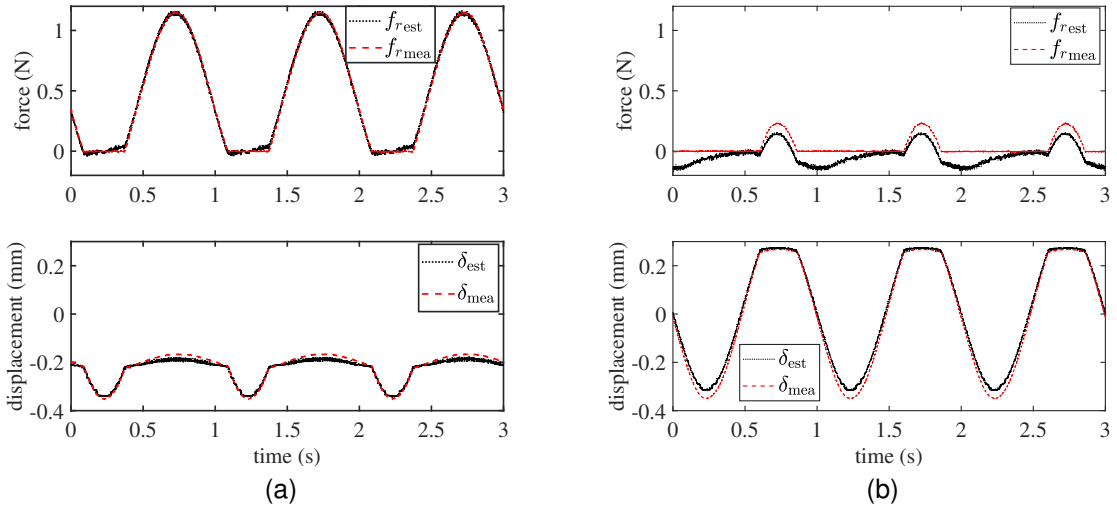

Figure 2.24: Sensing model validation under voltage and force excitation. (a) Hard stop around -0.21 mm. (b) Hard stop around 0.25 mm. The black dot curves present the estimated force and displacement ($f_{r\,\mathrm{est}}$, δ_{est}) and the red dash curves are the measured results ($f_{r\,\mathrm{mea}}$, δ_{mea}).

Table 2.10: Error analysis of the sensing model (with data from self validation and new validation experiments): the root mean square error is normalized by the observed range (NRMSE).

Loading condition	Displacement range δ_{mea} (µm)	NRMSE: $f_{r\,\mathrm{est}}$	NRMSE: δ_{est}
Tip free (voltage excitation only, $f_r = 0$)	842	N/A	0.9%
Small force level (voltage and external force)	618	33.0%	3.7%
Larger force level (voltage and external force)	185	1.6%	7.3%
Tip blocked (voltage and external force, $\delta = 0$)	N/A (assumed 0)	1.0%	N/A

N/A: not applicable.

types of phantom skins were prepared with the Dragon Skin™ series of silicone elastomers. They are Dragon Skin™ FX-Pro™, Dragon Skin™ 10 SLOW and Dragon Skin™ 20, corresponding to a Shore A hardness of 2, 10, and 20, respectively. We use DS_FX, DS_10 and DS_20 to refer to these three phantom skins.

2.8.1 Calibration of the phantom skins

To classify the three phantom skins in terms of stiffness, we calibrated them, based on static indentation tests. We used the MIP itself to indent the phantom to maintain the same normal loading conditions as for the next tangential traction tests. As shown in Fig. 2.25, the MIP is moved up/down manually with the help of a translation stage. A dial gauge (range 25 mm, resolution 0.01 mm) is used to measure the displacement in normal direction (along the probe length). A weighing scale (BP410, Max 410 g, resolution 0.01 g) is employed to measure the normal force F_n. The initial values are recorded when the bender tips (covered by boots) are not in contact with the phantom skin, as well as the readings at each target force level (0.1 N, 0.2 N, and 0.5 N).

It may be noted that the scale pan also has a normal displacement when loaded. Therefore, the dial

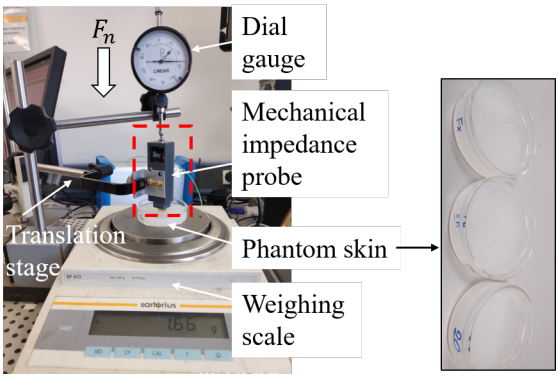

(a)

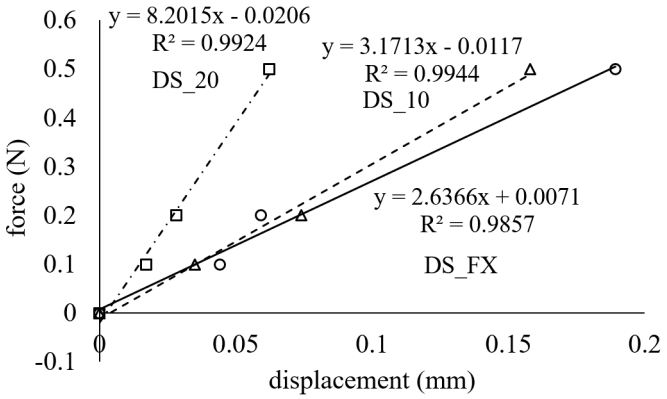

(b)

Figure 2.25: Phantom skin calibration under static indentation. (a) Apparatus for indentation tests. (b) Calibration results.

gauge measures the sum of the phantom displacement under indentation and the displacement of the scale pan. To obtain the indentation depth of the bender tips, the displacement of the scale pan should be subtracted from the global displacement. The normal displacement of the scale is obtained by directly loading the scale with the dial gauge. The force–displacement characteristics calibrated from indentation tests are shown in Fig. 2.25b. It can be seen that phantom DS_20 is the stiffest one. The stiffness of phantoms DS_FX and DS_10 are close and DS_10 is slightly stiffer.

2.8.2 Case study: influence of frequency and normal force on tangential properties

In real application, the probe characterizes material properties through tangential traction. To perform uniaxial stretch, a certain normal load is needed to grip the material between the two boots. Before studying the discrimination capability of the probe, the effects of normal force F_n on lateral stiffness are investigated with the softer phantom DS_FX. As the force and displacement estimations are validated only for low frequencies (below 100 Hz), the tests were performed with a frequency range of 1 Hz to 100 Hz. A sinusoidal frequency sweep signal was employed, with an amplitude around 60% of full-scale voltage to prevent any risk to the probe. Fig. 2.26 shows the test bench for tangential traction tests. The MIP is placed against

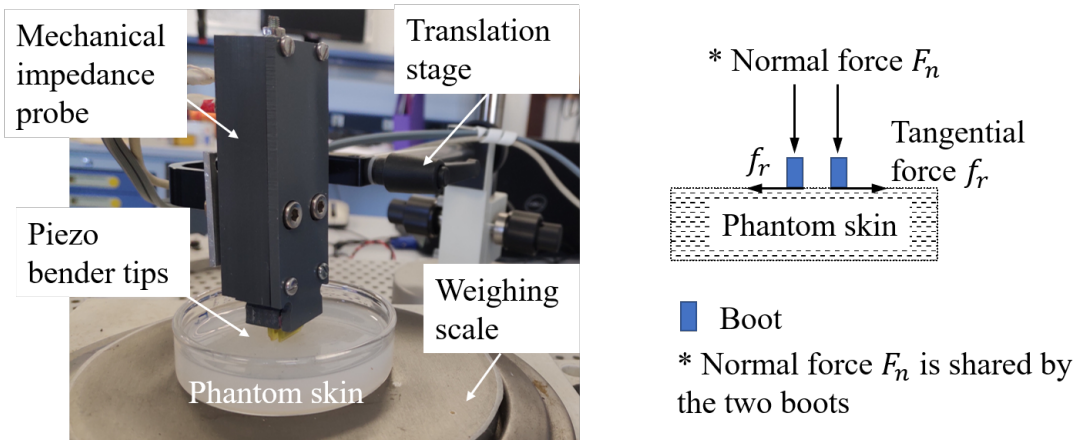

(a) (b)

Figure 2.26: (a) Apparatus for tangential traction tests on phantom skin. (b) Loading conditions on the phantom surface. Normal and tangential forces are applied.

the phantom skin. An articulated arm is used to hold the MIP vertically and to apply the desired normal force. The MIP is first moved up/down through the translation stage to preload the phantom skin to a target normal force level (0.1 N, 0.2 N, and 0.5 N). Then, the frequency sweep signal is applied to deform the phantom skin laterally. As depicted in Fig. 2.26b, the surface of phantom skin is subjected to combined normal and tangential forces.

The raw data (driving voltages and gauge signals) were collected through the oscilloscope (Picoscope 6) at a sampling rate of 30 kHz and filtered by a digital low-pass filter with a cutoff frequency of 1 kHz. The collected data were further processed with MATLAB. A Savitzky-Golay filter was applied to smooth data. Then, the lateral displacement and force were calculated from the estimator (2.15). Considering the fact that the phantom skin was deformed between the two bender tips, the global displacement was calculated by summing the displacement of each bender. While for the global force, it was determined by averaging the estimated force of each bender.

The frequency response of stiffness (N/mm) in the tangential direction is obtained using fast Fourier transform in the frequency domain. It can be seen in Fig. 2.27 that the stiffness of the Dragon Skin (DS_FX) in decibel is nearly constant over the frequency range of two decades.

The magnitude of stiffness in the tangential direction rises with the increased normal force (Fig. 2.27). While the phase between force and displacement is reduced with an increased F_n. Fig. 2.28 shows that such increment of tangential stiffness is proportional to that of the normal force. With the frequency ranging over two decades (1 Hz to 100 Hz), the stiffness of phantom DS_FX is increased around 48% from 0.93 N/mm to 1.39 N/mm when $F_n = 0.5$ N. The phantom tests with varying F_n suggest that the characterized mechanical properties in tangential direction are affected by the preload in normal direction. So the normal force F_n should be controlled to have comparable results.

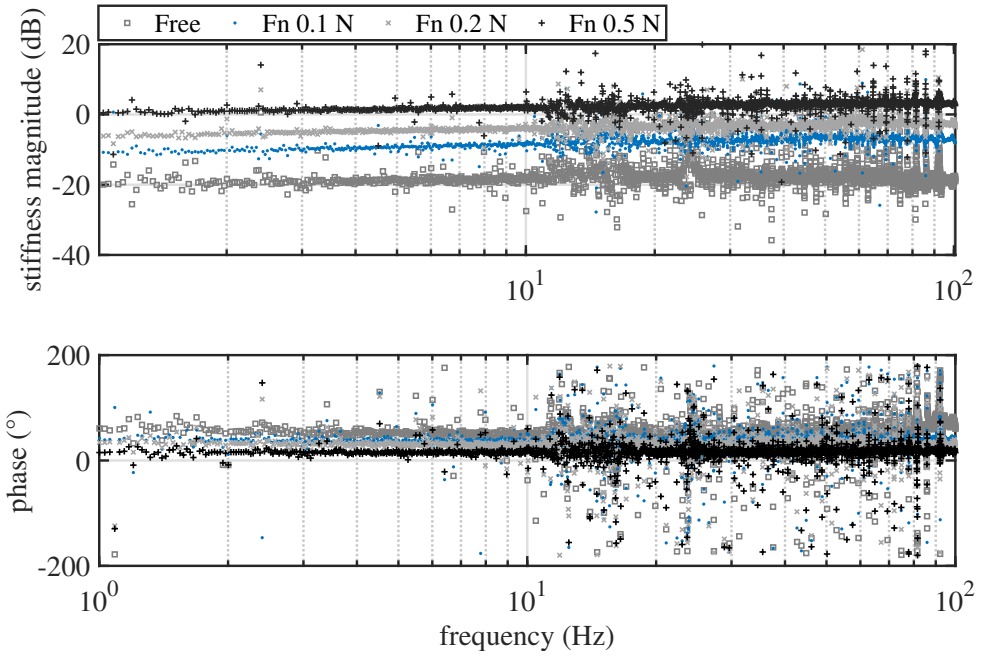

Figure 2.27: Frequency response of phantom DS_FX in the tangential direction.

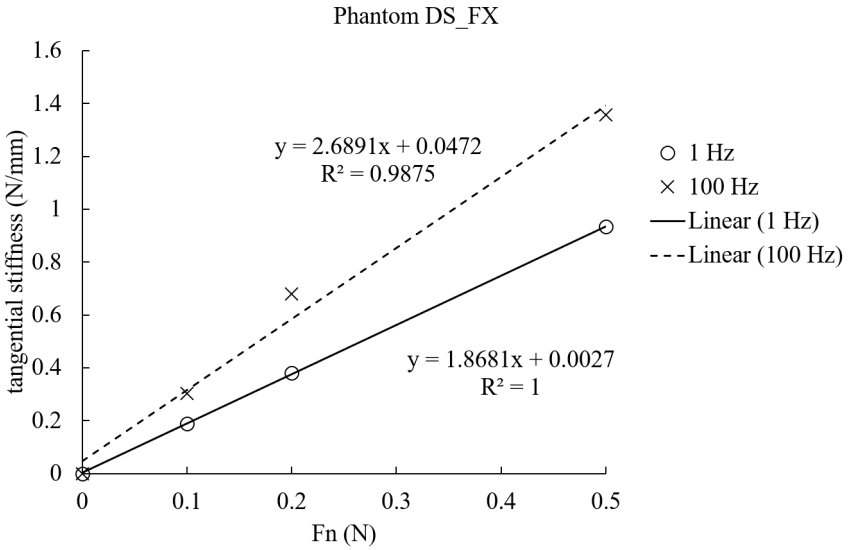

Figure 2.28: Tangential stiffness of the phantom DS_FX as a function of normal force. Results at 1 Hz and 100 Hz are presented. The stiffness when the bender tips are free is subtracted.

2.8.3 Tangential traction tests on different phantoms

To justify the discrimination function of the MIP, tangential traction tests were conducted on the three phantom skins mentioned above with the same apparatus presented in Fig. 2.26. It is expected that the MIP can distinguish the phantom skins featured with different stiffness. For this study, the normal force was controlled to $0.5\,\mathrm{N}$. The piezo benders were excited by a up-chirp and down-chirp signal (from $1\,\mathrm{Hz}$ to $100\,\mathrm{Hz}$, then back to $1\,\mathrm{Hz}$), and a voltage amplitude around 60% of full scale. The data were collected through DSP with a sampling rate of $625\,\mathrm{Hz}$. The data were processed as below:

- Remove biases from the original driving voltages and gauge signals. The biases correspond to the values when the bender tips are in their centering positions (no deflection).
- Smooth data or add filter if necessary.
- Estimate tip force and displacement using the identified estimator (2.15).
- Analyze data in time domain or frequency domain.

Representative force–displacement curves when the bender tips are free and loaded by phantoms are displayed in Fig. 2.29. For loaded cases, the slope of force–displacement curve is increased slightly with the increasing of the excitation frequency. When the bender tips are free, a hysteretic force (defined as the maximum gap of the loop) is present with a value around $0.08\,\mathrm{N}$. When the bender tips are loaded with the phantom skins, the hysteretic force can reach $0.2\,\mathrm{N}$ or even larger for DS_20. For this hardest phantom DS_20, the hysteresis loops between displacement and force at $1\,\mathrm{Hz}$ and $10\,\mathrm{Hz}$ differ from the others, as the force stops increasing with displacement at some moments. These abnormal curves may result from a slip between the probe and the phantom skin. It can be seen that this low frequency issue is pretty repeatable as the loops obtained at up-chirp frequencies are very close to the ones obtained at down-chirp frequencies. Moreover, compared to the softer phantom skins DS_FX and DS_10, the force–displacement curves of the hardest phantom DS_20 are less symmetrical about the origin 0, but shifted lower right. A larger positive displacement is observed than the negative displacement. This may be explained by the fact that the bender tips were pre-stretched with the unbalanced normal loads on the two benders during the tests of the hardest phantom DS_20. Whereas, for the softer phantom skins, it seems easier for them to accommodate and maintain centering positions when we place the bender tips against the phantom skins. For phantom DS_20, the displacement-force curves become similar to the other cases, when the frequency is increased to $100\,\mathrm{Hz}$. The slip seems disappeared as the displacement reduced.

To investigate the "slip" issue presented in DS_20 (Fig. 2.29) and justify the results obtained under $100\,\mathrm{Hz}$, the phantom DS_20 was tested again. The frequency sweep signal was lowered by half, which limits the voltage amplitude to $22\,\mathrm{V}$, about 30% of the full scale. Accordingly, the vibration amplitude was reduced as well. For these rechecking tests, the sampling rate was programmed to adjust according to the voltage frequency. A sampling rate of $\frac{25}{3}$ kHz was used for voltage frequency ranging from $10\,\mathrm{Hz}$ to $90\,\mathrm{Hz}$ and for higher frequencies, a full speed sampling rate of $25\,\mathrm{kHz}$ was used. No more "slip" issue is presented

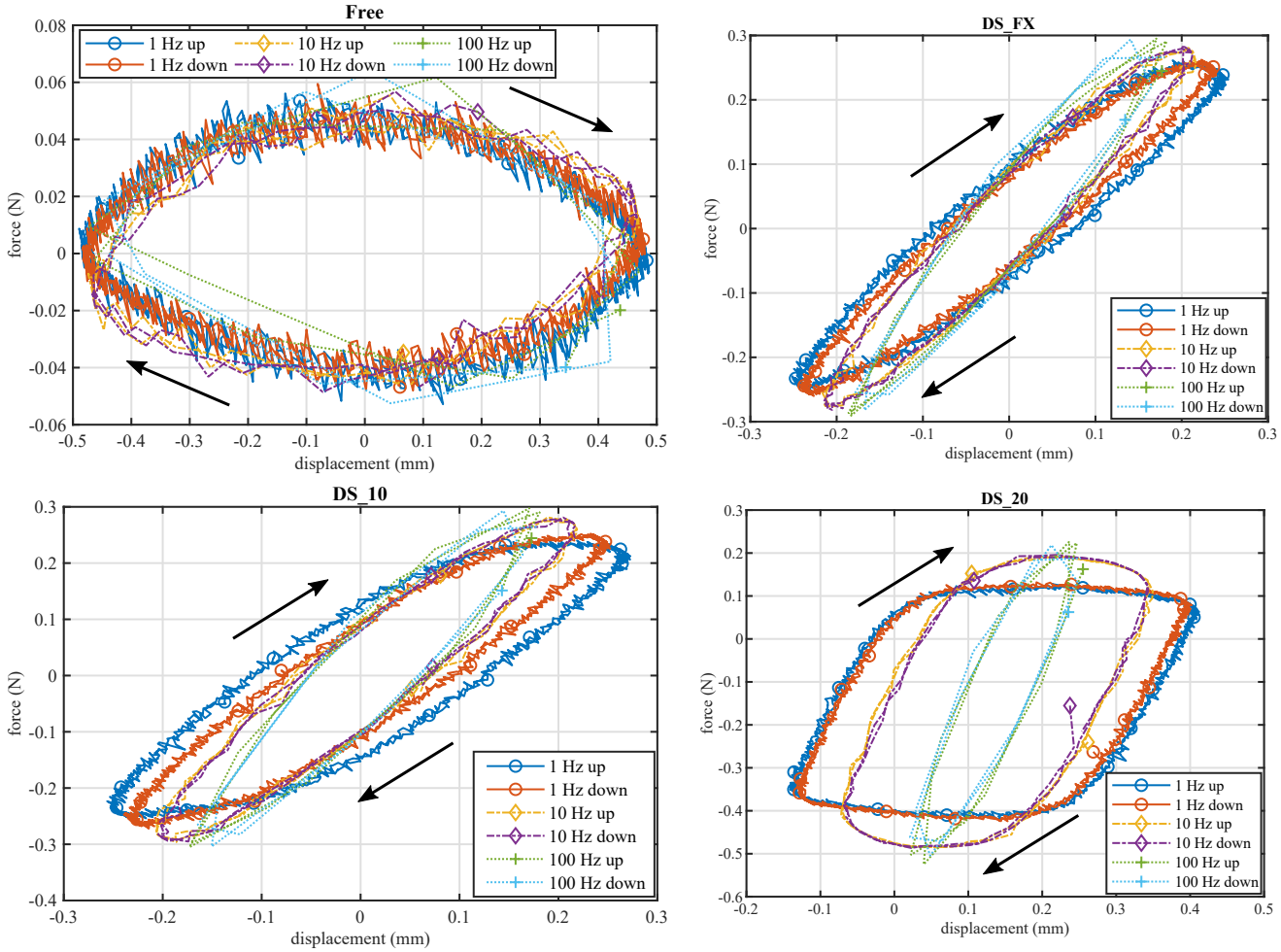

Figure 2.29: Force–displacement curves characterized under a frequency sweep of voltage, amplitude 44 V (60% of full scale). Results from 1 Hz, 10 Hz and 100 Hz are presented. Up and down denote that the frequency is along up- and down-chirp directions, respectively. The arrows show the loop direction.

in Fig. 2.30 when the displacement is reduced. In comparison with the curves obtained at 100 Hz, 60% of full-scale voltage, a very close inclination is observed for the curves obtained with the voltage lowered by half. This tends to confirm the curves of DS_20 at 100 Hz in Fig. 2.29.

The tangential stiffness of phantom skins under 100 Hz are compared in Fig. 2.31. It can be seen that under tangential traction, the phantoms DS_FX and DS_10 behave similarly and the phantom DS_20 is the hardest one. Linear regression is applied to the curves in Fig. 2.31 to identify the stiffness magnitude of each phantom. The corresponding stiffness from up-chirp and down-chirp are averaged and listed in Table 2.11. Results obtained under a lower voltage excitation at 10 Hz and 100 Hz are also included. Although tensile strength and stiffness are not equivalent, the relative relationship between the three phantom skins is consistent in terms of tensile strength (given in the manufacturer's data sheet) and stiffness (calibrated under static indentation). For example, the tensile strength of phantom skin DS_20 is approximately three times that of DS_FX, and the calibration results under static indentation show the some relationship. This further validates the calibration results obtained in subsection 2.8.1. The stiffness order of the three phantom skins obtained from the tangential traction tests is the same as that obtained from the indentation tests.

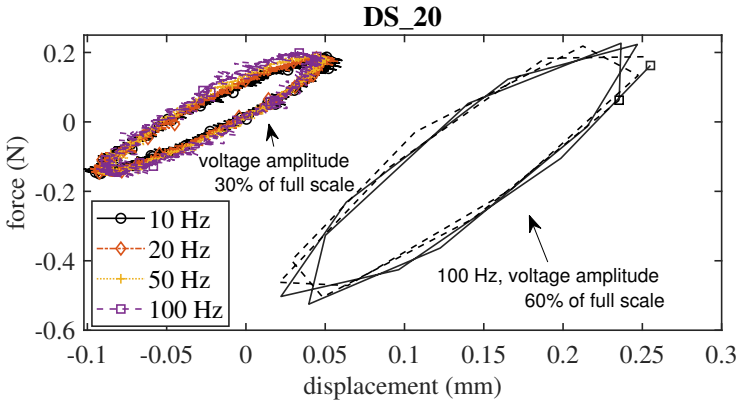

Figure 2.30: Phantom DS_20 retested with a lower voltage amplitude 22 V, about 30% of full scale. Results obtained at 100 Hz under voltage amplitude about 60% of full scale are plotted as a comparison.

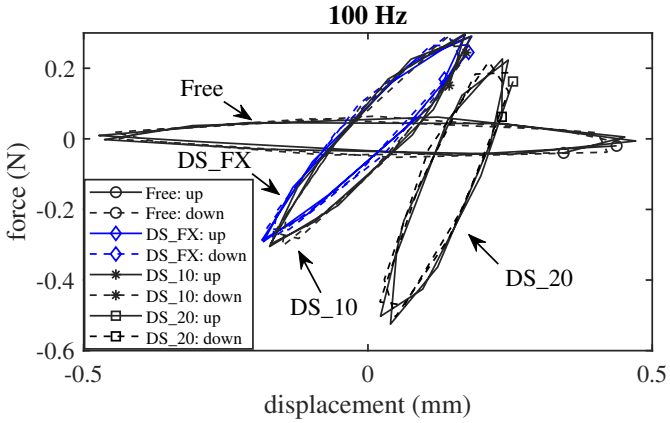

Figure 2.31: Lateral stiffness comparison when the bender tips are free and loaded by phantoms under 100 Hz sinusoidal voltage excitation, amplitude 44 V (60% of full scale).

As shown in the indentation tests, the DS_FX and the DS_10 are very close in stiffness and the DS_20 is the stiffest, which are also highlighted by the tangential traction test results. The orientation dependency may explain the stiffness differences between indentation tests and tangential traction tests. It was observed in [69] that the compressive stress of 100% filled Dragon Skin in Z direction was higher than that in X direction.

In conclusion, the MIP can distinguish different materials through tangential traction, which is verified by the tests on phantom skins.

Table 2.11: Characterization of phantom skins.

Phantom skin	Tensile strength (psi): data sheet	Stiffness (N/mm)				
		Static indentation	Tangential traction (voltage amplitude 44 V)		Tangential traction recheck (voltage amplitude 22 V)	
			10 Hz	100 Hz	10 Hz	100 Hz
DS_FX	288	2.64	1.27	1.51	/	/
DS_10	475	3.17	1.30	1.60	1.65	1.88
DS_20	550	8.2	issue	2.88	2.15	2.41

/: no data available, the phantom DS_FX was not tested.

2.9 Conclusion

A portable MIP was designed to characterize skin mechanical properties *in vivo*. This MIP consists in two piezoelectric bending actuators and two pairs of strain gauges. This chapter describes the design of the probe, including mechanical assembly and electrical circuits. We justified the mechanical structure and electrical circuits through simulation and experiments. The prototype was evolved from V0 to V1 and V2. Thanks to the interesting properties of the bender PB4NB2S from ThorLabs, the clamped cantilever structure was implemented instead of the dual-pinned structure.

A linear sensing model was established to estimate the force and displacement simultaneously from the driving voltage and gauge signal. System characterization suggests that the sensing model is valid up to 100 Hz. The performance of the sensing model was experimentally validated. The ability of the MIP to discriminate between different materials was verified by application to phantom skins. Additionally, the normal force should be handled carefully, as it linearly affects the tangential stiffness of the phantom skin. This is the main motivation for the design of prototype V2, which is capable to measure normal force with an embedded force sensor.

Here, we mainly consider the quasi-static behavior of the piezoelectric bender. In the next chapter, dynamic modeling will be introduced for control purpose. Hysteresis issue and compensation will also be discussed.

Chapter 3

System modeling, identification, and control

3.1 Introduction

In the previous chapter, we have highlighted the presence of hysteresis effect on the force measurement with our probe. This can be a critical issue for the accuracy of skin measurement. Therefore, the objective of this chapter is to propose different approaches to compensate this effect.

The force sensing accuracy can be improved either by hysteresis modeling or through a closed-loop displacement control. The two strategies both rely on the hypothesis that the hysteresis is dependent on the instantaneous displacement. The former strategy requires precise identification of the hysteretic parameters and involves derivative processes. A second compensation strategy is proposed, based on closed-loop displacement control. Given a specified motion path, a same hysteretic behavior is expected for the piezoelectric bending actuator, in tip-free and tip-loaded conditions. Within the framework of displacement control, we can derive the tip force from the voltage difference between loaded and unloaded cases. In order to achieve the closed-loop displacement control, a dynamic identification has been performed. In the previous chapter, we have investigated the system response for frequencies lower than 200 Hz. Here, we start with profiling the dynamic response of the system. This step is used to find the resonant frequency and bandwidth of the system. In the end, the compensation strategies are experimentally validated by applying a spring load. The system performance on estimation and control are evaluated.

3.2 Dynamic model and identification

3.2.1 Dynamic system characterization

As a preliminary study to achieve hysteresis compensation, it is necessary to identify the dynamic behavior of our system. A first step towards identification is performed in this section, to define which variables

are relevant to achieve the dynamic identification. The electromechanical system can be divided into two subsystems, composed of the electrical drive on one hand and the actuator-sensor part on the other hand, as illustrated in Fig. 3.1. To study the dynamic behavior of the system, a wide range of frequency sweep over 4 decades ($0.1\,\text{Hz}$ to $900\,\text{Hz}$) is applied. Since the bender voltage (or driving voltage) V is modulated by the pulse width PW, the sine waveform is generated by time-varying the duty cycle percentage. Here, we set the voltage amplitude with a pulse width amplitude $\mathrm{PW} = 200$, corresponding to a duty cycle of 12%. The probe operates at no load.

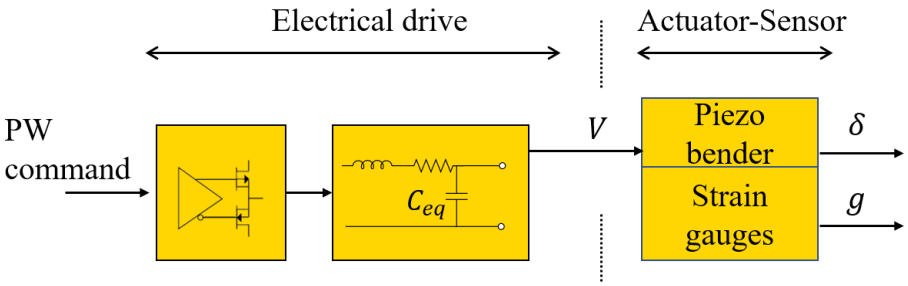

Figure 3.1: Block representation of the subsystems. The piezo bender (represented by the equivalent capacitor C_{eq}) is a part of the low pass filter.

The driving voltage, bender current, and bending strain in response to the pulse width command (PW) are presented in Fig. 3.2a. The bender current is in Volt, and the corresponding current value in Ampere can be calculated from the potential difference (e.g. $\mathrm{UBC} - \mathrm{UBV}$) divided by the damping resistor $R_8 = 560\,\Omega$, referring to the driving circuits in Fig. 2.13a. The global system response is reflected in the bode diagram of bending strain in response to the input PW (see in the right column of Fig. 3.2a). In Fig. 3.2a, the cut-off frequency of driving voltage is about $350\,\text{Hz}$. The responses of the two benders (UB and LB) are the same, in terms of the bender voltages and currents. The measured bending strains of the two benders show slight difference in the gains. Another observation related to the piezo bender drive is that the voltage difference (or the current) becomes significant only with frequencies higher than $70\,\text{Hz}$ (see in left column of Fig. 3.2a).

Our sensing model (2.15) relies on bender voltage supply and bending strain. While the sensing parameters are identified from corresponding signals (displacement, bending strain, and force) against the driving voltage. From the Bode diagram Fig. 3.2b, it can be seen that the gains from driving voltage to bending strain are barely changed when the frequency is lower than $100\,\text{Hz}$. This confirms that our sensing model (2.15) is valid up to $100\,\text{Hz}$. Meanwhile, a mechanical resonant frequency is observed around $400\,\text{Hz}$, concerning the global system (PW-to-bending strain) and the subsystem (bender voltage-to-bending strain).

To refine the identification of dynamic parameters, another frequency sweep between $100\,\text{Hz}$ and $900\,\text{Hz}$ is applied, with more frequency components around $400\,\text{Hz}$. The results from up-chirp and down-chirp are shown in Fig. 3.3. The identified resonant frequency measured from PW to bending strain g is about

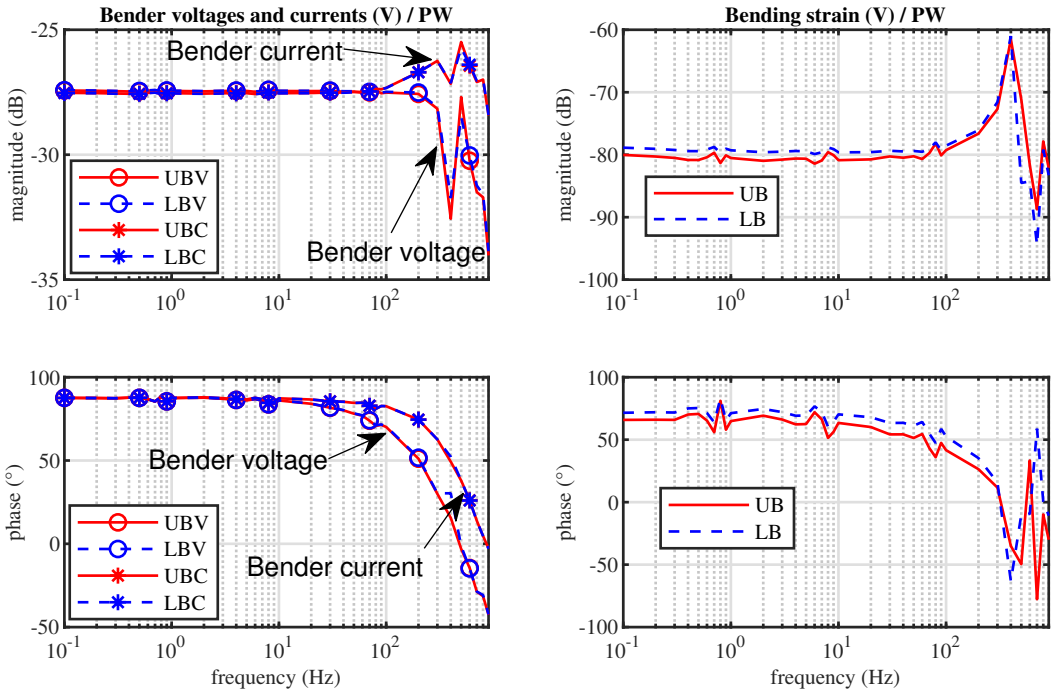

(a)

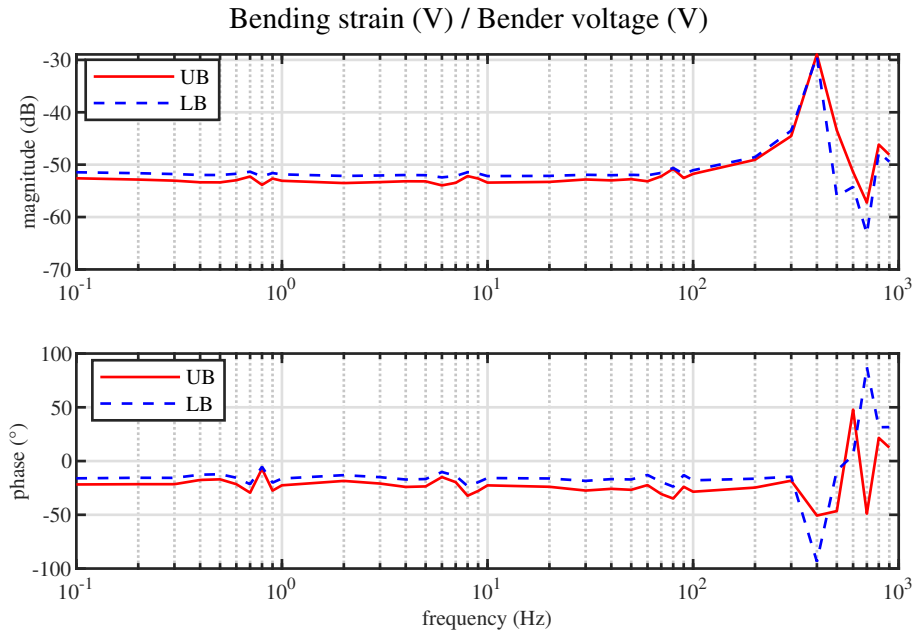

(b)

Figure 3.2: (a) Left column: frequency response measured from input $\mathrm{PW} = 200$ to bender voltage (UBV and LBV) and bender current (UBC and LBC). UB and LB refer to the two piezo benders. Bender current (UBC and LBC) are in Volt, and the current value in Ampere can be calculated from the potential difference (e.g. $\mathrm{UBC} - \mathrm{UBV}$) divided by the damping resistor $R_8 = 560\,\Omega$ in Fig. 2.13a). Right column: frequency response measured from PW to bending strain. (b) Frequency response measured from the driving voltage to the bending strain. The strain signals are measured by strain gauges.

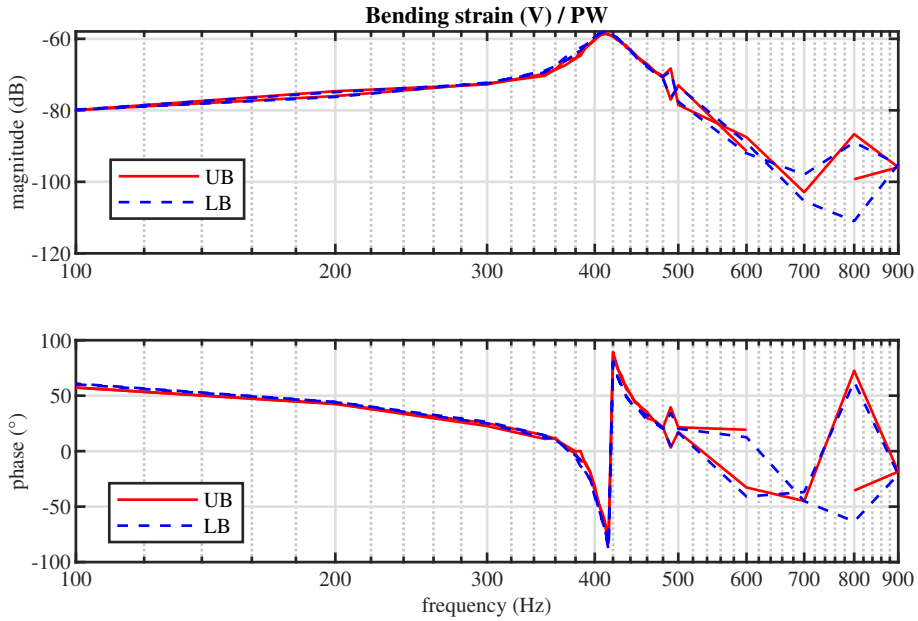

Figure 3.3: Refined frequency response of the bending strain per PW ($\mathrm{PW} = 100$).

410 Hz, with a bandwidth of 45 Hz.

It is marked that the negative magnitudes in the frequency response measured from the input PW to the voltage/current/bending strain (Fig. 3.2a and Fig. 3.3) are due to the fact that the data are normalized by PW for comparison.

It should be noticed that the dynamic response of tip displacement is not directly accessible from the system. So a laser sensor is needed to measure tip displacement. In chapter 2, the response of the subsystem actuator-sensor has been investigated with frequencies up to 200 Hz. A linear relationship exists between the bending strain and tip displacement (Fig. 2.19c, subsection 2.5.2). To go further, the dynamic responses of bending strain and displacement under voltage excitation, with a frequency range of 300 Hz–500 Hz are shown in Fig. 3.4. The tip displacement is still linear to the bending strain, and their dynamic characteristics (resonant frequency and bandwidth) are the same. Hence, we can identify the dynamic system from strain signal directly, instead of measuring the tip displacement.

As a conclusion, the tip displacement is linear to the bending strain over the whole studied frequency range (up to 900 Hz). Concerning the global system, the tip displacement δ and the bending strain g are outputs in response to the input PW. Thanks to the linear relationship between δ and g, the dynamic system identification can be performed with the bending strain, which is directly accessible with the DSP unit. The bending strain in response to PW from Fig. 3.2a and the refined response in Fig. 3.3 will be used for dynamic system identification.

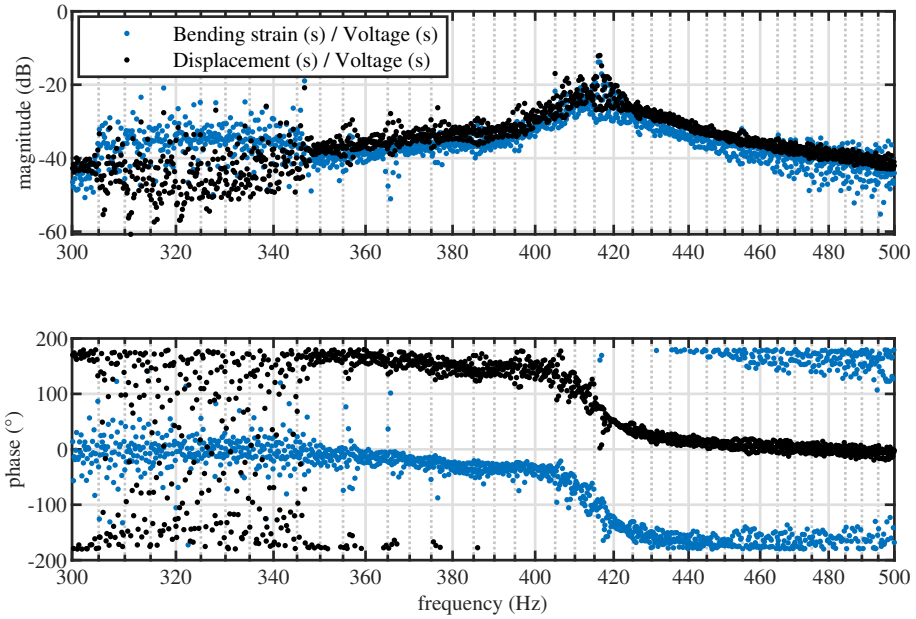

Figure 3.4: Frequency response measured from voltage to bending strain and voltage to displacement ($\mathrm{PW} = 100$), data collected through Picoscope.

3.2.2 Linear dynamic model and identification

Typically, the linear dynamic behavior of piezoelectric bending actuators can be described by a second-order equation as

$$M\ddot{\delta} + D\dot{\delta} + K\delta = NV - f_r \tag{3.1}$$

where M, D, K, and N denote the mass, damping, stiffness, and the force factor of the piezoelectric actuators, respectively. We remind that V and f_r are respectively the bender voltage and the external force. Here, for the dynamic identification, the tests are done at no load condition, $f_r = 0$.

The force factor N is identified in blocking tests, see (2.17). The bender stiffness K is the reciprocal of S_{df} (2.12). The calculation of stiffness K and mass M are as following:

$$K = \frac{1}{S_{\mathrm{df}}} \tag{3.2}$$

$$M = \frac{K}{{\omega_n}^2} \tag{3.3}$$

where ω_n is the resonant angular frequency. From Fig. 3.3, a resonant frequency $\mathrm{Freq}_n = 410\,\mathrm{Hz}$ is obtained. The bandwidth $45\,\mathrm{Hz}$ is determined from the frequency range corresponding to $-3\,\mathrm{dB}$ from the resonant magnitude. The damping D is determined by

$$D = 2\xi\omega_n M \tag{3.4}$$

$$\xi = \frac{1}{2Q} \tag{3.5}$$

Table 3.1: Dynamic parameters.

N (N/V)	K (N/m)	M (kg)	D (Ns/m)
-1.177×10^{-2}	2.075×10^{3}	3.130×10^{-4}	8.840×10^{-2}

where ξ denotes the damping ratio, and the quality factor Q is the ratio between the resonant frequency and the bandwidth. The identified dynamic parameters are listed in Table 3.1.

3.3 Hysteresis model for piezoelectric benders

3.3.1 Hysteresis: cause and effects

It is well known that piezoelectric actuators exhibit hysteretic behavior [70], which degrades the positioning accuracy. The cause of hysteresis in piezoelectric materials is "generally attributed to residual misalignment of crystal gains in the poled ceramic", as summarized by Moheimani et al [56]. On a macroscopic level, the hysteresis induces internal energy losses (or power dissipation) during expanding or contracting process. When talking about hysteresis of piezoelectric materials, it is typical to picture the loop between the applied voltage and displacement. Actually, hysteresis also exists between force and displacement, which was experimentally observed in [59].

In our electromechanical system, the hysteresis effects mainly occur when the bender tip is free or under small loads (see section 2.5 and section 2.7, chapter 2). These effects can be uniformly interpreted by the relative large tip displacement, where hysteresis becomes significant. When the bender tip is free, the hysteresis between voltage and displacement is observed to be frequency dependent (at frequencies higher than 100 Hz) and voltage amplitude dependent. The inclination angles of hysteresis loop change with increasing input voltage amplitudes. The amplitude-dependent hysteresis has impacts on the identification of the sensing parameters, since the parameters are determined by linear regression of the curves in free and blocking tests. For this reason, we have emphasized the need to use the same voltage supply for free and blocking tests.

Regarding our sensing model (2.15), it is the force sensing that is mainly compromised by the hysteresis (section 2.7). To improve force sensing, the hysteresis model is introduced in the following parts.

3.3.2 Dynamic modeling of piezoelectric bender with hysteresis

The hysteresis between the displacement and the driving voltage is well described for the piezoelectric materials. Frequently, the hysteresis is modeled and compensated for accurate positioning. Abundant models are available for this purpose, such as Preisach model [71, 72], Prandtl–Ishlinskii model [73, 74], Bouc–Wen model [75, 76, 77, 78], and hybrid model (such as integration of Maxwell-slip model with Gaussian process) [79].

On the other hand, the effects of external force on hysteresis behavior are barely discussed. In [68], the authors observed that the inclination of voltage-to-displacement curve was decreased when applying an external force. Additionally, our blocking tests (subsubsection 2.5.2.3) show that hysteresis phenomena are minimized when the bender tip is blocked, with a significantly reduced loop size. Thus, the hysteresis behavior of piezoelectric actuator is not only affected by the voltage (electric field) but also by the external force (stress). This was also reported in [70].

The Bouc–Wen model is quite easy to identify, and to inverse compared to other well-known hysteresis models [80]. The Bouc–Wen based hysteresis model for piezoelectric actuators is usually applied with external force ignored. Back to 1995, Low and Guo [75] modeled the hysteresis of a three-layer piezoelectric bimorph beam using the Bouc–Wen model. Even though the external force was presented in the piezoelectric dynamic equation, the hysteretic component was still just related to the voltage excitation. The effects of force on hysteresis behavior was not modeled. Another example, in [76], the Bouc–Wen model was well adapted to describe hysteresis between the output displacement and the input voltage excitation. But as it was for micro/nanopositioning applications, the effect of the load could be ignored. On the contrary, the external force is essential for us to characterize skin properties, along with an accurate displacement measurement. In our case, the hysteresis should be modeled considering the combined effects of voltage (electric field) and external force (stress).

From free and blocking tests, a hypothesis is generated that the hysteresis is related to displacement. The classical Bouc–Wen hysteresis model is applicable in our case. Unlike modeling hysteresis with the excitation voltage [75, 76], we directly model the hysteresis as a function of the instantaneous displacement. Therefore, the linear dynamic equation (3.1) is adapted to (3.6), taking into account the hysteresis.

$$M\ddot{\delta} + D\dot{\delta} + R_T(\delta, z) = NV - f_r \tag{3.6}$$

with

$$R_T(\delta, z) = \alpha K\delta + (1-\alpha)Kz \tag{3.7}$$

$$\dot{z} = A\dot{\delta} - \beta\left|\dot{\delta}\right||z|^{n-1}z - \gamma\dot{\delta}|z|^n . \tag{3.8}$$

R_T is the restoring force, which is composed of an elastic and a hysteretic component. We use f^h to denote this hysteretic force, with $f^h = (1-\alpha)Kz$. In Bouc–Wen hysteresis model, z is an imaginary hysteretic displacement. In (3.7), $0 \leq \alpha \leq 1$ is a weighting parameter [81]. With $\alpha = 1$, hysteretic component disappears and the nonlinear equation (3.6) becomes the linear equation (3.1). In (3.8), A controls the restoring force amplitude. The parameters β and γ control the shape of the hysteresis loop. n controls the smoothness of the transition from elastic to plastic response [75]. For the cantilevered piezoelectric

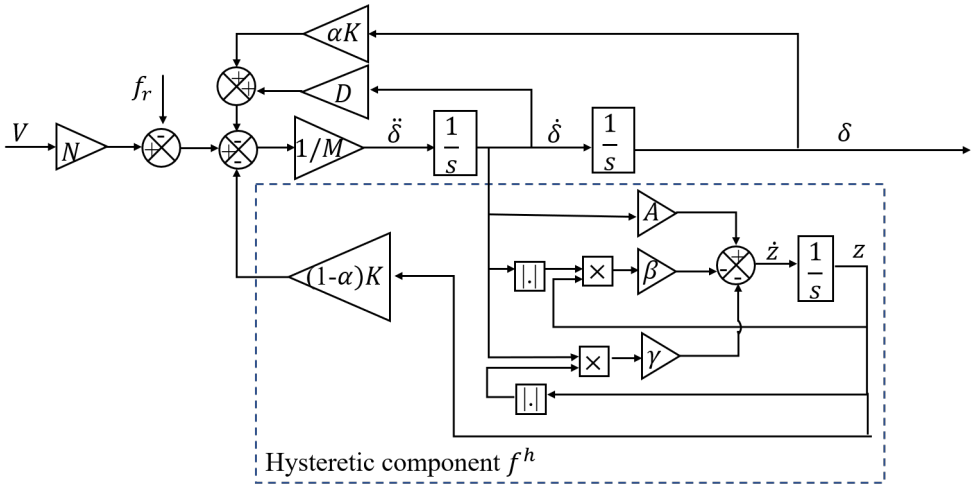

Figure 3.5: Block diagram of the hysteresis model.

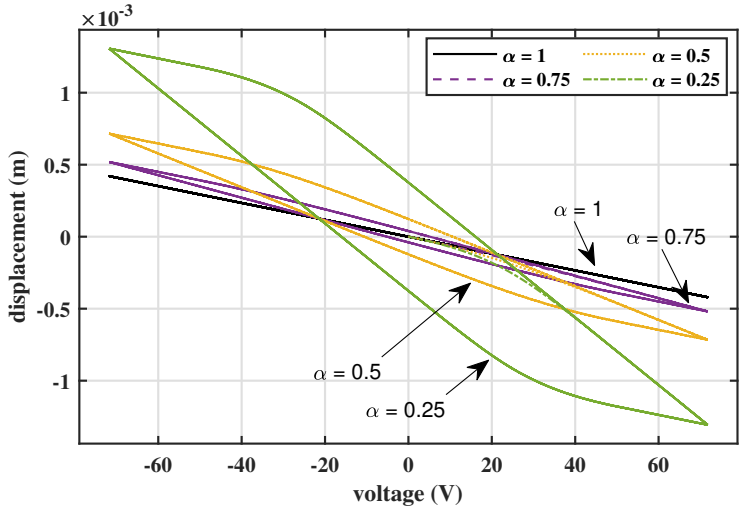

Figure 3.6: Effects of weighting parameter α on hysteresis loop.

bender, $n = 1$ [75], then (3.8) is reduced to

$$\dot{z} = A\dot{\delta} - \beta \left|\dot{\delta}\right| z - \gamma \dot{\delta} \left|z\right|. \tag{3.9}$$

Here, a new relationship is established for piezoelectric actuators between the output δ and inputs voltage and force(V, f_r), with hysteresis considered. The nonlinear dynamic model of the piezoelectric actuator can be easily represented by a block diagram, as shown in Fig. 3.5.

This block diagram was numerically implemented with MATLAB Simulink to study the bender behavior. A was set to 1 to reduce the redundancy of the model [81]. Encouraged by the identification results in [76], we let $\beta = \gamma$. The effects of the weighting parameter α were studied through simulation under no load condition. As shown in Fig. 3.6, when $\alpha = 1$, no hysteresis is presented and the tip displacement is linear to the input voltage. The hysteresis loop size is increased by reducing α. Moreover, the slop is also changing with α.

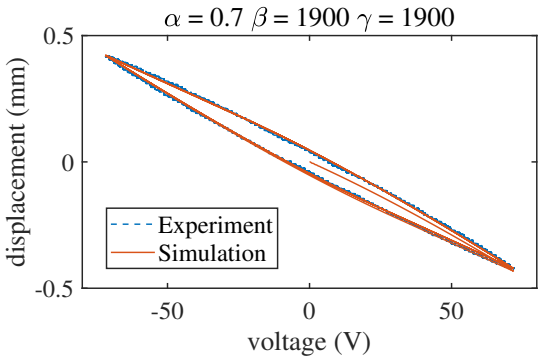

Figure 3.7: Hysteresis model fit. The dash curve shows the experimental data, obtained under a sinusoidal voltage excitation at 1 Hz. The solid curve is the simulation result with the fitted model. Parameters: $A = 1$, $\alpha = 0.7$, $\beta = \gamma = 1900$.

To fit the experimental results, we first determined α to have a similar loop shape and size. Then, we tuned the value of β to match the loop size. The final fitting results are shown Fig. 3.7. In practice, the stiffness K was refined to fit the inclination angle of the experimental curve. The tuned value of stiffness is denoted by K^*. Correspondingly, M and D were recalculated with the tuned K^*, by maintaining an identical resonant frequency. The up tuned stiffness K^*, indicates that the piezoelectric bender is naturally stiffer than the identified value (identified from experiments with equation (3.2)): due to hysteresis effect, the effective stiffness $K = 89\% \times K^*$.

3.3.3 Simulation study on the effects of external force

The effects of the external force f_r on the hysteresis behavior of piezoelectric bending actuators were further investigated by simulation. We scaled the blocking force (NV) by a factor (0, 0.25, 0.5 and 0.75) to introduce the external force. Subject to the same input voltage, the hysteresis size is reduced in Fig. 3.8 with increased force level. This behavior is exactly what we observed from experiments.

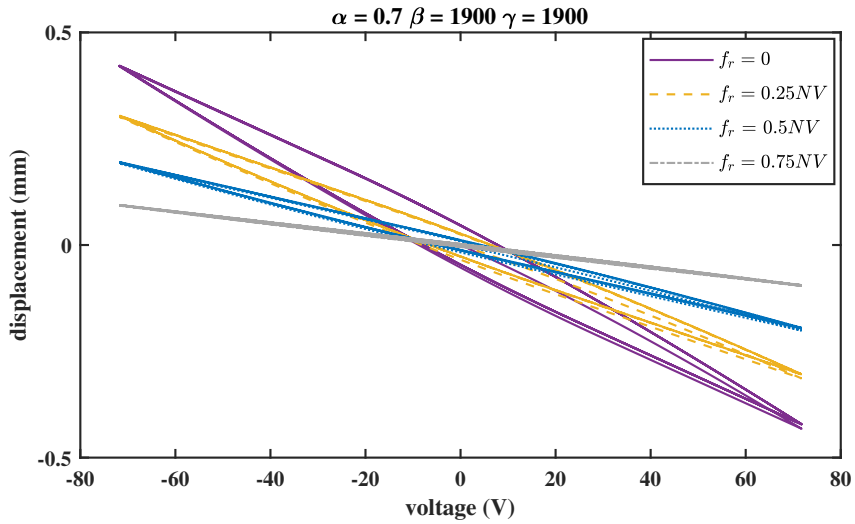

Figure 3.8: Effects of external force f_r on hysteresis behavior (simulation results).

3.3.4 Evaluation of the hysteresis model

The hysteresis model was identified under single input frequency. To assess the robustness of the hysteresis model, experiments were conducted by supplying the piezo bender with voltage harmonics. No external loads were applied. The voltage is composed of a fundamental frequency of $1\,\mathrm{Hz}$, its 3rd and 5th harmonics, with corresponding amplitudes around 20%, 59%, and 59% of full scale, as shown in Fig. 3.9a. To avoid overvoltage, a saturation block is added to limit the output driving voltage to the full scale. The flat parts in voltage source are due to these saturation effects. The predicted displacements with or without hysteresis model are compared with the measured one in Fig. 3.9b. The hysteresis model shows better prediction on tip displacement with a root-mean-square error (RMSE) of $0.0163\,\mathrm{mm}$, while the model without hysteresis has a RMSE of $0.0300\,\mathrm{mm}$. It is validated that the nonlinear dynamic model of the piezoelectric bender identified from single input frequency works well under a multi-harmonic voltage excitation.

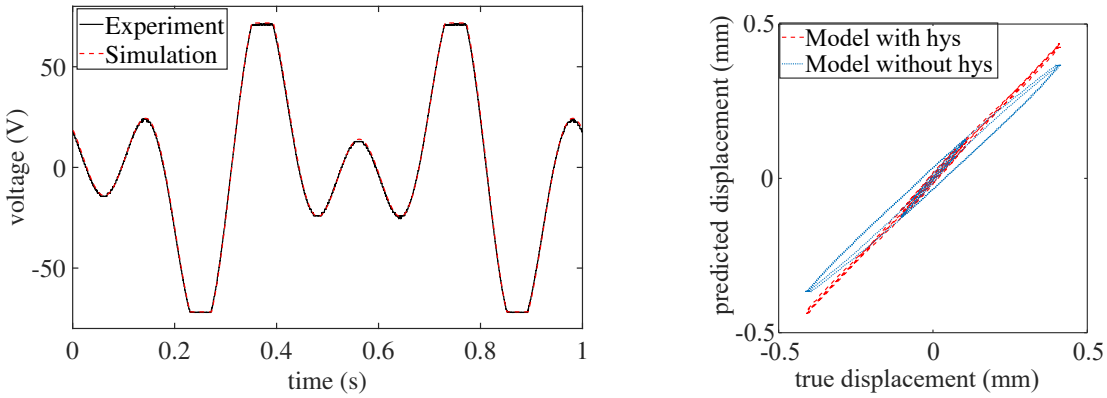

Figure 3.9: Performance of hysteresis model when subjected to multi-harmonic voltages. (a) Voltage source used in experiments (black solid curve) and in simulations (red dash curve). (b) The true displacement was measured by the laser sensor. The red dash curve and the blue dot curve show the prediction results with and without hysteresis modeling, respectively.

3.4 Hysteresis compensation

In the previous section, a Bouc–Wen hysteresis model for piezoelectric actuators has been developed and validated. Based on this model, we propose a first hysteresis compensation strategy to diminish the effects of hysteresis on force sensing. Next, a second hysteresis compensation strategy is proposed, based on displacement control.

3.4.1 Compensation with inverse hysteresis model

The first compensation strategy is based on the dynamic piezoelectric equation including hysteresis effect (3.6). As demonstrated in Fig. 3.5, the hysteresis influence is modeled by introducing a hysteretic force, depending on the instantaneous displacement. The hysteresis compensation can be achieved using the inverse model. Then, the tip force can be estimated following:

$$\hat{f}_r = NV - (M\ddot{\delta} + D\dot{\delta} + R_T(\delta, z)). \tag{3.10}$$

Usually, the compensation of hysteresis in piezoelectric actuators refers to compensating the hysteresis from input voltage to output displacement. While in our case, the compensation means to compensate the hysteretic force, taking the displacement as the input instead of voltage. The compensation strategy with inverse hysteresis model is illustrated in Fig. 3.10. This compensation process is performed virtually with MATLAB® and Simulink®, which requires knowledge of the voltage and displacement, as well as accurate modeling of the hysteresis. It also involves derivative blocks that require a clean data source, otherwise they tend to introduce high frequency noise at the output.

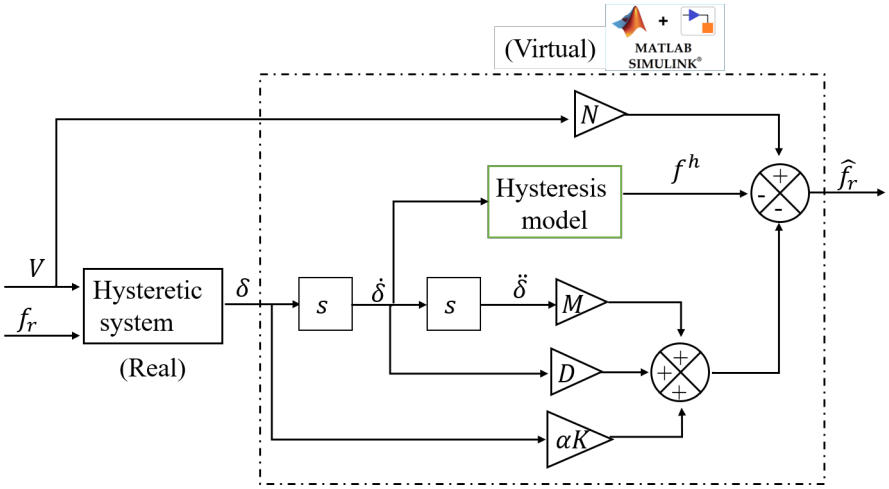

Figure 3.10: Hysteresis compensation with an inverse model. The hysteretic system block represents the real system with hysteresis. The hysteresis model block refers to the modeled hysteretic component in Fig. 3.5.

This inverse model was applied to compensate the hysteretic force presented in free tests (Fig. 2.22). The bender tip force is expected to be null when subjected to voltage excitation only. It can be seen in Fig. 3.11 that the force amplitude and the hysteresis loop size are reduced significantly by compensating hysteresis with (3.10). The maximum hysteresis is attenuated around 71%, compared with estimation results from the linear model (2.15). So we can say here that the force estimation at no load is more accurate when the hysteresis model is used.

Our contribution here is the hysteresis modeling of a piezoelectric bender, including the tip-loaded condition, which is a complement to [76]. To the best of our knowledge, this is the first attempt to model the

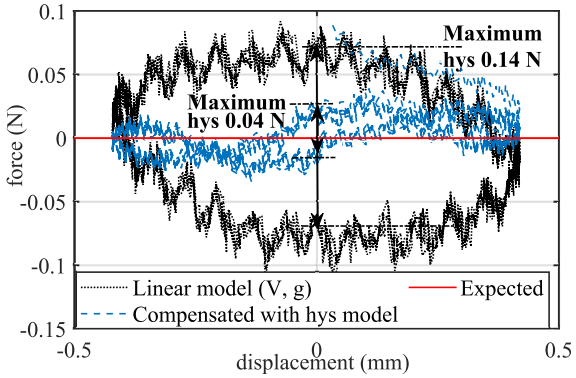

Figure 3.11: Hysteresis compensation using a hysteresis model. The piezoelectric bender was driven by a full-scale sinusoidal voltage at 1 Hz with its tip free. The tip force is expected to be null. The black dot curve is estimated from the linear model (V, g), following equation (2.15). The blue dash curve shows the compensation results with the hysteresis model, following equation (3.10).

hysteresis of piezoelectric actuators with the instantaneous tip displacement instead of the driving voltage [75, 76, 77] using the Bouc–Wen model. Other methods can be adopted to identify hysteretic parameters more wisely, such as neural networks [82], nonlinear filter [75, 76], etc.

Despite the accurate results (tip force estimation) obtained with the direct inversion of the hysteresis model, this approach requires a particular identification process and highly depends on the accuracy of the identified parameters. Therefore, a simpler hysteresis compensation strategy based on closed-loop displacement control is developed.

3.4.2 Compensation with closed-loop displacement control

In the actuator-sensor system, as shown before, strain gauges allow an accurate estimation of the tip displacement, whereas the force estimation is less accurate. A better estimation of the force, especially at low values, can be achieved thanks to the hysteresis modeling and the deduced equation (3.10).

The hysteresis effect is modeled as a function of displacement. In this sense, we can have a constant hysteresis under unloaded and loaded conditions for the same instantaneous tip displacement. To maintain the same displacement for tip-free and tip-loaded conditions, the driving voltage must be adapted. For instance, it increases for the loaded case (3.12), compared to the free case (3.11)

$$NV_{\text{free}} = M\ddot{\delta} + D\dot{\delta} + R_T(\delta, z) \tag{3.11}$$

$$NV_{\text{loaded}} = M\ddot{\delta} + D\dot{\delta} + R_T(\delta, z) + f_r \tag{3.12}$$

where V_{loaded} and V_{free} correspond to the driving voltages needed to achieve the same displacement when the bender tip is loaded and free, respectively.

Thus, the external force f_r can be determined offline from the voltage difference as

$$\hat{f}_r = N(V_{\text{loaded}} - V_{\text{free}}). \tag{3.13}$$

Hence, the hysteresis effect on the force estimation can be eliminated by an accurate displacement control. Following this motivation, the next section focuses on the design of the closed-loop displacement control.

3.5 Closed-loop displacement control

In this section, the closed-loop displacement controller is designed. The performance of the controller is evaluated from the following aspects:

- steady state error
- response time of the closed-loop system

First, the step response of the controlled system is studied under tip-free and tip-loaded conditions. Then, the performance of the controller is further evaluated to track a sinusoidal displacement reference when a spring load is applied to the bender tips (displacement control with a sinusoidal reference is presented separately in the next section 3.6). Note that for sinusoidal references, phase lag may present when using a proportional-integral (PI) controller. Since we are focusing on the vibration amplitude, this issue is not important to a certain extent.

3.5.1 Controller design

In controller design process, the piezoelectric bender was modeled by a first-order system (considering damping and spring effects), as the probe works in quasi-static conditions with an operating frequency below $10\,\text{Hz}$. A PI control method was used to regulate the driving voltage so that the displacement of the bender tip can follow the given reference. Fig. 3.12 shows the control scheme. For the sake of safety, a saturation block is added to limit the output of the controller, i.e., the driving voltage. Thanks to the accurate displacement sensing, $\hat{\delta}$ estimated from (V, g) (2.15) is fed back for displacement control. In this way, we meet the requirement of a stand-alone system.

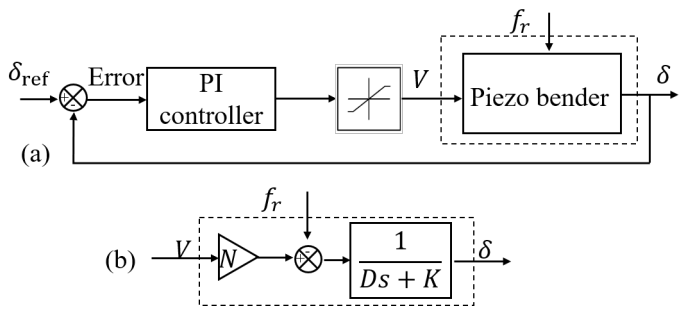

Figure 3.12: (a) Control scheme. (b) Simplified piezoelectric bender model for controller design.

Table 3.2: Parameters related to controller design.

N (N/V)	K (N/m)	D (Ns/m)	K_P	K_I
-1.177×10^{-2}	2.075×10^{3}	8.840×10^{-2}	-5.633×10^{2}	-1.3221×10^{7}

Considering f_r as a disturbance, the transfer function of the approximated system can be written as:

$$\frac{\delta(s)}{V(s)} = N\frac{1}{Ds+K} = \frac{N}{K}\left(\frac{1}{\frac{D}{K}s+1}\right) = G\frac{1}{\tau s+1}, \tag{3.14}$$

where gain $G = \frac{N}{K}$, time constant $\tau = \frac{D}{K}$.

The transfer function of PI controller is described by

$$C(s) = K_P + \frac{K_I}{s}, \tag{3.15}$$

where K_P is the proportionality constant and K_I is the integral constant.

Then, the open-loop transfer function in Fig. 3.12 is expressed as

$$\mathrm{OLTF}(s) = \left(K_P + \frac{K_I}{s}\right) G\frac{1}{\tau s+1} = \frac{GK_I}{s}\frac{1+\frac{K_P}{K_I}s}{\tau s+1} \tag{3.16}$$

A dominant pole compensation method is adopted to tune the parameters of the PI controller. Let

$$\frac{K_P}{K_I} = \tau, \tag{3.17}$$

equation (3.16) is rewritten as

$$\mathrm{OLTF}(s) = \frac{GK_I}{s}. \tag{3.18}$$

In closed-loop control, K_I is adjusted to obtain the required response time t_r, leading to

$$K_I = \frac{3}{Gt_r}. \tag{3.19}$$

Then, K_P is determined from (3.17). Details can be seen on pages 33–35 in [83].

3.5.2 Step response

Here, we set the response time $t_r = 40\,\mathrm{ms}$ for stability purposes. With identified N, K, and D (refer to Table 3.1), the controller parameters K_P and K_I are determined from (3.17) and (3.19). The parameters related to controller design are listed in Table 3.2.

The step responses of the closed-loop system with tip free and loaded are presented in Fig. 3.13. The load applied to the bender tips is a spring. For both cases (free and loaded), the system is stable with zero static error. When the bender tip is free, the response time is exactly as designed, while the response time

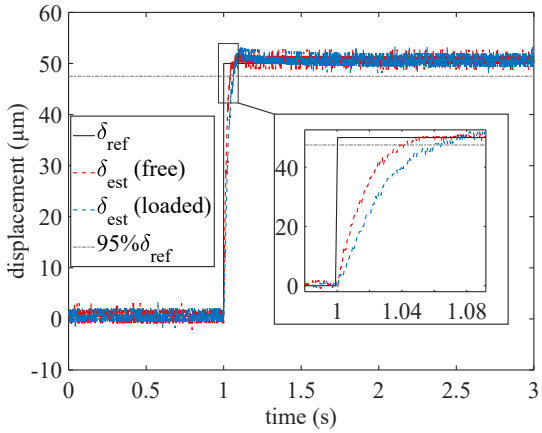

Figure 3.13: Closed-loop step response of the system when the bender tip is free and loaded, respectively. Response time $t_r = 40$ ms.

is delayed to 60 ms when the bender tip is loaded.

3.6 System evaluation: estimator and controller

The working principle of the actuator-sensor system is summarized in Fig. 3.14. The main function of the probe is to estimate the tip displacement and the external force, which is represented by the estimator developed in chapter 2. In the present chapter, closed-loop displacement control is realized. Accordingly, the accuracy of force sensing can be improved within displacement control framework. The objective of this section is to evaluate the whole system including the performance of the estimator and the controller, by applying a spring load. The spring load was made in the lab from PCB materials. Calibration of the PCB spring is explained in Appendix E.

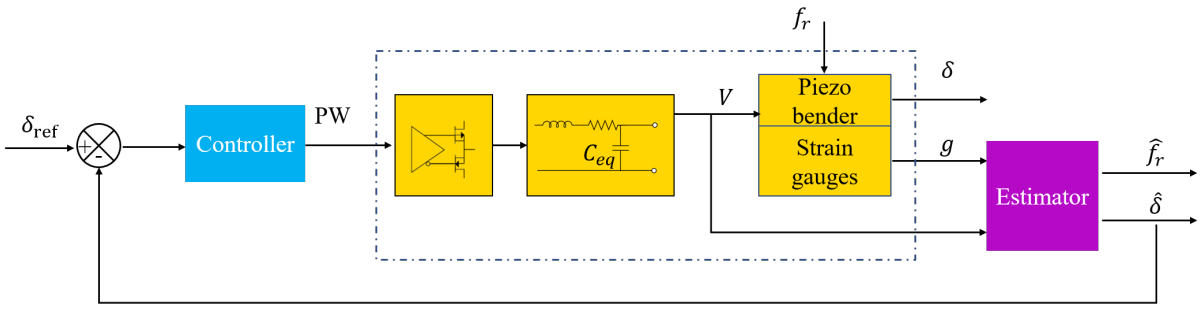

Figure 3.14: Working principle of the stand-alone system. $\widehat{\delta}$ is given by the linear model (2.15) and $\hat{f}_r$ obtained from voltage difference in (3.13).

3.6.1 Experimental setup

The setup for system evaluation is depicted in Fig. 3.15.The bender tips were continuously loaded by a customized spring. Concerning the characterization of skin viscoelasticity, it is typical to perform dynamic mechanical analysis, where sinusoidal stimulation is applied. Hence, our controller should also work

properly when the reference is sinusoid. The primary evaluation criteria of the controller is the vibration amplitude in steady state. A sinusoidal displacement with an amplitude $0.08\,\mathrm{mm}$, at $1\,\mathrm{Hz}$ was used as the reference signal δ_{ref} in the experiment. The real displacement δ_{mea} was measured by the laser displacement sensor. As summarized in Fig. 3.14, the estimated tip displacement δ_{est} was taken as the feed back signal and compared with the reference δ_{ref}. The error between δ_{est} and δ_{ref} was sent to the controller. Accordingly, the driving voltage was regulated.

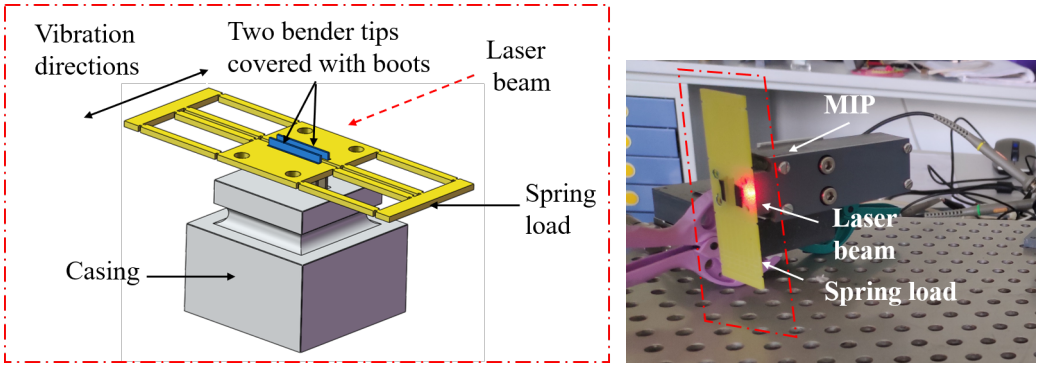

(a) (b)

Figure 3.15: (a) Schematic diagram of system function evaluation with a spring load. The two bender tips fit into two rectangular holes of the customized spring and protrude slightly. The laser beam is targeted on the edge of the spring. (b) Photo of the experimental setup with a spring loaded at the bender tips.

3.6.2 Results

The results of displacement sensing and control are shown in Fig. 3.16. The measured and estimated displacements are in phase. However, they are delayed relative to the displacement reference due to PI control. In our application, we are not bothered by the delayed displacement, as long as the vibration amplitude is guaranteed. The accuracy of the displacement estimation and control is evaluated by the relative peak-to-peak errors. The estimation error ($\left|{}^{(\delta_{\mathrm{pp\_est}}-\delta_{\mathrm{pp\_mea}})}/_{\delta_{\mathrm{pp\_mea}}}\right| \times 100\%$) and control error ($\left|{}^{(\delta_{\mathrm{pp\_mea}}-\delta_{\mathrm{pp\_ref}})}/_{\delta_{\mathrm{pp\_ref}}}\right| \times 100\%$) are 8.7% and 5.5%, respectively. The results on displacement estimation and control are summarized in Table 3.3.

Previously, we have evaluated the performance of the estimator in open-loop condition subsection 2.7.2. The displacement estimation error 5.3% was calculated from the maximum variation between δ_{mea} and δ_{est} and normalized by the full-scale displacement range. Here, the error is evaluated in terms of peak-to-peak values. In this sense, the estimation error in open-loop condition is 3.7% (Table 3.3). In comparison with the peak-to-peak displacement error in open-loop tests (3.7%), the increased peak-to-peak error in closed-loop operation (8.7%) is mainly due to changes in the experimental setups, such as the different targeting points of the laser beam. The control error depends on the performance of PI controller and the estimator (Fig. 3.14). Finally, the control error is lower than the estimation error, which is due to compensation in errors. In general, the displacement sensing and control show satisfying results.

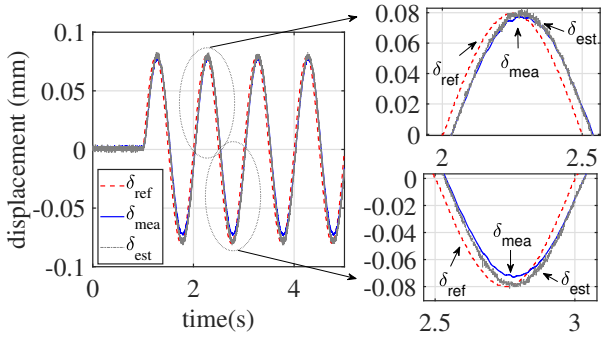

Figure 3.16: Evaluation on displacement sensing and control. The reference displacement is a sine wave with a frequency of 1 Hz, amplitude 0.08 mm. The spring is loaded at the bender tips. δ_{ref}, δ_{mea}, and δ_{est} represent reference displacement, measured displacement, and estimated displacement.

Table 3.3: Displacement estimation and control results.

	$\delta_{\mathrm{pp\_mea}}$ (µm)	$\delta_{\mathrm{pp\_est}}$ (µm)	estimation error	$\delta_{\mathrm{pp\_ref}}$ (µm)	control error
closed-loop (spring load)	151	164	8.6%	160	5.6%
open-loop (hard stop)	618	595	3.7%	/	/

Concerning force sensing, the estimated tip force is expected to be linear to the tip displacement when loaded by a spring. At this point, we present three models of force estimation. The first approach is to calculate the tip force from a linear model (V, g) (2.15). The second approach involves inverse hysteresis model (3.10). As for the last method, we obtain the tip force from the voltage difference between loaded and unloaded conditions with tip displacement controlled (3.13). Tip force estimated from these three methods are compared in Fig. 3.17. The hysteresis loop originating from piezoelectric material is attenuated efficiently after hysteresis compensation. The method with closed-loop displacement control and the one with hysteresis model both provide a better force estimation than the linear model (V, g) (2.15), as the hysteretic force is compensated and the slopes are closer to the calibrated one.

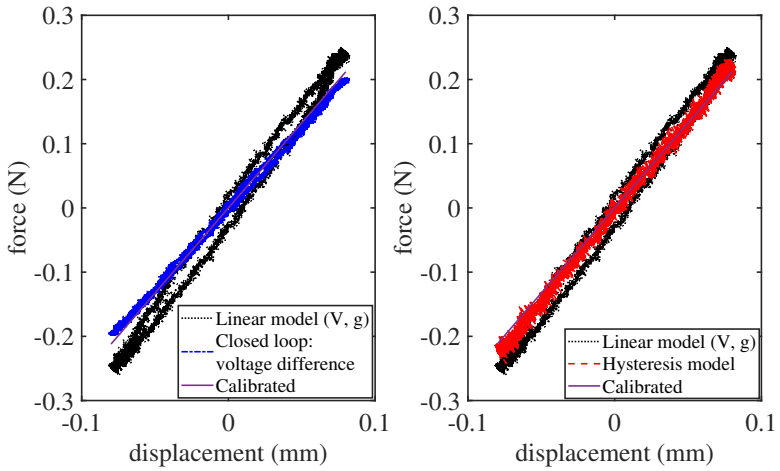

Figure 3.17: Estimated force as a function of estimated displacement with different force sensing approaches. Force estimated from the linear model (V, g) referring to (2.15). Force estimation under closed-loop displacement control referring to (3.13). Force estimation with hysteresis model referring to (3.10). The calibrated force–displacement curve is reproduced from the calibration results of the spring load.

The stiffness of the spring characterized with different methods are compared in Table 3.4. It is noted that the spring stiffness here is determined from linear regression of the force–displacement curves in Fig. 3.17 and divided by a factor of two, assuming the global displacement is twice as large on one side. The stiffness characterized without hysteresis compensation shows largest variation in comparison with the calibrated value. The hysteresis compensation performed under displacement control has significantly reduced such variation from 47.6% to 18.3%. On the one hand, the hysteresis compensation strategy based on closed-loop displacement control shows better characterization results. On the other hand, the variation about 18% is still unpleasant. We can attribute this to several reasons, such as the stiffness was calculated assuming symmetrical behavior of the second bender, errors arising from the calibration process, etc.

Table 3.4: Stiffness of the spring.

Methods	Stiffness ($\mathrm{N/m}$)	Variation ralative to calibrated value
Calibrated (see in Appendix E)	1.060×10^3	0.0%
Linear model (no hysteresis compensation)	1.564×10^3	47.6%
Compensated with hysteresis model	1.407×10^3	32.8%
Compensated with displacement control	1.254×10^3	18.3%

Overall, the bender tips are well controlled to deflect as required. The accuracy of the force estimation can be improved by compensating the hysteretic force based on either an accurate hysteresis model or a closed-loop displacement control framework. The latter approach, which is easier to implement, is used in the following.

3.7 Conclusion

In this chapter, we focused on hysteresis modeling and compensation. To improve the force sensing, we modeled the hysteresis of piezoelectric bender using Bouc–Wen model, and related the hysteresis to the instantaneous displacement instead of the driving voltage. On the one hand, the external force can be directly derived from the inverse hysteresis model by knowing the position trajectory. However, this process requires accurate hysteresis modeling and involves derivative blocks, which tends to introduce high frequency noise at the output. On the other hand, we can more easily compensate hysteresis by controlling the displacement and obtaining the external force from the voltage difference between the tip loaded and unloaded cases under closed-loop displacement control. Hysteresis compensation strategies have been experimentally verified by applying a spring load to the bender tips.

We met the requirements for simultaneous measurement of displacement and force. Closed-loop displacement control was implemented to provide robust, repeatable and comparable measurements. This stand-alone actuator-sensor system allows *in situ* measurements of skin properties. In the next chapter, we will present the experiments on human skin.

Chapter 4

Experiments with human skin

4.1 Introduction

The functions of the MIP have been demonstrated in the previous two chapters, including simultaneous force and displacement sensing, and displacement control as well. In section 2.8 chapter 2, we have justified the discrimination capability of the probe with phantom skins. In this chapter, the application of the MIP on human skin is presented. The skin behavior (forearm) under large harmonic oscillation (strain amplitude up to 16.7%) is first studied. Then, we present how to quantify viscoelastic properties of the skin. The quantified skin parameters include dissipated strain-energy density and the parameters associated with Dynamic Mechanical Analysis (DMA) tests (e.g., dynamic modulus, loss tangent, storage and loss moduli). It is well known that anatomical site is one of the factors affecting the mechanical properties of the skin [84]. The response of the skin at different anatomical sites (forearm and palm) is under investigation. The first study focuses on the characterization of intact skin. Finally, another study is conducted in collaboration with the University of Southampton to study the clinical feasibility of the MIP to detect skin damage caused by mechanical insults. This second study is extended to the lower back site.

4.2 Study 1: Behavior of the intact skin under cyclic loading

Dynamic Mechanical Analysis is a technique typically used to characterize the viscoelasticity of materials. In DMA tests, a sinusoidal strain (stress) is applied and the mechanical stress (strain) response is recorded. With our MIP, we can apply a controlled sinusoidal displacement (strain) and measure the response force (stress) to characterize skin viscoelasticity. In this section, we briefly introduce the quantification process to obtain skin parameters associated with viscoelasticity, such as dissipated-strain energy density and dynamic modulus. Results of skin under tangential cyclic loading are presented. We first consider the *in vivo* skin response (force–displacement and stress–strain curves). Furthermore, a quantification procedure is applied to quantitatively describe the regional variations in the mechanical properties of the skin with

respect to two anatomical sites, forearm and palm.

4.2.1 Apparatus: prototype V1

Tests were run with the designed test bench shown in Fig. 4.1 to study skin response under cyclic loading, with prototype V1. A weighing scale was used to indicate the normal force applied to the skin. A participant's left inner forearm was placed on a transparent supporting plate. The MIP can easily reach the targeted area through an open hole. The skin was immobilized by the open window. During tests, the support plate with forearm on it, was lowered to contact the bender tips by turning the translation stage. The normal force F_n was controlled to 0.5 N. The skin behavior under uniaxial cyclic loading at 1 Hz was studied, with varying displacement amplitudes 100 µm, 200 µm, 300 µm and 400 µm. It is recalled that the MIP works in closed-loop displacement control. The loading patterns used as stimuli are displayed in Fig. 4.2. The skin was held at the initial position for 1 s and then deformed cyclically for another four periods at a given displacement amplitude. We reminder that the displacement amplitude refers to the sum of the displacement amplitudes of the two benders.

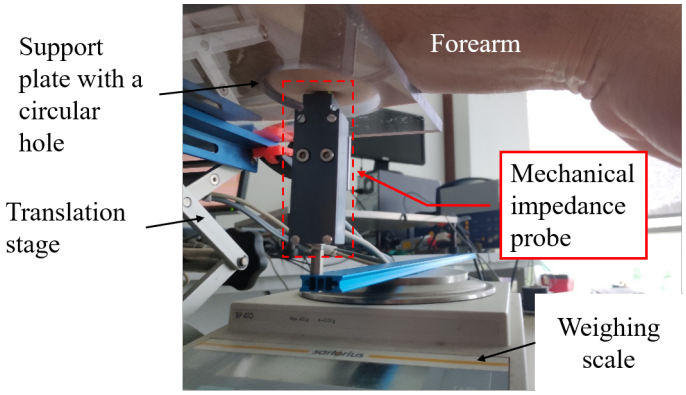

Figure 4.1: Apparatus for *in vivo* tests with prototype V1.

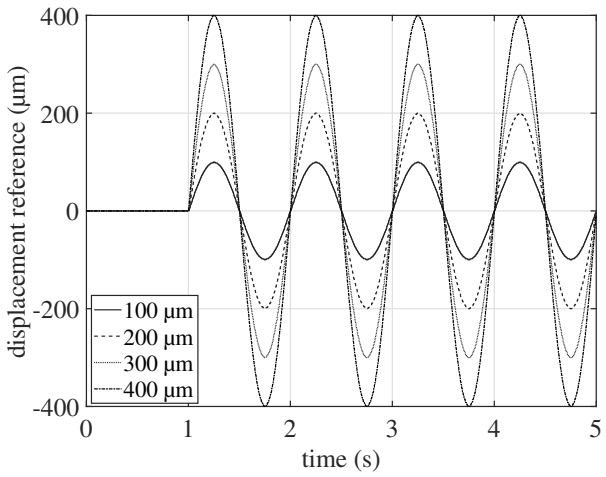

Figure 4.2: Cyclic loading pattern with four displacement amplitudes.

4.2.2 Participants

In this study, a total of 14 participants were recruited locally from the University of Lille. For the forearm skin measurements, we have data from 10 of the participants (4 females and 6 males, average age 35.4). These data sets were mainly used to study the skin behavior under large harmonic oscillation, and to analyze the distribution of skin parameters. Of these 10 participants, 4 also participated in the palm skin tests. We then added 4 additional participants to perform the forearm and palm tests. Thus, for the following forearm and palm skin comparison, we have 8 pairs of data (4 females and 4 males, average age 37).

Informed consent was received from each participant, in line with the requirements of the Ethics Committee of Research at the University of Lille (references: 2020-435-S85).

4.2.3 Procedure

The recruited participants were invited to a testing room on their scheduled time. The testing procedures are summarized as follows:

- clean the testing area with hydroalcoholic gel;
- let the participants accommodate to the testing environment around $5\,\mathrm{min}$ to $10\,\mathrm{min}$ and briefly explain each test we are going to perform;
- perform mechanical tests with MIP.

4.2.4 Data processing

Dynamic modulus is usually used to describe skin viscoelasticity. Additionally, the strain-energy dissipation has also been proposed as a quantitative parameter to describe the hysteresis properties of soft tissue [85]. In the following part, we will explain how to extract these parameters from our measurements.

4.2.4.1 Dissipated strain-energy density

The typical stress–strain curve of soft tissue under uniaxial cyclic loading is shown in Fig. 4.3. The loading and unloading curves are different, as strain energy is dissipated due to the viscosity.

To quantify strain-energy density dissipation, the area of the hysteresis loop (H_A) is calculated as:

$$H_A = \int_0^{\varepsilon_0} \{\sigma_l(\varepsilon) - \sigma_u(\varepsilon)\}\,\mathrm{d}\varepsilon. \tag{4.1}$$

where ε_0 is the turning strain between loading and unloading processes.

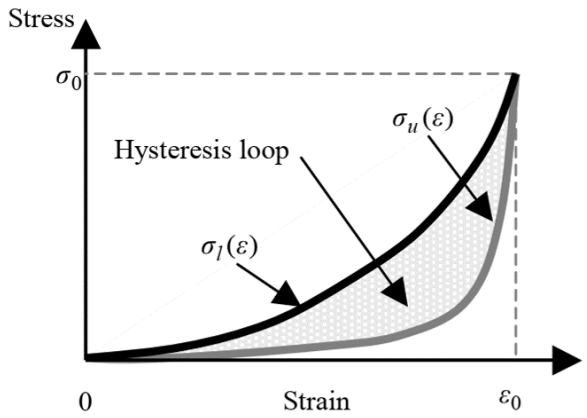

Figure 4.3: The typical uniaxial stress–strain relationships of soft tissue in the loading and unloading processes during a certain time period. $\sigma_l(\varepsilon)$ and $\sigma_u(\varepsilon)$ denote the stress curves during loading (strain increased) and unloading (strain decreased) [85].

4.2.4.2 Dynamic modulus

The strain ε and stress σ in viscoelastic materials when subject to an oscillatory strain, can be expressed as [86]:

$$\varepsilon = \varepsilon_0 \sin(\omega t) \tag{4.2}$$

$$\sigma = \sigma_0 \sin(\omega t + \theta) \tag{4.3}$$

where

$\omega = 2\pi f$, with f the frequency of strain oscillation,

t is the time,

ε_0, σ_0, and θ denote respectively, the strain amplitude, the stress amplitude and the phase lag between stress and strain, as illustrated in Fig. 4.4.

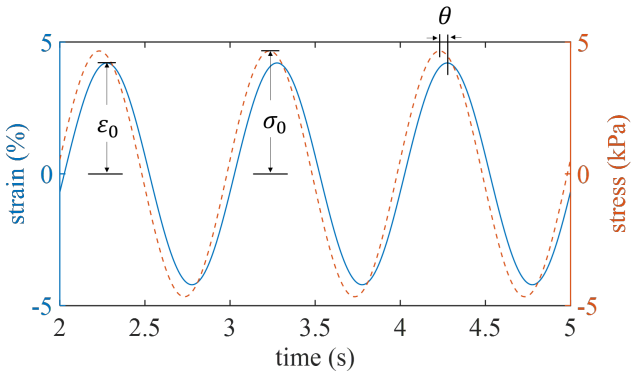

Figure 4.4: Strain and stress of viscoelastic materials.

As the viscoelastic materials show elasticity and viscosity, the storage and loss moduli are used to

describe these two properties. The tensile storage modulus E' and loss modulus E'' are defined as

$$E' = \frac{\sigma_0}{\varepsilon_0} \cos\theta \tag{4.4}$$

$$E'' = \frac{\sigma_0}{\varepsilon_0} \sin\theta \tag{4.5}$$

Storage modulus E' measures the stored energy and represents the elastic portion. While loss modulus E'' measures the energy dissipated as heat, which represents the viscous portion. The dynamic modulus (also complex modulus) E^* is expressed as:

$$E^* = E' + iE'' \tag{4.6}$$

The magnitude of the dynamic modulus $|E^*|$ is given by $\frac{\sigma_0}{\varepsilon_0}$. The ratio between loss and storage modulus gives us another important parameter, loss tangent $\tan\theta$:

$$\tan\theta = \frac{E''}{E'}. \tag{4.7}$$

A pure elastic material has a $\tan\theta$ equal to 0. When the $\tan\theta$ is greater than 1, the viscous property becomes dominant.

The MIP measures the displacement and force. To compare our results with literature, the force was converted to stress with a cross-sectional area that is determined from the product of the boot width (10 mm) and the initial skin thickness (e.g. average 1.39 mm for forearm skin [19]). The thickness of skin we used to calculate the stress is listed in Table 4.1. Meanwhile, the strain was obtained from the ratio of skin displacement to the initial distance between the two boots (2.4 mm), as explained in subsection 1.3.1 (1.2). Fig. 4.5 displays the evolution of skin strain and stress under a vibration amplitude of 100 µm at 1 Hz, measured from the inner forearm of one participant as an example. It can be seen that the strain is sinusoidal thanks to the displacement control. While, the stress curve is not linear and shows DC bias and harmonics. To quantify the viscoelasticity (e.g., identify the magnitude of dynamic modulus $|E^*|$ and phase angle θ), fast Fourier transform (FFT) and inverse FFT were applied to obtain the fundamental signals shown in Fig. 4.4. The amplitude ratio (magnitude of dynamic modulus $|E^*|$) and phase angle (θ) can be determined in the frequency domain. For simplicity, we also use dynamic modulus to refer to its magnitude $|E^*|$.

4.2.5 Results

4.2.5.1 Skin behavior under cyclic loading

For cyclic loading, the skin was stretched and pinched uniaxially by the bender tips of the MIP at 1 Hz. The measured skin response under cyclic loading for the inner forearm is shown in Fig. 4.6a. To reach a

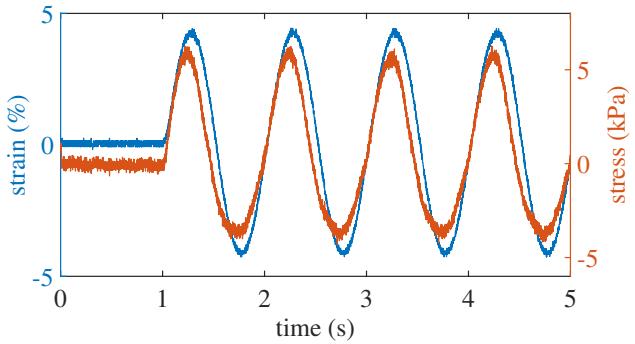

Figure 4.5: Inner forearm stress response under controlled strain amplitude 4.2% (displacement amplitude 100 µm) for one participant.

Table 4.1: Skin thickness used to calculate stress.

Site	Skin thickness (mm)	Reference
Palm	1.5	[87]
Inner forearm	1.39	[19]
Lower back (waist)	2.5	[88]

displacement of about 400 µm, a tangential traction force about 0.35 N is needed. Four loops are formed corresponding to each vibration amplitude. Each loop contains four paths. Paths 1 and 2, corresponding to positive strain, describe load-elongation and relaxation, respectively. Paths 3 and 4, corresponding to negative strain, describe load-contraction and relaxation, respectively. Considering the initial distance between the two boots (2.4 mm), the vibration amplitudes (100 µm, 200 µm, 300 µm and 400 µm) can be converted to strain amplitudes, following equation (1.2), which are 4.2 %, 8.3 %, 12.5 % and 16.7 %. The stress is calculated from the force divided by a cross-sectional area (average skin thickness of inner forearm 1.39 mm [19] times the width of the boots 10 mm), following equation (1.1). The converted stress–strain curves are displayed in Fig. 4.6b–Fig. 4.6e.

Several observations are made according to the four-level cyclic loading in Fig. 4.6:

- The loading paths (paths 1 and 3) differ from the unloading paths (paths 2 and 4), forming the hysteresis loops. They are caused by strain-energy dissipation, representing the viscosity [85]. These hysteresis loops are also related to the phase lag between the strain and stress in Fig. 4.4.
- The four successive cycles are essentially the same in the case of the small strain amplitude, 4.2%, in Fig. 4.6b, compared to other larger strain levels. In Fig. 4.6c–Fig. 4.6e, the skin response becomes repeatable after the first cycle. Therefore, data from the first cycle were not included in the following quantification process.
- Intra-cycle strain stiffening. Considering only load-elongation path (path 1), a hardening phenomenon is presented with an increased strain, especially for strain levels higher than 4.2% (Fig. 4.6c–Fig. 4.6e). This is termed as intra-cycle strain stiffening as in [89].

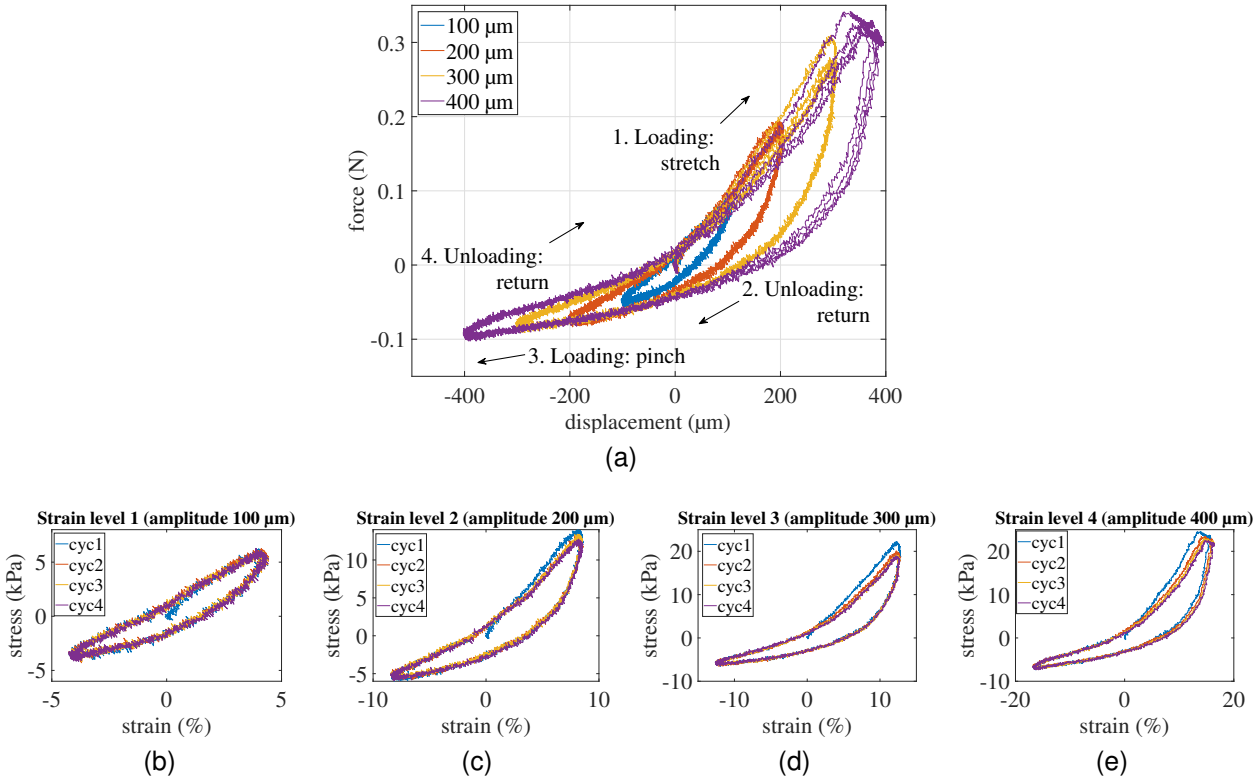

Figure 4.6: Example of inner forearm skin responses under cyclic loading at 1 Hz with four displacement amplitudes. Data from one participant. The skin was loaded cyclically for four periods around the starting point with various vibration amplitudes 100 µm, 200 µm, 300 µm and 400 µm, corresponding to strain levels 4.2 %, 8.3 %, 12.5 % and 16.7 %. (a) Force–displacement curves. Each loop contains four paths. Path 1: the bender tips stretch the skin out. Path 2: return to start point. Path 3: continue to pinch the skin. Path 4: return to start point. (b)–(e) Converted stress–strain curves. cyc1–cyc4 represent the four cycles of loading/unloading. For the highest strain level (16.7 %), a voltage saturation was observed during positive strain.

Table 4.2: Measured force or stress response ($n = 10$) in comparison to literature at forearm site.

	Tests	Strain level	Force (N)	Stress (kPa)
Our measurements	Tangential traction (uniaxial tensile)	16%	0.14–0.33 (0.25 ± 0.06)	10–24 (18.15 ± 4.18)
References			0.3–0.6 [8]	20 [19]

- For larger deformation (curves in Fig. 4.6c–Fig. 4.6e), to reach the same strain level, less force is required when the skin is strained negatively (paths 3 and 4) than strained positively (paths 1 and 2). The unsymmetrical behavior between positive strain and negative strain may result from the nonlinearity of the skin or the boundary conditions between the bender tips and the skin surface.

Our measurements characterized skin viscoelasticity. In Study 1, the skin was stretched across the arm axis, corresponding to the 90°-direction tests in [19]. In the literature, the stress was around 20 kPa under a strain of 16% (refer to Figure 4 in [19]). We obtained a comparable stress level as shown in Fig. 4.6e. The forearm skin responses (force and stress) of the 10 participants under 16% strain are summarized in Table 4.2, considering only the last cycle. Our measurements show that the force and stress levels are in the same order as reported in the literature.

Next, we present the quantification based on the dissipated strain-energy density and dynamic modulus.

Dissipated energy density

To calculate the area of the hysteresis loop H_A for the 4-path loop in Fig. 4.6a, the equation (4.1) is extended to (4.8):

$$H_A = \int_0^{\varepsilon_0} \{\sigma_{l_1}(\varepsilon) - \sigma_{u_2}(\varepsilon)\}\,\mathrm{d}\varepsilon + \left| \int_{-\varepsilon_0}^{0} \{\sigma_{l_3}(\varepsilon) - \sigma_{u_4}(\varepsilon)\}\,\mathrm{d}\varepsilon \right|, \tag{4.8}$$

where σ_{l_1} and σ_{l_3} are the stresses of loading paths 1 and 3, σ_{u_2} and σ_{u_4} are the stresses of the unloading paths 2 and 4. In practice, H_A was calculated from the average area of the last three cycles. Fig. 4.7 shows the dissipated strain-energy density versus peak-to-peak strain. The dissipated strain-energy density increases approximately linearly with the strain range.

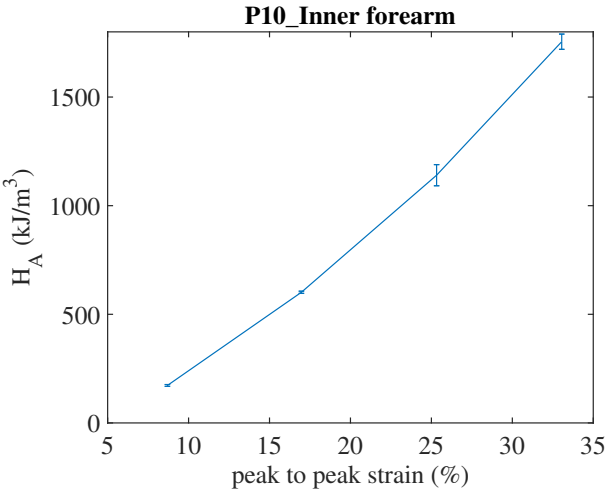

Figure 4.7: Strain-energy density dissipation as a function of peak-to-peak strain (mean $\pm$ standard deviation (SD) of the 3 cycles). Data from one participant.

For the largest strain level (amplitude 16.7%), saturation in the driving voltage was observed in several tests. Thus, we only present the distribution of H_A with the strain amplitude up to 12.5%, i.e., peak-to-peak strain 25%, see in Fig. 4.8. For 10 participants, the mean dissipated energy density also shows strong linear relationships between the dissipated energy density and the strain. The coefficient of variation (CV) (the ratio of the standard deviation to the mean) under each strain level is $18\,\%$, $15\,\%$ and $17\,\%$. The dispersion shows the variations between individuals.

Dynamic modulus

The dynamic modulus was extracted from the skin data measured with the smallest strain amplitude (4.2%), as the skin behaved more linearly under this condition (corresponding to $100\,\mu\mathrm{m}$ vibration amplitude). The fundamental signals (fundamental stress and strain) are obtained applying FFT and inverse FFT. Then, the magnitude of dynamic modulus $|E^*|$ and the phase angle θ are obtained in the frequency domain. Knowing these two parameters, we can further derive other parameters, such as the loss tangent $\tan\theta$, the storage modulus E' (4.4), and loss modulus E'' (4.5). The mean dynamic modulus of forearm is $121\,\mathrm{kPa}$ with strain amplitude of 4.2%, measured from 10 participants (Fig. 4.9a). For the forearm, the storage modulus is

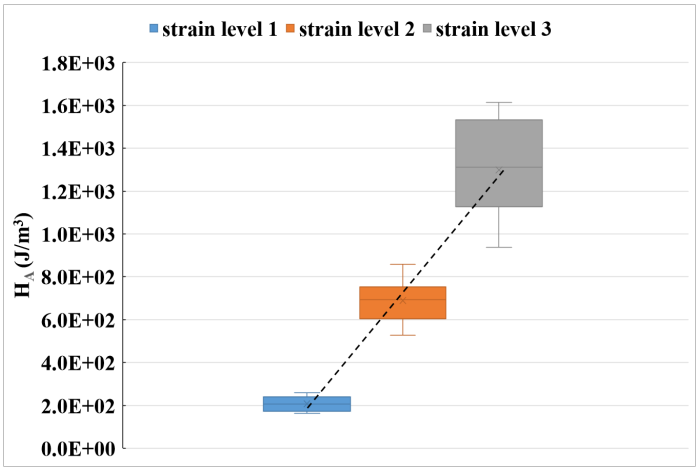

Figure 4.8: Distribution of strain-energy density dissipation (forearm, $n = 10$) under peak-to-peak strain of $8.3\,\%$, $16.7\,\%$ and $25.0\,\%$, labeled as strain levels 1–3, with mean values of $207\,\mathrm{J/m^3}$, $689\,\mathrm{J/m^3}$ and $1300\,\mathrm{J/m^3}$. Cross marks the mean value. The black dash line is the linear regression of the mean values.

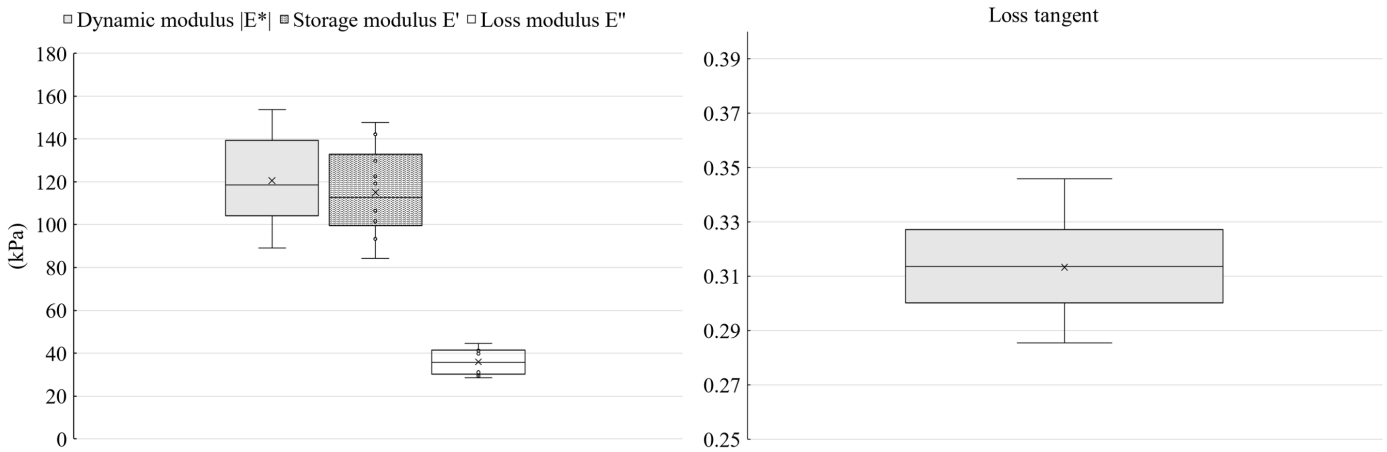

Figure 4.9: Distribution of characterized skin parameters at forearm site ($n = 10$). (a) Dynamic modulus ($\mathrm{mean} = 121\,\mathrm{kPa}$), storage modulus ($\mathrm{mean} = 115\,\mathrm{kPa}$), and loss modulus ($\mathrm{mean} = 36\,\mathrm{kPa}$). (b) Loss tangent ($\mathrm{mean} = 0.31$). Cross marks the mean value.

much higher than the loss modulus. The mean storage modulus is $115\,\mathrm{kPa}$, around three times of the loss modulus $36\,\mathrm{kPa}$. This relationship is reflected in the loss tangent in Fig. 4.9b. The CV of the two moduli is close, about 18% for storage modulus and 17% for loss modulus.

At this level, we demonstrate the capabilities of the MIP for skin characterization, taking inner forearm measurements as an example. To sum up the results with forearm tests ($n = 10$), the characterization of the viscoelastic properties of the skin are demonstrated based on strain-energy density dissipation (hysteresis area enclosed by the loading and unloading stress–strain curves) and dynamic modulus. The latter requires extraction of the fundamental signals. The skin behaves nonlinearly under large oscillation. Nevertheless, the strain-energy density dissipation shows linear relationship with the applied strain range. Dynamic modulus of forearm quantified at a strain amplitude of 4.2%, is $121\,\mathrm{kPa}$ with a loss tangent of 0.31. These results will be compared with the ones measured from the palm site.

4.2.5.2 Forearm skin vs palm skin

The same cyclic tests were conducted with the palm skin to verify the distinction capabilities of the MIP for real human skin. Fig. 4.10 compares the skin force in response to the applied displacement, measured at the palm and the forearm sites for one participant. For this participant, a force about 0.12 N was needed to stretch the skin to 100 µm (strain 4.2%) at the palm site. While the forearm skin required only half of the force, 0.06 N, to reach the same strain level, as shown in Fig. 4.10a. The cyclic loading tests at four strain levels on the same participant show that the palm skin is stiffer than the forearm skin.

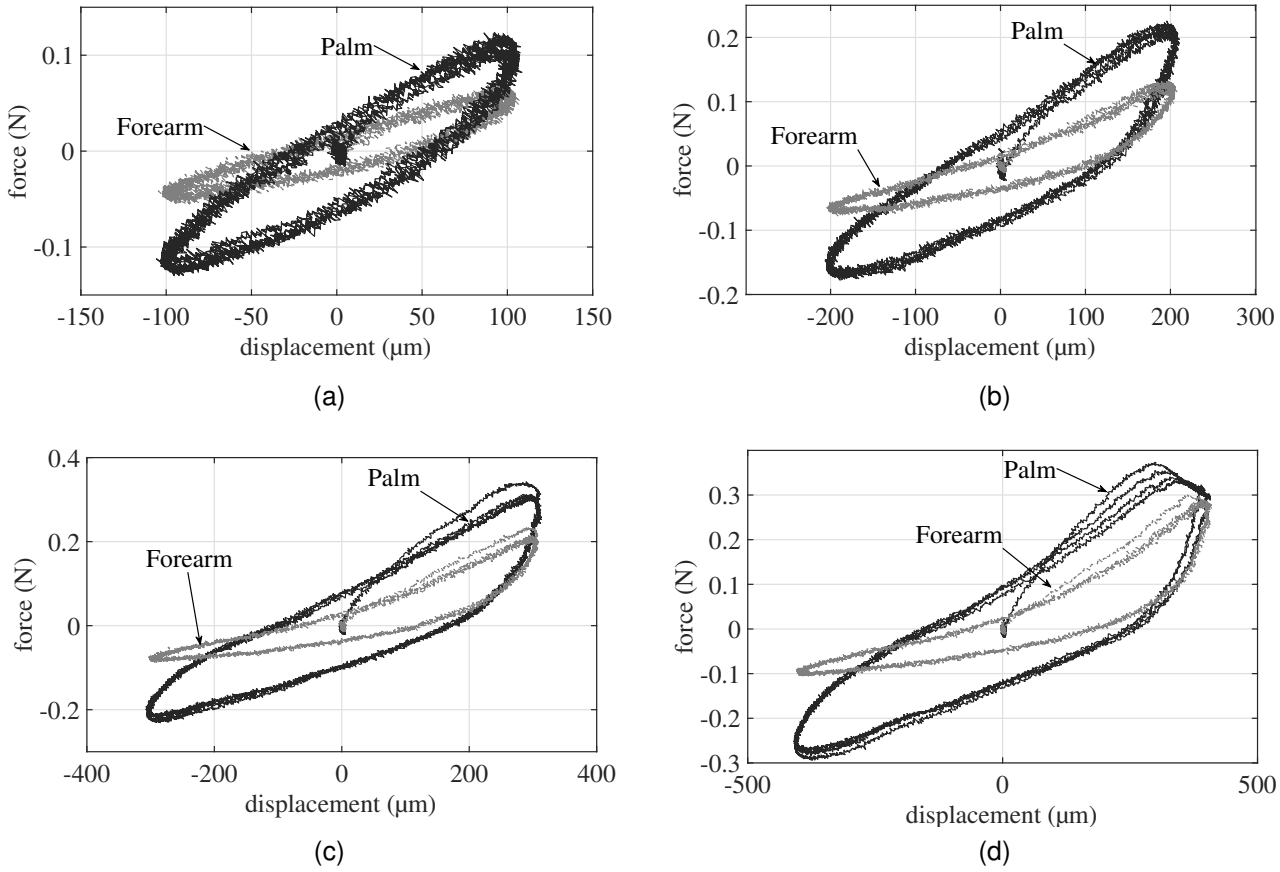

Figure 4.10: Inner forearm skin vs. palm skin, data from one participant. The skin was cyclically stressed for four periods at 1 Hz around the starting point. The vibration amplitude was varied with four levels 100 µm, 200 µm, 300 µm and 400 µm. For the highest displacement level (400 µm), voltage saturation was present.

The mechanical properties of forearm and palm skin were further quantified with a cohort of 8 participants. The skin was cyclically stressed for four periods with a strain amplitude of 4.2%, at 1 Hz. The comparison between the forearm and the palm skin, concerning the dissipated strain-energy density is given in Fig. 4.11. For the statistical analysis (Fig. 4.11b), two participants' palm data were removed (P02 and P08). Indeed, we had issues with these two participants. For participant P02, the peak-to-peak strain of palm was 7.45%, less than the required 8.3%, due to inappropriate setting of the saturation voltage (see Appendix F Fig. F.1). Nevertheless, the dissipated strain-energy density is still much higher than that of the forearm skin even with a smaller strain level (Fig. 4.11a). For participant P08, a suspicious slip was

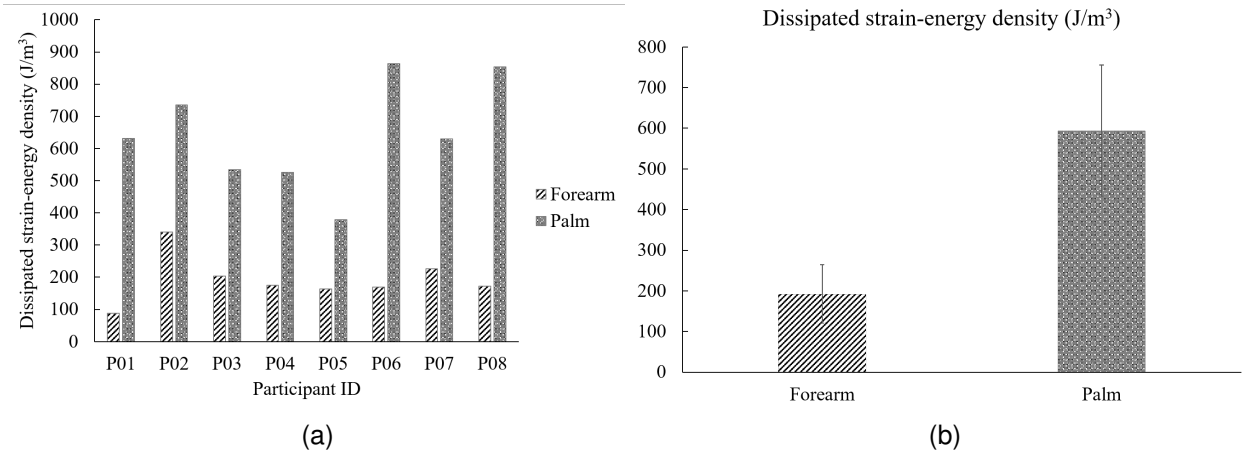

Figure 4.11: Dissipated strain-energy density: forearm skin vs palm skin. (a) Individual results. (b) Forearm ($n = 8$): $\mathrm{mean}\pm\mathrm{SD} = 192\pm72\mathrm{J/m^3}$. Palm (P02 and P08 data removed, $n = 6$): $\mathrm{mean}\pm\mathrm{SD} = 594\pm161\mathrm{J/m^3}$.

present in the stress–strain curve measured at the palm site (see Appendix F Fig. F.2), which may bias the results. Thus, for the statistic analysis, the palm data of P02 and P08 were removed. The mean value of the 8 forearm skins and 6 palm skins are presented in Fig. 4.11b. The mean dissipated strain-energy density in palm skin is $594\,\mathrm{J/m^3}$, about 3 times higher than in the forearm skin ($192\,\mathrm{J/m^3}$). As a general conclusion, the palm skin has more energy dissipated under cyclic loading than the inner forearm skin.

On the other hand, fundamental signals were extracted to deduce dynamic modulus. As shown in Fig. 4.12, the three moduli ($|E^*|$, E' and E'') are all higher at palm site than at forearm site. The palm skin of the participant P02 shows the highest magnitude of dynamic modulus Fig. 4.12a. This indicates that the palm skin of P02 is much stiffer than the others, which can be the reason why the output voltage was easily saturated in this test. This issue was later fixed by increasing the voltage saturation threshold, but still lower than the nominal voltage of the piezo bender. For the participant P08, the moduli of palm skin are still higher than the forearm, even though slipping is suspected when testing the palm. Concerning loss tangent, palm skin is higher than the forearm skin. This is related to a larger part of viscosity, which is relevant with the higher strain-energy density dissipation.

In statistical analysis, the two outlying data sets (palm skin data of P02 and P08) were once again excluded. The dynamic modulus of the forearm and palm ($\mathrm{mean} \pm \mathrm{SD}$) are compared in Fig. 4.13 The mean dynamic modulus for the forearm ($n = 8$) is $110.97\,\mathrm{kPa}$, and for the palm ($n = 6$) is $206.71\,\mathrm{kPa}$. As for the loss tangent, the average value for the forearm skin is 0.31. It is higher for the palm skin, about 0.55.

The mean value and the CV of all the skin parameters measured at the forearm and palm sites are summarized in Table 4.3. The largest differences between forearm and palm are seen in hysteresis loss (dissipated strain-energy density) and loss modulus. They are about three times higher at the palm site than at the forearm site. Then, the magnitude of the dynamic modulus of the palm is about 1.9 times higher than that of the forearm one, and 1.8 times higher in the loss tangent. The smaller difference is for the storage modulus, which is about 1.7 times higher than that of the forearm.

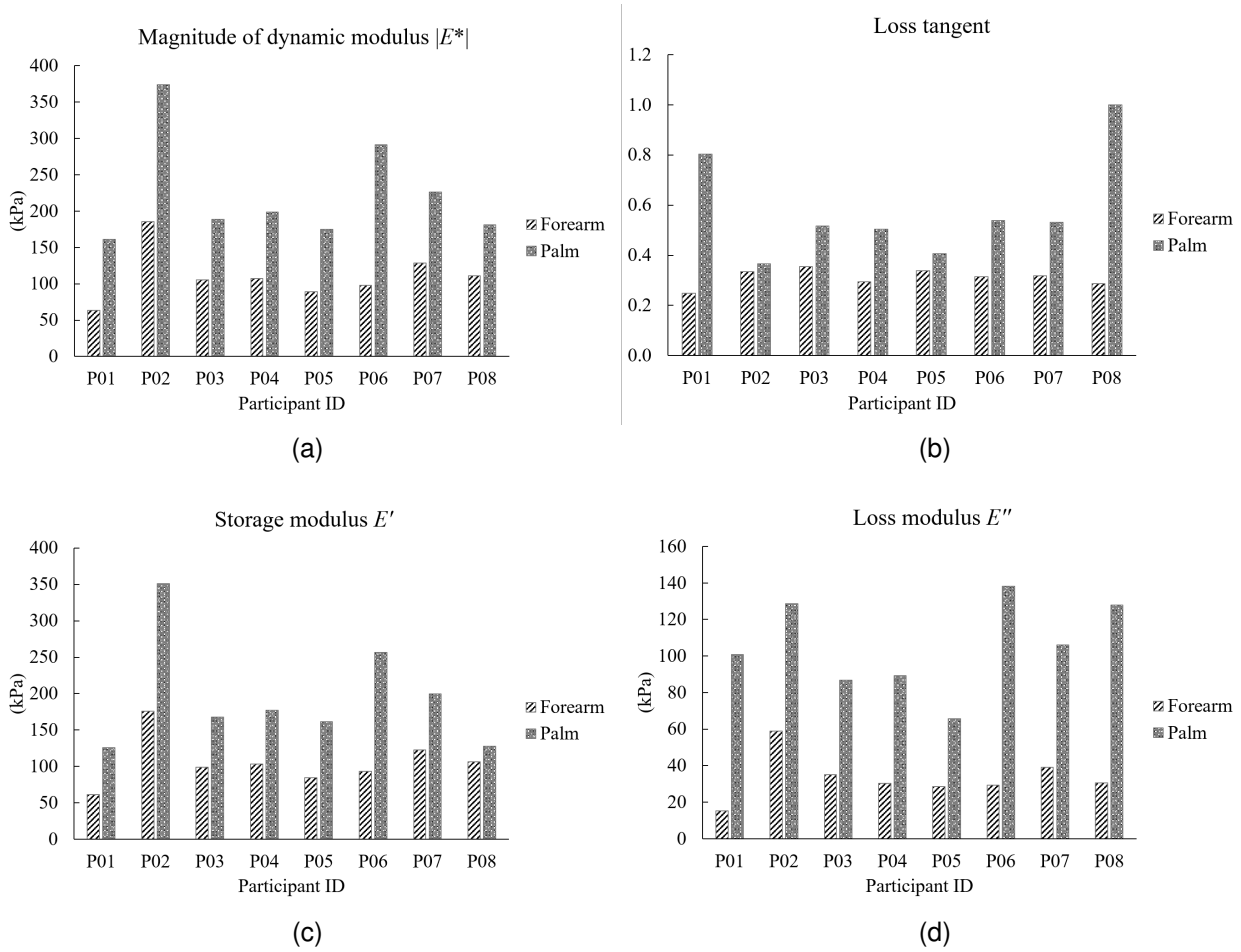

Figure 4.12: Dynamic modulus: forearm skin vs palm skin for each participant.

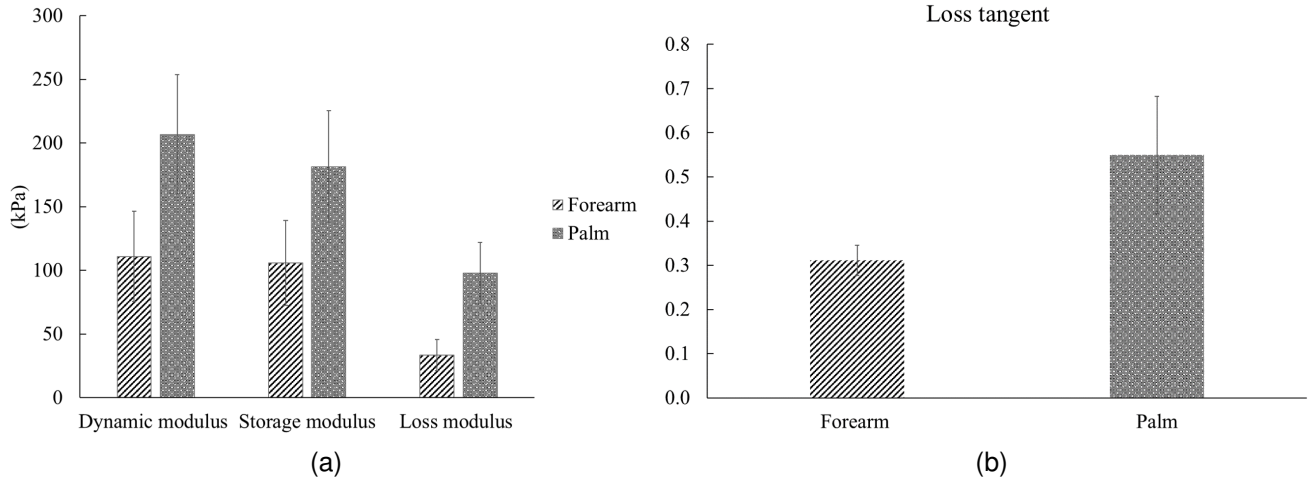

Figure 4.13: Dynamic modulus ($\mathrm{mean} \pm \mathrm{SD}$): forearm ($n = 8$) vs palm ($n = 6$).

Table 4.3: Mean and coefficient of variation of skin mechanical parameters at forearm and palm sites.

	Dissipated strain-energy density		Dynamic modulus $\lvert E^* \rvert$		Loss tangent $\tan\theta$		Storage modulus E'		Loss modulus E''	
	Mean (J/m^3)	CV (%)	Mean (kPa)	CV (%)	Mean	CV (%)	Mean (kPa)	CV (%)	Mean (kPa)	CV (%)
Forearm ($n = 8$)	192.34	37	110.97	32	0.31	11	105.79	32	33.37	37
Palm ($n = 6$)	594.21	27	206.71	23	0.55	24	181.38	24	97.82	25

Considering the skin structure, the differences in stiffness (modulus) may be due to a thicker epidermis layer of the palm (may reach $0.8\,\mathrm{mm}$), whereas the thickness of the most other body sites, except the soles ($1.4\,\mathrm{mm}$), varies from $0.07\,\mathrm{mm}$ to $0.12\,\mathrm{mm}$ [10]. Moreover, a larger hysteresis loop is shown for the palm skin, which is related to a larger influence of viscosity. These differences between palm skin and forearm skin are in line with the plots presented in [8].

In conclusion, measurements with the MIP allow us to derive a series of skin parameters. In this way, we can distinguish between skin at different anatomical sites. Here, we quantified the skin mechanical properties from stress–strain curves and illustrated the anatomical sites related differences based on the dissipated strain-energy density and dynamic modulus. During the measurements, slip issue was observed for some participants in the hand palm tests, especially at large strain amplitude. We can reduce the vibration amplitude to avoid the slipping.

4.3 Study 2: Clinical feasibility

This second study has been performed in collaboration with our colleagues from the University of Southampton. The goal was to verify whether the MIP we developed was accurate enough to highlight mechanical differences from the skins subjected to mechanical insults or not. In other words, we aimed to detect the changes in local skin parameters before and after a mechanical insult (tape stripping and axial loading). The study was designed to assess the reliability and sensitivity of the parameters derived from the developed MIP. The big difference with Study 1, regarding the testing environment, is that Study 2 was performed in clinical conditions close to the real application ones. Therefore, more uncertainties were introduced by the operators or by the participants, such as the normal force level or the MIP orientation.

4.3.1 Apparatus: prototypes V1 and V2

Two versions of the MIP were used in the experiments, as illustrated in Fig. 4.14. As a reminder, the normal force was not monitored with prototype V1. To keep more or less this force constant, the indentation depth was fixed at a constant value of $1\,\mathrm{mm}$, thanks to a customized cap. Prototype version two (V2) has a normal force sensor embodied inside its casing. Thus, the normal force at the bender tips can be monitored

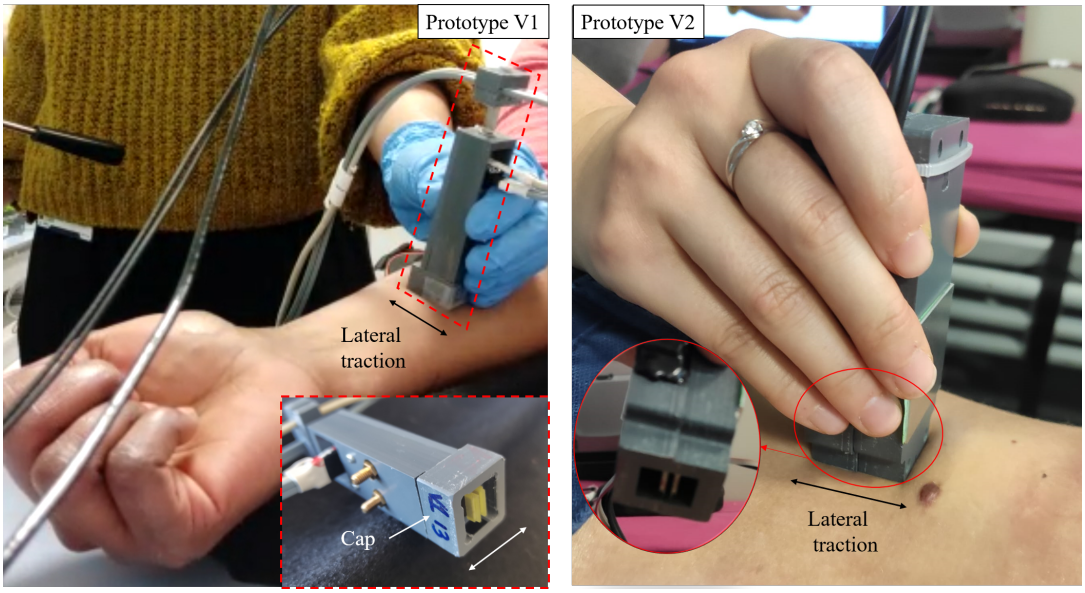

(a) (b)

Figure 4.14: Setup for *in vivo* tests. (a) Example of forearm tests with prototype V1. A customized cap is used to allow 1 mm indentation depth of the bender tips on the skin surface. (b) Example of lower back tests with prototype V2. The indentation depth is adjustable so that the exerted normal force is within the test range.

and regulated to the targeting force level (0.2 N) through a visual feedback from the computer screen. It may be noticed that during this clinical study, mechanical issue arose with V1 because of the unwanted movement of the tested body sites. So we began the measurements with V1 and ended up with V2. Both prototypes, however, are designed to characterize the quasi-static mechanical properties of skin. During the measurements, both probes were placed perpendicular to the testing area of the skin (Fig. 4.14). A specific loading pattern was applied to the skin, as depicted in Fig. 4.15. This step-hold-cyclic loading pattern was adopted from [90]. The pre-strain was necessary to prevent skin slack during the sinusoidal cyclic loading.

To facilitate the data collection process, we designed a graphical user interface using MATLAB® App Designer, as shown in Fig. 4.16.

4.3.2 Participants

The approach involved an observational case-control studies, recruiting healthy participants from the local population at University of Southampton. It was conducted in an environmentally controlled laboratory, with ethical approval from the host institution (University of Southampton), reference number 9349.A6. Informed consent was received from each participant.

Details of the participants involved in the dynamic mechanical analysis with MIP are summarized in Table 4.4, indicating which of the probes was used to measure skin properties at the two anatomical sites. Forearm characteristics were evaluated in 8 subjects aged ranging from 27 to 41 (mean age 34 years, 3

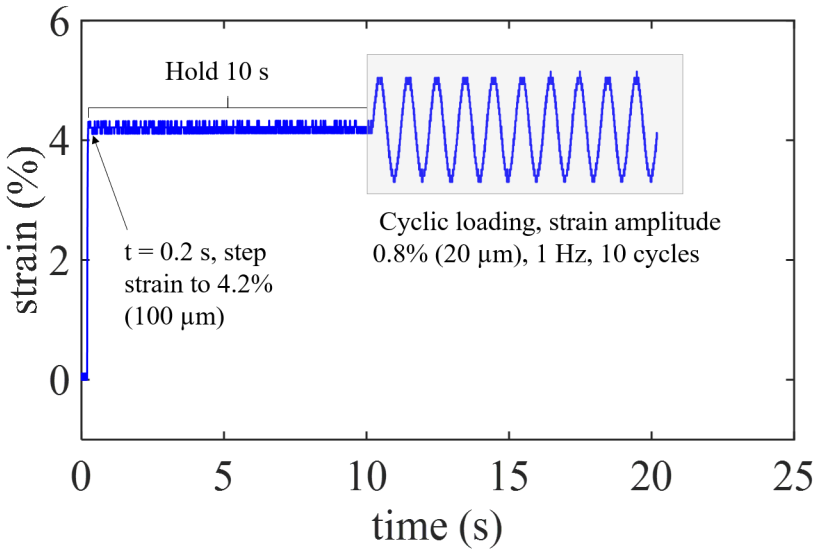

Figure 4.15: Loading pattern of the skin for dynamic mechanical analysis. The skin was stretched to 4.2% at $t = 0.2\,\mathrm{s}$, then the strain was held for $10\,\mathrm{s}$, followed by a sinusoidal cyclic load at $1\,\mathrm{Hz}$, with a strain amplitude of 0.8%.

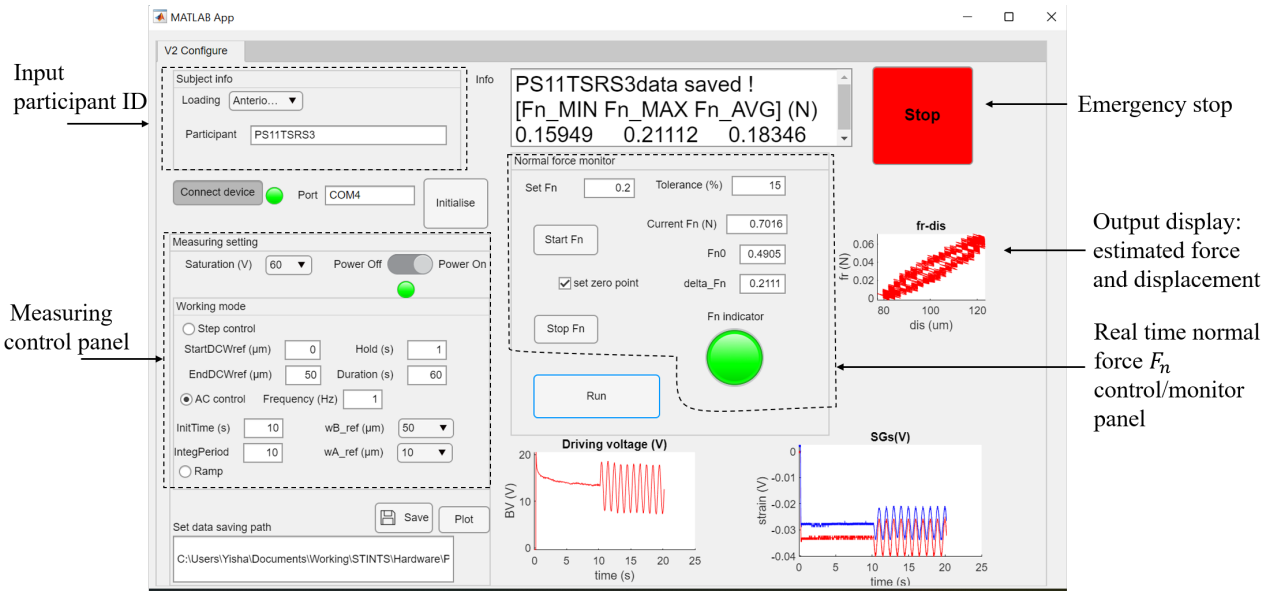

Figure 4.16: Graphical user interface designed for the MIP.

males and 5 females). For the lower back, 4 participants were tested with an age range of 27 to 41 (mean age 31 year, 2 males and 2 females).

4.3.3 Protocols

The participants were invited to the testing room. Two body sites, forearm and lower back were measured. The forearm has three randomized testing sites, including the control site, the tape stripping site, and the intermittent loading site. The lower back has four randomized testing sites, with an additional continuous loading site. Fig. 4.17 shows the testing protocol. The treatments to each testing site are described as below:

Table 4.4: Participants information and the used probe version.

Participant ID	Gender	Age	Forearm	Lower back
PS01	M	37	V1	/
PS02	F	30	V1	/
PS03	F	40	V1	/
PS04	F	29	V1	V2
PS05	F	33	V1	/
PS06	M	36	V2	/
PS07	M	27	/	V2
PS08	M	41	V2	V2
PS09	F	27	V2	V2

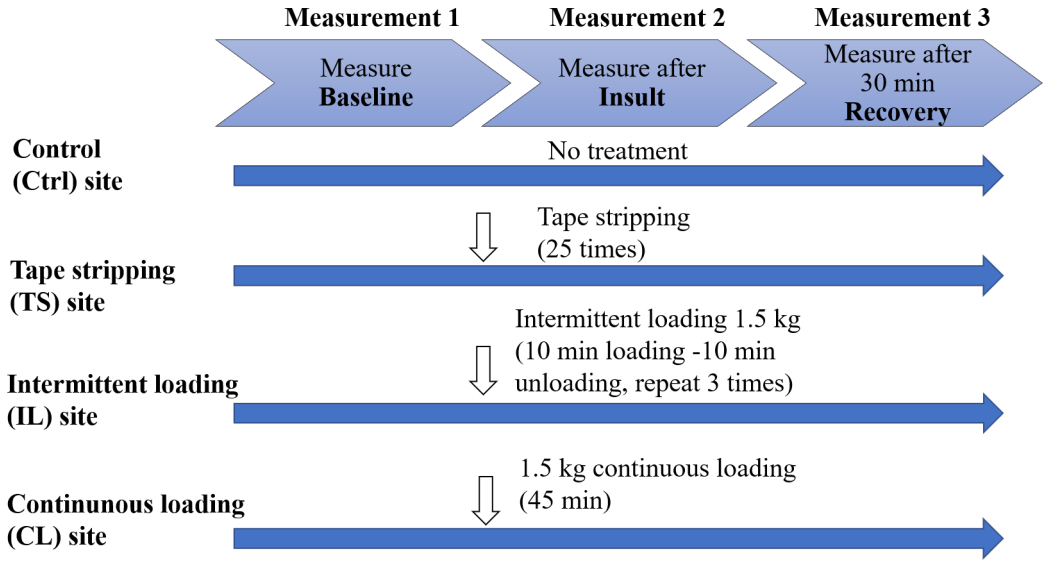

Figure 4.17: Testing protocol for the skin insult study. Total duration is about 150 min.

Control site (Ctrl) No treatment.

Tape stripping site (TS) Tape stripping 25 times with Sellotape. The total duration takes approximately 5 min. For each tape stripping, we press the tape on the skin and strip it rapidly.

Intermittend loading site (IL) 1.5 kg of intermittent loading with 3 cycles of load/unload for 10 min each, totally taking 1 h.

Continuous loading site (CL) 1.5 kg continuous loading for 45 min, only for the lower back.

The whole study has three measuring sessions, denoted by "BL" for baseline, "I" for after insult and "R" for after recovery. First, the baseline measurements are taken before applying any insult. Second, the measurements are taken after insults, control site included. Last, the measurements are taken after 30 min of recovery, control site included. Note that the duration of each insult is different. We first applied intermittent loading, then continuous loading (for the lower back only), and finally tape stripping, so that all the insults could be completed at almost the same time and then the second measuring session was performed.

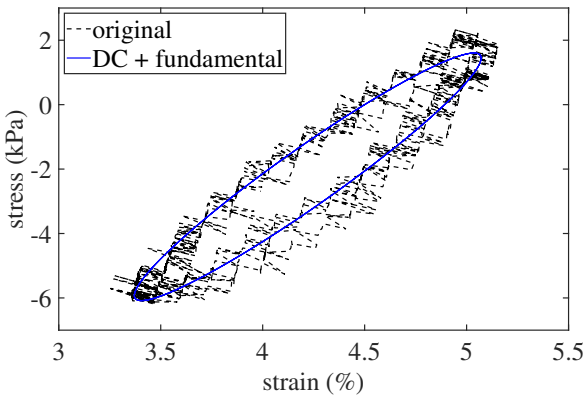

Figure 4.18: Forearm response (no insult) under a baseline strain to 4.2% and following a sinusoidal vibration with an amplitude of 0.8% at 1 Hz. The black dashed curve represents the original data and the blue solid curve shows the results after removing the harmonics.

4.3.4 Results

We remind that in this study, the loading pattern includes 10 s of prestrain to 4.2%, and then 10 cycles of sinusoidal vibration at 1 Hz with a much lower strain amplitude of 0.8% (Fig. 4.15). For data processing, the first six periods and the last period were dropped for the sake of stable results. Fig. 4.18 shows the original forearm skin response and the one after removing harmonics. The skin behaved rather linear at this strain level (baseline strain 4.2%, with vibration amplitude of 0.8%). The quantification of these curves was only based on the dynamic modulus. As the lower back data set is small ($n = 4$), the statistical analysis was only performed with forearm data set.

4.3.4.1 Intra-site variability and inter-site variability: on intact skin

To evaluate the variability of the measurements with the MIP, we first studied the variation on skin properties without any insults applied. The intra-site variation was evaluated with control site data (Ctrl_BL, Ctrl_I, Ctrl_R), representing the changes of the skin with time. The inter-site variation was evaluated with the baseline measurements at all sites (Ctrl_BL, TS_BL, IL_BL). For the lower back, an additional baseline was measured at the continuous loading site (CL_BL). This study is important for following analysis, concerning the changes introduced by skin insults.

For the inner forearm, a total of 40 measurements with the MIP yielded four parameters (dynamic modulus, loss tangent, storage modulus, and loss modulus), which are presented in Fig. 4.19. For the lower back, a total of 24 measurements on intact healthy skin are presented in Fig. 4.20. Descriptive statistics for each participant are presented in Table 4.5 and Table 4.6. It is evident that values for SD and the associated CV vary considerably across the cohort, with particularly high dynamic modulus values i.e. CV greater than 40%, for PS2 and PS09 and high loss tangent values for PS03 at the forearm site. On the other hand, the lower back data set is less varied in comparison with the forearm data set. It can be due to the fact that the participant was in prone position and had less degree of freedom compared to the

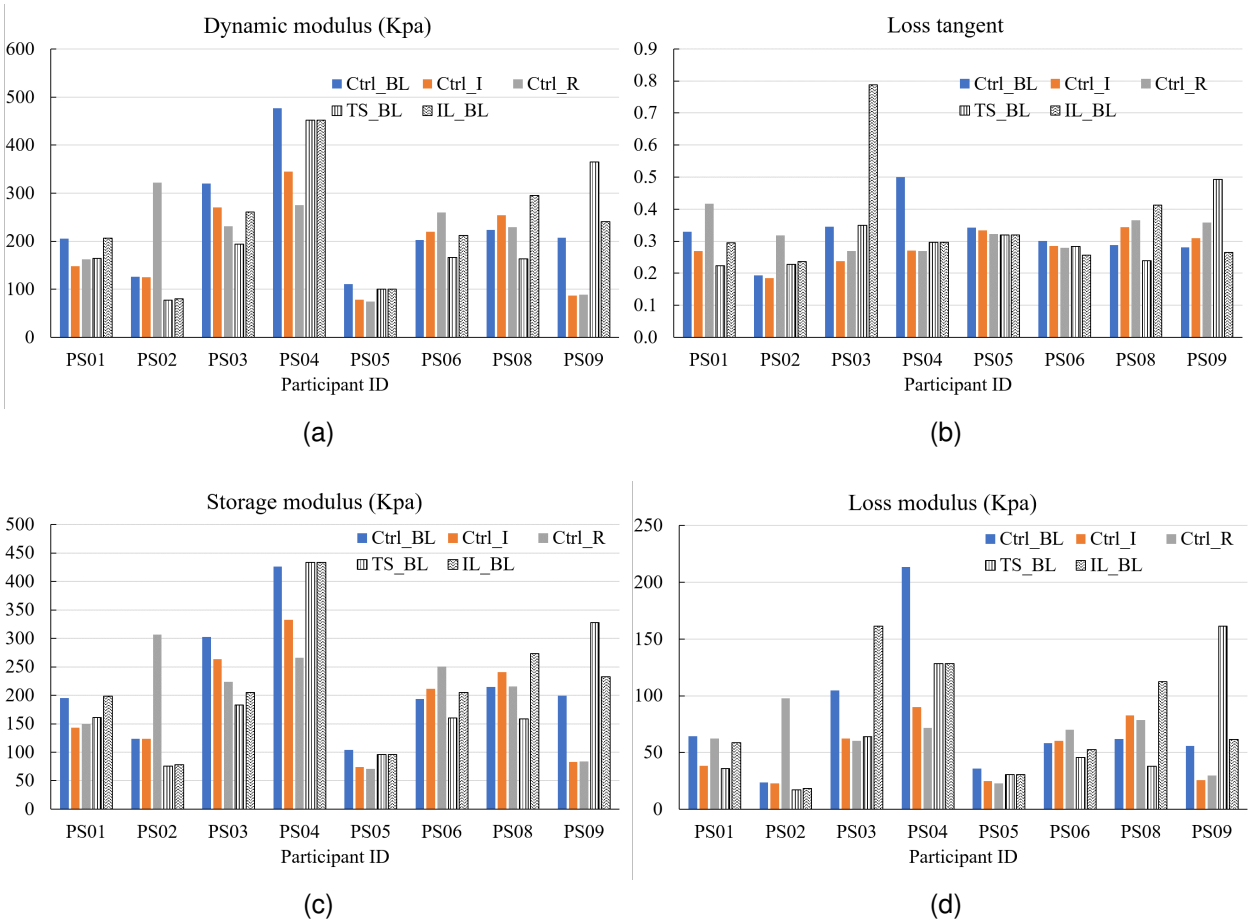

Figure 4.19: Mechanical skin parameters at forearm under a baseline strain to 4.2% and followed by a sinusoidal vibration with amplitude of 0.8% at 1 Hz. All data without insults are presented, including measurements from the control site (Ctrl_BL, Ctrl_I and Ctrl_R) and baseline data (BL) from the tape stripping site (TS_BL) and the intermittent loading site (IL_BL).

inner forearm tests, as seen in Fig. 4.14. There is a variation across the cohort of four participants with CV values for the dynamic modulus ranging between 8% and 23% and for the loss tangent of 6% to 25%.

The intra-site variability was evaluated with control site data (Ctrl_BL, Ctrl_I, Ctrl_R), measured at three different moments. The temporal variation may be caused by posture differences of the participant during the three measuring sessions. It may be noted, that for this study, as we are in a clinical situation, we may have discrepancy coming from the probe itself: the normal force of prototype V1 was not accurately controlled; and for both prototypes V1 and V2, the direction of the probe against the skin surface was not guaranteed. A one-way repeated measures ANOVA was conducted on the 8 individuals (forearm data set) to examine the effect that three different measuring moments had on skin mechanical parameters. Results showed that temporal variation is not statistically significant in dynamic modulus ($F(2, 14) = 0.94$, $P = 0.42$), loss tangent ($F(2, 14) = 1.24$, $P = 0.32$), storage modulus ($F(2, 14) = 0.82$, $P = 0.46$), and loss modulus ($F(2, 14) = 1.28$, $P = 0.31$).

Concerning the inter-site variability, the variation of skin parameters can be due to the site differences, as the skin properties vary from distal to proximal of the forearm [19]; and also to the previous discussed

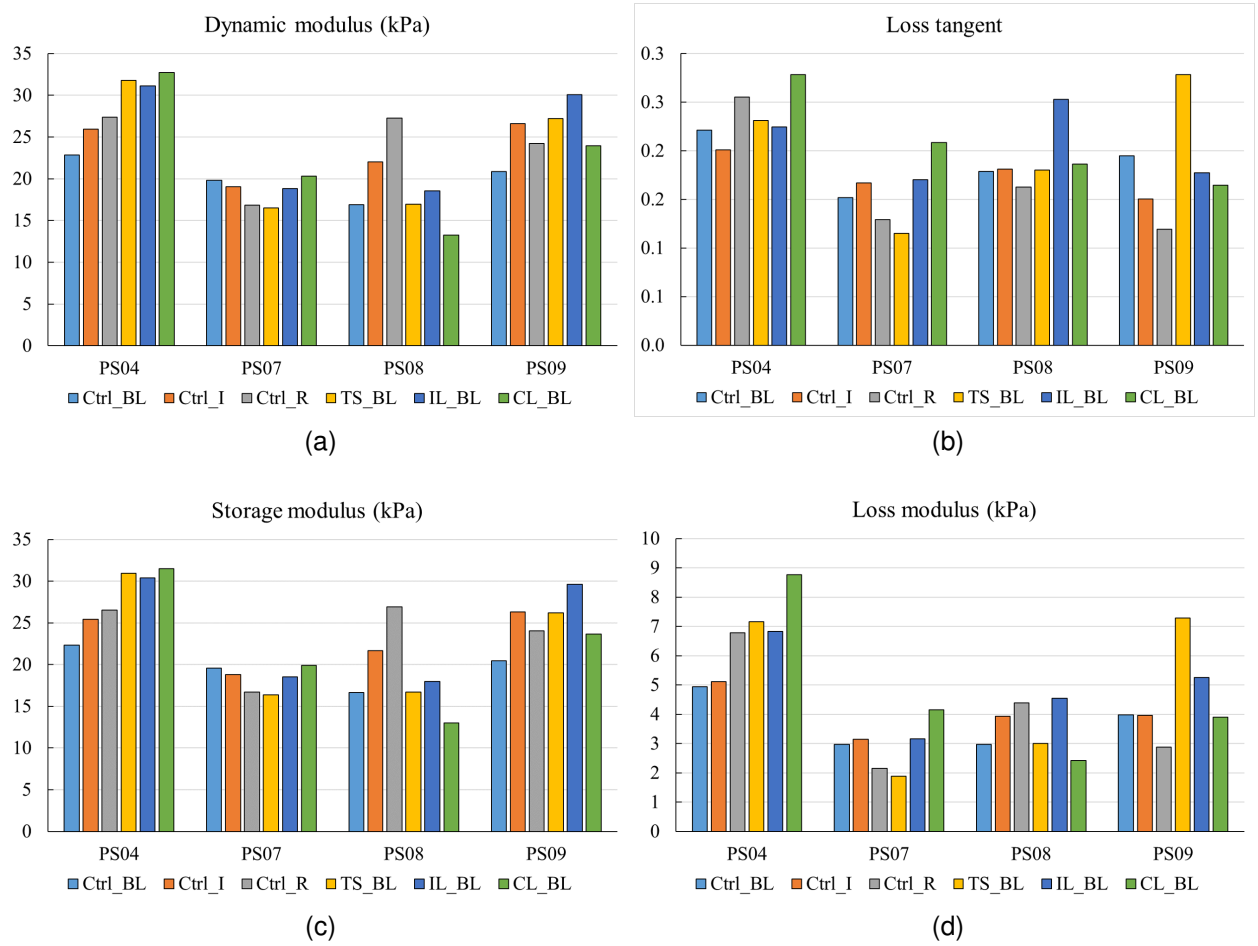

Figure 4.20: Mechanical skin parameters at lower back under a baseline strain to 4.2% and followed by a sinusoidal vibration with amplitude of 0.8% at 1 Hz. All data without insults are presented, including measurements from the control site (Ctrl_BL, Ctrl_I and Ctrl_R) and baseline data (BL) from the tape stripping site (TS_BL), the intermittent loading site (IL_BL), and the continuous loading site (CL_BL).

Table 4.5: Mean and coefficient of variation of skin dynamic modulus and loss tangent at forearm site.

Participant ID	Dynamic modulus				Loss tangent			
	Intra-site variability		Inter-site variability		Intra-site variability		Inter-site variability	
	Mean (kPa)	CV (%)	Mean (kPa)	CV (%)	Mean	CV (%)	Mean	CV (%)
PS01	171.86	17.50	192.36	12.49	0.34	21.95	0.28	19.24
PS02	190.87	59.34	94.49	28.63	0.23	32.13	0.22	10.54
PS03	274.13	16.23	258.46	24.43	0.28	19.47	0.49	51.42
PS04	365.61	27.95	460.24	3.09	0.35	38.37	0.36	32.4
PS05	87.74	22.44	103.93	5.37	0.33	2.96	0.33	4.15
PS06	227.25	13.04	193.46	12.43	0.29	19.43	0.28	24.49
PS08	235.7	6.95	227.23	29.18	0.33	11.87	0.31	28.38
PS09	127.42	54.22	270.85	30.72	0.32	12.52	0.35	36.88

Table 4.6: Mean and coefficient of variation of skin dynamic modulus and loss tangent at lower back site.

Participant ID	Dynamic modulus				Loss tangent			
	Intra-site variability		Inter-site variability		Intra-site variability		Inter-site variability	
	Mean (kPa)	CV (%)	Mean (kPa)	CV (%)	Mean	CV (%)	Mean	CV (%)
PS04	25.4	9.09	29.62	15.35	0.23	12.17	0.24	11.11
PS07	18.57	8.29	18.86	8.96	0.15	12.64	0.16	24.18
PS08	22.06	23.48	16.42	13.7	0.17	5.69	0.2	17.92
PS09	23.9	12.08	25.53	15.65	0.15	24.4	0.2	25.13

probe issues. Same statistical analysis was performed to study the inter-site variability. Results showed that site variation at the forearm is not statistically significant in dynamic modulus ($F(2, 14) = 0.57$, $P = 0.58$), loss tangent ($F(2, 14) = 0.42$, $P = 0.66$), storage modulus ($F(2, 14) = 0.52$, $P = 0.61$), and loss modulus ($F(2, 14) = 0.30$, $P = 0.74$).

In general, the reliability of the test with the MIP was verified.

4.3.4.2 Intact skin response: forearm vs. lower back

The intra-site and inter-site variations at the same body zone are not significant. We further combined the intact skin data to compare healthy forearm skin and lower back skin based on the dynamic modulus and loss tangent as shown in Fig. 4.21. The mean dynamic modulus of the forearm is 214 Kpa (75 kPa to 476 kPa), and the loss tangent of the forearm is 0.32. The corresponding values for the lower back are 23 Kpa (13 kPa to 33 kPa), and 0.19, respectively. These findings highlight that the dynamic modulus of the forearm is approximately nine times that of the lower back. In addition, the loss tangent for the forearm is approximate 50% larger than that of the lower back, meaning the forearm demonstrates a larger viscous component. A comparable study also reported that the modulus of the forearm was higher than the upper back one [91]. Another study based on suction tests also showed that the lower back had higher distensibility than the forearm, which means that the lower back skin was softer than the forearm skin [84]. The smaller dispersion at the lower back site can be explained by the following reasons: regarding the testing environment, the lower back was tested with the participant in the prone position, stable on a medical table; also, for the lower back site, we used the V2 MIP, which is designed to copy with lateral and normal shifts.

4.3.4.3 Response to insults

The forearm skin responses pre- and post-insult are compared in Fig. 4.22. We analyzed the relative change to the baseline value at each measuring moment for each testing site. For the control site, it is expected to have zero changes between the measuring moments. However, it is not the case, as seen in Fig. 4.22. This variations have already been discussed in intra-site variability 4.3.4.1. For the insult sites, they show different behavior in comparison to the control site, which indicate the effects of mechanical

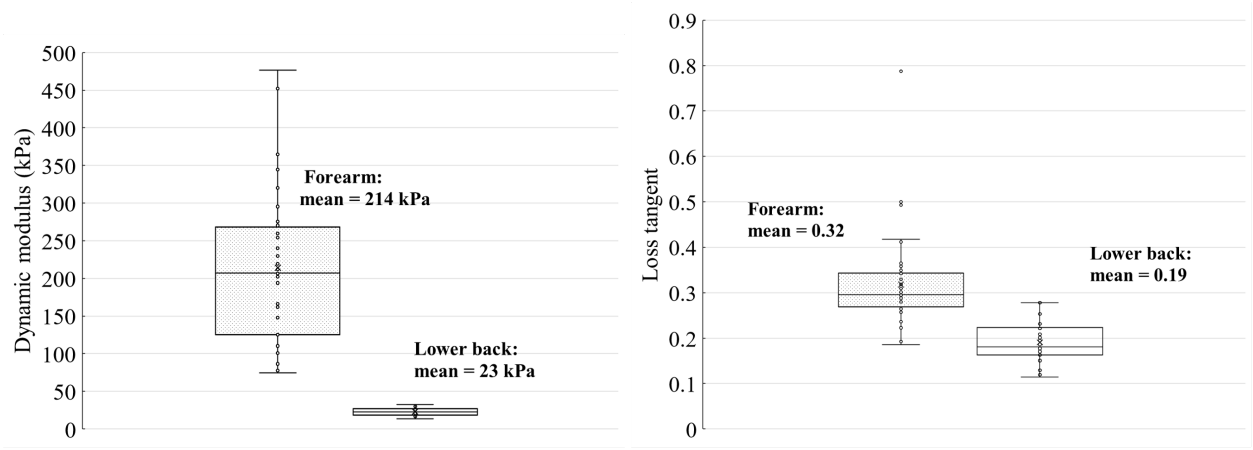

Figure 4.21: Forearm skin ($n = 8$, 40 measurements) vs lower back skin ($n = 4$, 24 measurements): (a) dynamic modulus (b) loss tangent.

insults.

The profiles of dynamic modulus and storage modulus after insults were very similar as seen in Fig. 4.22a and Fig. 4.22c. The dynamic modulus and storage modulus at insult sites are decreased more than the control site, where the largest decrease is observed at tape-stripping site (30%). Hence, tape-stripping and intermittent loading both tend to lower the dynamic modulus and storage modulus in lateral direction. The loss modulus measured right after insult in Fig. 4.22d is barely changed compared to the control site. After tape stripping, a temporary increase in loss tangent (ratio of loss modulus to storage modulus) is observed in Fig. 4.22b. It is mainly due to the reduced storage modulus in Fig. 4.22c. After 30 min "recovery", all the skin parameters tend to go back to the baseline.

Only four participants data are available at the lower back site. The skin response to the insults presented in Fig. 4.23 may not be representative. Nevertheless, following tape stripping, all the moduli are decreased (Fig. 4.23a,Fig. 4.23c, Fig. 4.23d). The loss modulus are reduced more than the storage modulus. Consequently, the loss tangent is decreased after tape stripping (Fig. 4.23b), which is the opposite of the forearm skin response (Fig. 4.22b). The two types of axial loading both tend to increase all the moduli. Specifically, intermittent loading increases more in the loss modulus than the continuous loading, while the increment of storage modulus is less than continuous loading. Accordingly, the loss tangent is increased after intermittent loading, and decreased after continuous loading, as shown in Fig. 4.23b. A moderate recovery is observed after 30 min recovery.

4.3.5 Discussion

In this Study №2, we attempted to use the MIP in a clinical environment. In comparison with the Study №1, the experimental conditions may be less reproducible from one test to another. Nevertheless, the estimated value of the loss tangent for the intact forearm skin was very close for the two separate studies,

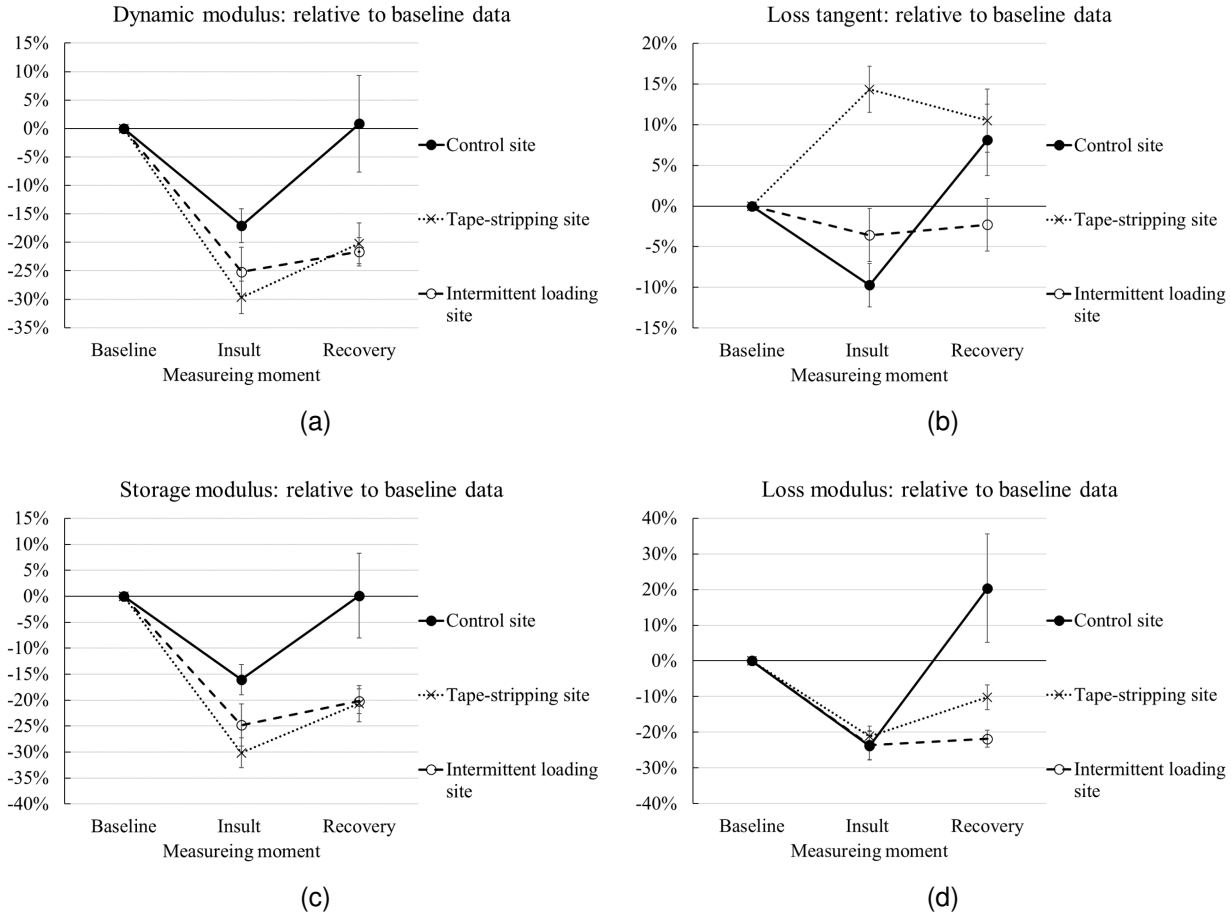

Figure 4.22: Forearm skin in response to insults (mean $\pm$ standard error, $n = 8$). Control site data are plotted as a reference. X axis represents the timeline, where three measurements were taken, including the baseline, the measurement after insult and the measurement after recovery. Y axis represents the relative change to the baseline value at each measuring moment.

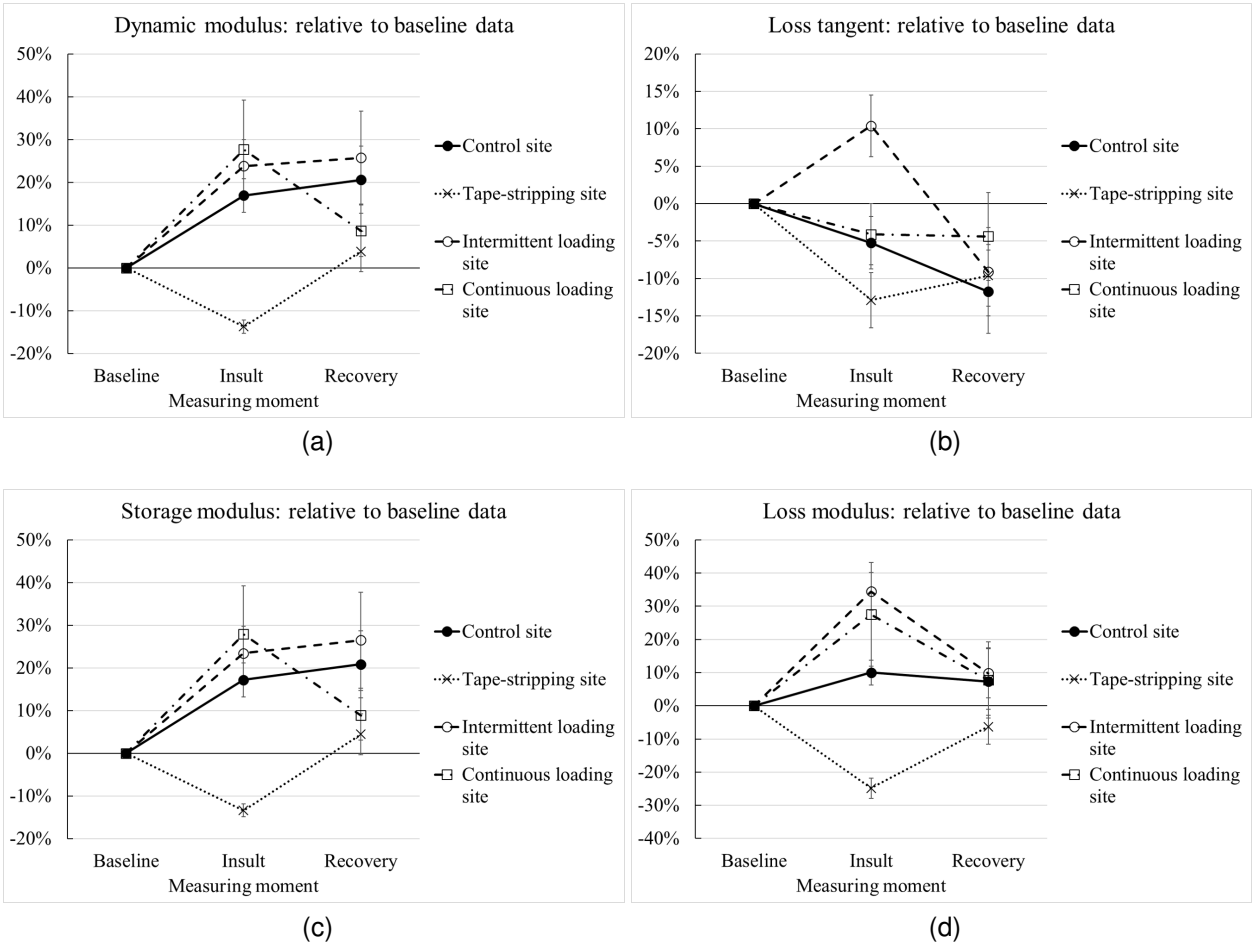

Figure 4.23: Lower back skin in response to insults (mean $\pm$ standard error, $n = 4$). Control site data are plotted as a reference. X axis represents the timeline, where three measurements were taken, including the baseline, the measurement after insult and the measurement after recovery. Y axis represents the relative change to the baseline value at each measuring moment.

about 0.3. This indicates that the loss tangent parameter is not too sensitive to the measurement protocol, such as "pretension" conditions. It is not really the case with respect to other skin parameters.

On the other hand, the dynamic modulus of the intact forearm skin, shows a larger dispersion compared to the rather stable results obtained at the lower back site. This difference in dispersion may be due to the positioning during the test: for the lower back measurements, all participants were lying prone, whereas for the forearm measurements, the participants were sitting in a chair with the arm resting on a table. They could change their arm position quite easily, even if they should not. Moreover, tests on the lower back were performed with the V2 MIP which could compensate the shifts in tangential and normal directions, e.g. the large movement due to breathing. However, despite these differences, we can conclude at least, that there is a clear variation in skin parameters derived from DMA tests at different skin sites such as the forearm and the lower back. In particular, forearm skin was characterized by a considerably higher dynamic modulus and a larger viscous component, compared to the lower back skin. As a reminder, site-specific variation has already been demonstrated in Study №1, comparing forearm skin and palm skin.

As for the ability of the MIP to detect skin damages, the first results given in Fig. 4.22 and Fig. 4.23 need to be discussed: it is obvious that at both sites (forearm and lower back), tape stripping, intermittent loading or even continuous loading change the skin characteristics. Unfortunately, these characteristics are also changed at the control site, which has not been insulted. Further studies with more participants are needed to confirm this phenomenon. Some hypotheses to explain this may be the change in the way to measure between the three steps (baseline, insult, and recovery) or the participant himself who may be anxious after the insult and induces changes in his body including the skin.

Nevertheless, these first results are encouraging if we consider the tape stripping insult: on the lower back as well as on the forearm, the tendency seems to be the same, namely a reduction of the dynamic modulus, greater than the changes registered at the control site. This is consistent with the literature where the stiffness (slope of the force–displacement curve) in the lateral direction was reduced after tape stripping [92]. Further experimental tests are needed to determine an available threshold beyond which we would be able to detect the insult using only the DMA tests.

4.4 Conclusion

In this chapter, the application of the mechanical impedance probe for *in vivo* measurements is presented. The skin behavior was first studied under large oscillation (strain amplitude up to 16.7%). The hysteresis loop and intra-cycle strain stiffening effect were captured by our measurements. A series of skin parameters (dissipated strain-energy density and dynamic modulus) were then deduced to quantify the skin behavior. The dissipated strain-energy density is a quantity that describes viscosity dissipation (hysteresis loss). Results show that the dissipated strain-energy density is linear to the strain range.

Our measurements show that the skin behaves differently over different body sites. For example, all

the skin parameters (dissipated strain-energy density, dynamic modulus, loss tangent, storage and loss moduli) were higher at the palm site than at the forearm site, characterized at a strain amplitude of 4.2%, 1 Hz. In particular, the dissipated strain-energy density and the loss modulus at palm site were about three times higher than the forearm ones. Another study shows that the forearm skin had a higher dynamic modulus and loss tangent than the lower back skin, characterized by a baseline strain of 4.2%, and an oscillating amplitude of 0.8% at 1 Hz.

Concerning the tests with insulted skin, after tape stripping, the lateral dynamic modulus and storage modulus were decreased and the loss tangent was increased for the forearm. These changes may be considered relevant enough to say that the MIP can detect the skin damage caused by tape stripping. Of course, a larger cohort size is needed to verify the clinical significance of the measurements with the MIP.

Conclusion and perspectives

Conclusion

This PhD. thesis aimed to develop a handheld probe to perform *in vivo* skin biomechanical measurements. It consists of two piezoelectric benders and a set of strain gauges that provide localized and independent measurements. The MIP applies tangential traction to the skin surface and measures skin response under quasi-static conditions (below $10\,\text{Hz}$). We have fulfilled the function requirements of the MIP, such as handheld, simultaneous sensing of the displacement and force, operating in a closed-loop displacement control, etc.

The mechanical structures of the MIP were optimized from a dual-pinned structure (V0) to a clamped-cantilever structure (V1 and V2). To adapt to clinical applications, MIP V2 was embedded with a normal force sensor and was designed with a floating base to compensate tangential and normal shifts at the skin surface during tests.

First, a linear mathematical model (2.15) was developed that allows simultaneous force and displacement measurements based on the bender voltage V and bending strain g. It was found that the relationship between tip displacement and bending strain was different in response to voltage excitation and to external force. We proposed a protocol to identify the sensing parameters from a free test and a blocking test. Although we are interested in the quasi-static mechanical properties of the skin, the sensing model is valid up to $100\,\text{Hz}$. It is noted that accurate displacement sensing (error less than 6% of full scale in open-loop tests) is achieved, while force sensing is less accurate due to hysteresis. Such inaccuracy is not negligible for skin characterization.

To improve the force sensing, the hysteresis behavior of the electromechanical system was studied and modeled. It was experimentally observed that the hysteresis exhibited between the input bender voltage to the output tip displacement (also the bending strain) under tip free condition. Whereas, the hysteresis was not present when the bender tip was blocked. The tip-free tests with high-voltage excitation at various frequencies (Fig. 2.19) also show that the hysteresis behavior can be regarded as rate-independent (below $100\,\text{Hz}$). The hysteresis behavior of piezoelectric actuators is usually described between the input voltage and output displacement. The influence of external force is rarely discussed. Considering the combined effects of the voltage (electric field) and the external force (stress), we modeled hysteresis with the instan-

taneous displacement relying on the Bouc–Wen model. The hysteresis model can predict the bending behavior even when driven by multi-harmonic voltages, according to experimental and simulation results. The first hysteresis compensation strategy based on an inverse model was validated at no load and loaded conditions (a spring load). However, to simplify the compensation process, another original strategy was proposed, relying on a closed-loop displacement control. Results demonstrate that the second approach also improves the accuracy of force sensing. Even though the hysteresis error can be slight, it may affect the diagnostic accuracy. Thus, it is necessary to implement hysteresis compensation to improve the precision of the *in vivo* measurements.

The distinction capability of the MIP was first demonstrated with tests on phantom skins. The MIP was finally applied to human skin measurements with validated sensing and closed-loop displacement control functions achieved in the early stages. Preliminary skin measurements show that the MIP can characterize skin viscoelasticity and skin responses are as expected from the literature. The highly integrated system enables us to perform *in vivo* tests with no other external devices required. With the MIP, we can obtain skin parameters such as strain-energy density dissipation and dynamic modulus. Experiments on human skin showed that the MIP can differentiate the skin between different anatomical sites (palm of hand, forearm and lower back) on the basis of the quantified skin parameters.

While the number of participants limits the generalizability of the skin insult study, the skin parameters characterized with the MIP show interesting changes in response to the insults applied to the tested forearm and lower back sites, especially for the tape-stripping insult. These results can be further studied to confirm the sensitivity of the MIP with a larger group of participants, and also to determine the threshold beyond which the disease is significant.

Perspectives

This thesis brings a contribution to the rapid evaluation of skin mechanical properties. Accounting for its design, the MIP is a portable probe that can be used in a standalone way. We have achieved *in vivo* skin characterization with the MIP and verified the discrimination capability in terms of body site. In addition, the first results on skin damage discrimination are encouraging.

Beyond the work we've done, there is still a lot we can continue to explore.

Firstly, improvements may be brought to the probe. If version V2 seems to be the best one we had, we may improve its robustness, in case of wide use by non-technical people. The slip issue at the tip levels should also be addressed: either by reducing the risk of slip thanks to other materials at the tip level, or by defining different measurement protocols. The tip material must be studied as it is in contact with the body and must not be painful on the skin, especially on damaged skin.

Secondly, it would be interesting to understand the results of the MIP with respect to the type of insult we applied: damage caused by tape stripping appears to be easier to detect than global pressure like

normal loading. These two insults are quite different. The former acts on the surface of the skin and the latter can act on the dermis layer or even underneath. The evaluation of the discrimination possibilities of the MIP is still to be studied, in particular, to determine the relevance of its measurement in relation to the depth where the damage occurs. This is essential if we want to use this kind of probe for the early detection of PUs.

Last but not least, it is mandatory to enlarge the number of trials to obtain statistically relevant results. Skin is a living material that has different behaviors regarding the individuals, the body sites, and also regarding diseases. With a huge data set, it will be possible, perhaps with the help of artificial intelligence, to determine the threshold values of mechanical parameters at which the diagnosis becomes relevant.

Beyond the scope of early diagnosis, this study may also be of interest for skin modeling, as it can provide a solution for acquiring valuable experimental data, for example for finite element analysis, which can be further used in the design of health care products (mattress, cushion...) or even in the cosmetic field.

Appendix A

Prototype V0: dual-pinned structure

A.1 Assembly process

The prototype V0 was assembled in dual-pinned condition with bender model CMBP07 from Noliac, as shown in Fig. A.1. Two side PCBs were used to place the pins. The foil strain gauges were glued on both sides of the benders, forming a Wheatstone bridge. The output of bridge was then amplified with an instrumentation amplifier. The strain gauge lead wires were also connected to the side PCBs.

A.2 Calibration

The relationship between tip displacement and gauge signal was studied with setups shown in Fig. A.2. In tip-free tests, the probe was held tightly by the vise clamp table. The two benders were driven by a linear amplifier (LPA 400 B), with a sinusoidal voltage at $1\,\mathrm{Hz}$, $V_{\mathrm{pp}} = 195\,\mathrm{V}$. A laser displacement sensor (Vibrometer, Polytec OFV-534) was used to measure the tip displacement, with a sensitivity of $160\,\mu\mathrm{m/V}$, seen in Fig. A.2a. The probe was turned over so that we could measure the displacement of the second

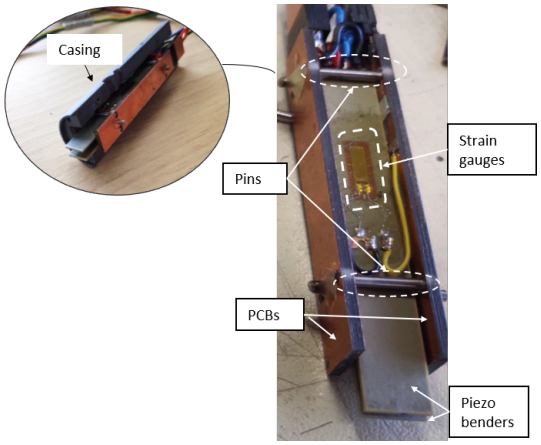

Figure A.1: Prototype V0 in dual-pinned condition. Piezoelectric bender model CMBP07 from Noliac.

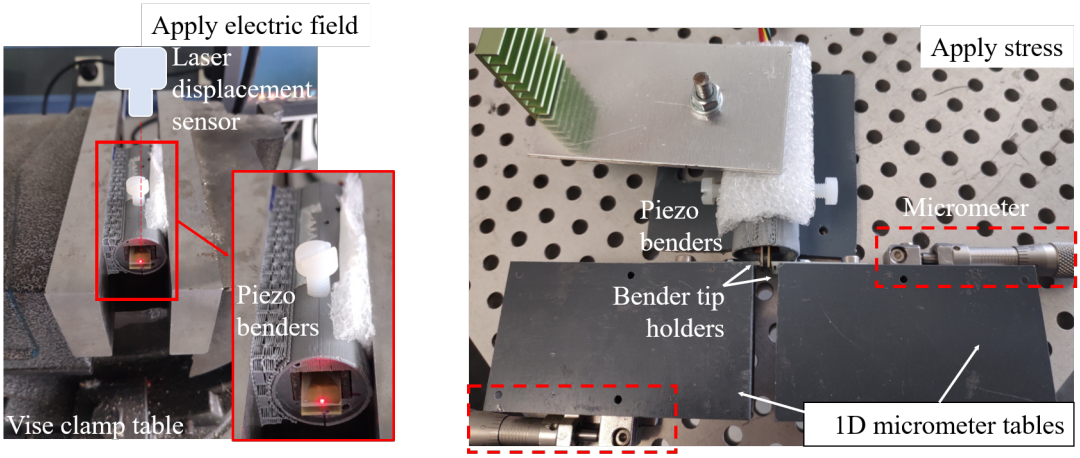

(a) (b)

Figure A.2: Calibration setups for dual-pinned piezo benders (prototype V0). (a) Free tests when subjected to electrical field, tip displacement was measured by a laser displacement sensor.(b) Loading tests with 1D micrometer tables.

bender. By this means, we obtained the relative displacement between the two bender tips. The strain signal and tip displacement were collected by PicoScope 6. While, the displacement–strain curve in response to external stress was obtained with a setup seen in Fig. A.2b. A pair of lab designed bender tip holders were attached to 1D micrometer tables. The bender tips were fitted inside the waved rectangular holes of the holders. In such a way, the bender tips can be stretched out and pressed together by tuning the position of the 1D micrometer tables. The position of the two benders were read from the 1D micrometer and the strain signal was measured through Multimeter Beta (Gould Advance Ltd).

Different proportional coefficients were found by linearly fitting the displacement–strain curves (Fig. A.3), when subjected to electric field and stress, respectively. In Fig. A.3a, a non-symmetric behavior is present when the bender tips are moving away (positive displacement) or moving together (negative displacement). We treated the raw data separately according to positive or negative displacement. This asymmetry can be resulting from the bad layout of the components. The surrounding circuits or mechanical structure (Fig. A.1) may obstruct the bending movement.

Overall, the coefficient obtained under stress excitation is larger than that when excited by electrical field. The results indicate that the piezoelectric strain in response to electric field and external stress are not identical in such configuration. These tests helped establish the system calibration protocol.

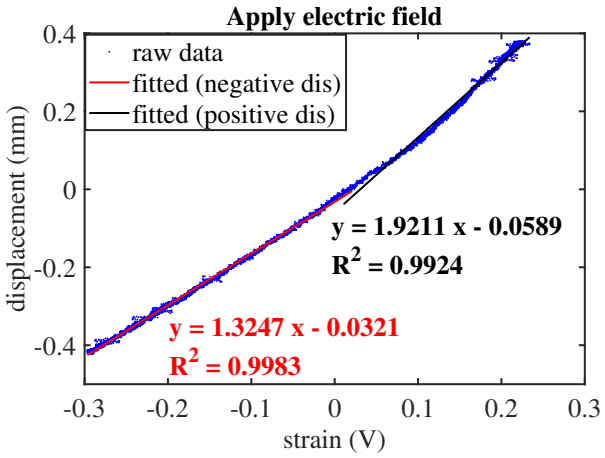

(a)

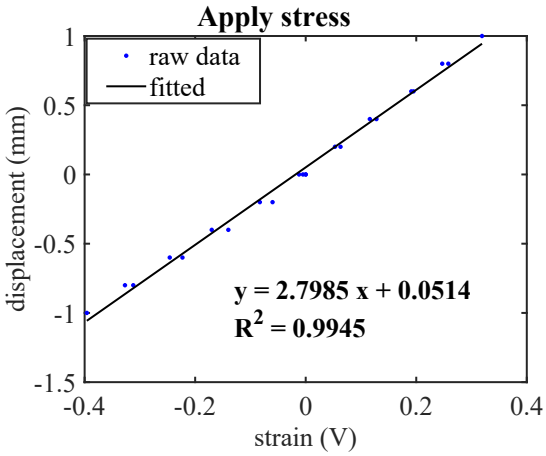

(b)

Figure A.3: Relative tip displacement against strain (prototype V0), when subjected to (a) sinusoidal voltage at 1 Hz, $V_{\mathrm{pp}} = 195$ V; (b) external stress applied by 1D micrometer tables. Positive displacement means moving the two bender tips away from each other, while negative displacement means moving the two bender tips together. The strain is shown with the DC bias removed. In (a), the linear fitting was performed with positive displacement and negative displacement, separately.

Appendix B

Specifications of the piezoelectric benders

Table B.1: Specifications of the piezoelectric benders.

Manufacturer	Model	Operating voltage max (V)	Displacement (mm)	Blocking force max (N)	Length (mm) active/total	Width (mm)	Height (mm)
Noliac	CMBP07	200	± 1.270	± 0.4	46.5/50	7.8	0.7
PiezoDrive	BA5010	150	± 1.5	± 0.3	43/50	10	0.8
ThorLabs	PB4NB2S	150	± 0.450	1.5	28/32	7.8	0.8
Bimitech	PBA3020-5H200	160	± 0.48	± 0.48	30/50	20	0.65
PI	PL128.10	60	± 0.450	± 0.55	28/36	6.15	0.67
PIEZO	T220-H4BR-1305YE*			*refer to [66]			

Appendix C

Strain gauge installation

The strain gauges were glued to the bender surfaces as follows:

1) Gluing preparation. Degrease the piezoelectric bender surfaces with a solvent (Acetone) gently. Use sellotape to pick the strain gauge, sticking to the surface with wire lead;

2) Mix adhesive (3M™Scotch-Weld™Epoxy Adhesive DP190 Gray). Apply a small drop of mixed adhesive on the flat surface of strain gauge base;

3) Place the gauge on the bender surface and stick the whole length of sellotape to keep the gauge in position (Fig. C.1a). Use an apparatus like Fig. C.1b to press the gauge evenly during gluing.

4) Curing. To speed up curing, we put the apparatus together with the glued piezo benders into an oven (Binder), heating up to 70 ℃ within 1 h and curing for another 5 h, then cooling down with 1 h to 2 h.

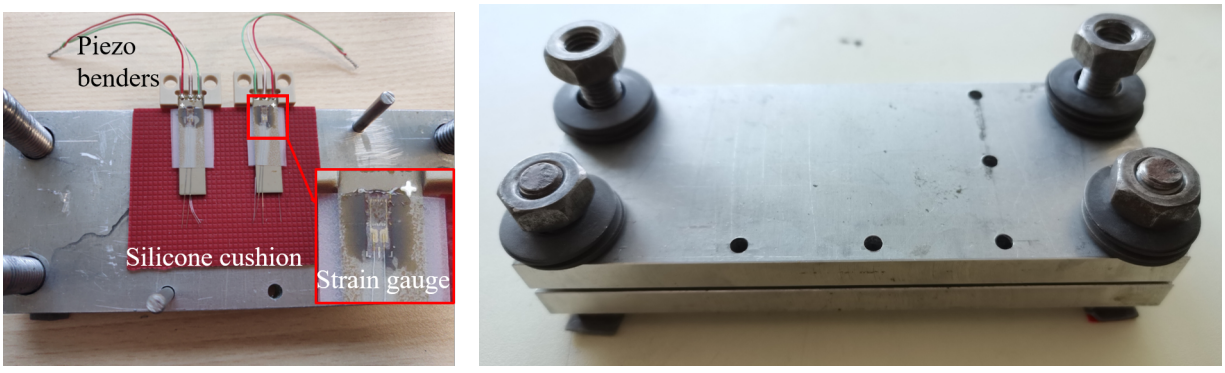

(a) (b)

Figure C.1: Strain gauge installation. (a) Strain gauges glued on the piezo bender surfaces. (b) Apparatus used to apply evenly distributed pressure for strain gauge gluing. The piezo benders with strain gauges adhered were placed between the upper and lower parts of the apparatus.

Appendix D

Blocking tests (additional results)

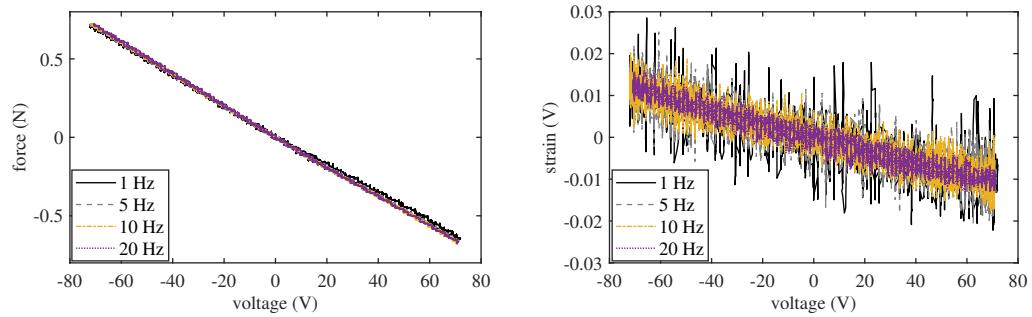

Figure D.1: Blocking force (a) and strain (b) when the piezo bender was subjected to a full-scale sinusoidal voltage with its tip blocked. The horizontal coordinate represents the driving voltage.

Appendix E

Calibration of the PCB spring

The PCB made spring was calibrated with a setup shown in Fig. E.1. A 1D micrometer table fixed on a support is used to apply a displacement to the spring and the reaction force of the spring is measured by a high resolution weighing scale. The PCB spring on one side is connected to the 1D micrometer table to transmit the displacement. On the other side, the spring is connected to a mass, so that the spring force can be measured. The mass is used to preload the weighing scale so that a good contact is maintained even when the spring is pulled up.

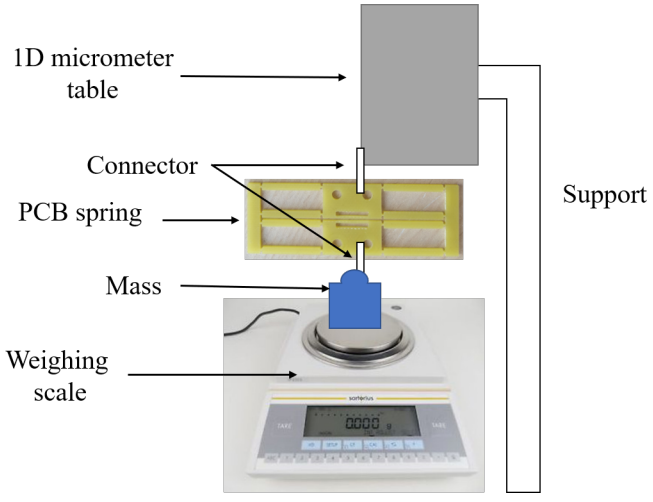

Figure E.1: Setup for PCB spring calibration.

Appendix F

Skin data

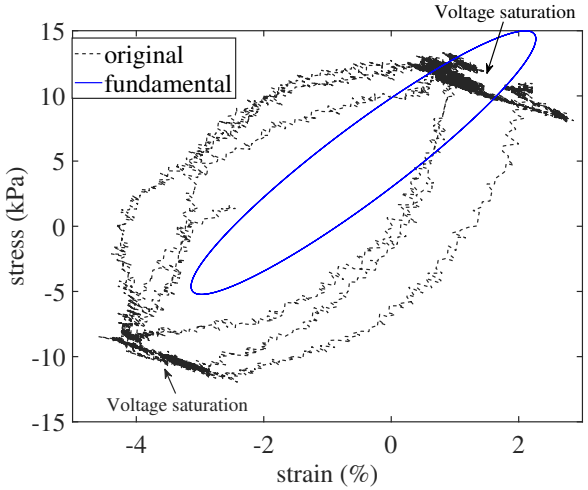

Figure F.1: Stress–strain curve of P02 measured at palm of the hand. The sharp turning of the curves is due to voltage saturation. Peak-to-peak strain was 7.45% less than the required 8.3%.

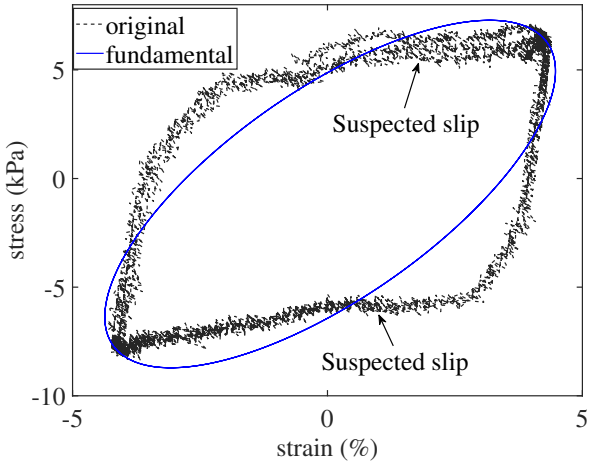

Figure F.2: Stress–strain curve of P08 measured at palm of the hand. Slip may present as the stress stops increasing with the increased strain.

Bibliography

[1] J. L. Zeller, C. Lynm, and R. M. Glass, “Pressure ulcers,” *JAMA*, vol. 296, no. 8, p. 1020, Aug. 2006.

[2] D. Bader, “Chapter 23 - Pressure ulceration,” in *Clinical Engineering (Second Edition)*, A. Taktak, P. S. Ganney, D. Long, and R. G. Axell, Eds. Academic Press, Jan. 2020, pp. 391–402.

[3] J. S. Mervis and T. J. Phillips, “Pressure ulcers: Pathophysiology, epidemiology, risk factors, and presentation,” *Journal of the American Academy of Dermatology*, vol. 81, no. 4, pp. 881–890, Oct. 2019.

[4] T. V. Boyko, M. T. Longaker, and G. P. Yang, “Review of the current management of pressure ulcers,” *Advances in Wound Care*, vol. 7, no. 2, pp. 57–67, Sep. 2016.

[5] G. Bennett, C. Dealey, and J. Posnett, “The cost of pressure ulcers in the UK,” *Age Ageing*, vol. 33, no. 3, pp. 230–235, May 2004.

[6] C. D. J. P. A. Walker, “The cost of pressure ulcers in the United Kingdom,” *Journal of Wound Care*, Aug. 2013.

[7] “Development of pressure ulcers: Causes and signs – Scottish acquired brain injury network.”

[8] Q. Wang, L. Kong, S. Sprigle, and V. Hayward, “Portable gage for pressure ulcer detection,” in *2006 International Conference of the IEEE Engineering in Medicine and Biology Society*, Aug. 2006, pp. 5997–6000.

[9] A. Pissarenko, W. Yang, H. Quan, K. A. Brown, A. Williams, W. G. Proud, and M. A. Meyers, “Tensile behavior and structural characterization of pig dermis,” *Acta Biomaterialia*, vol. 86, pp. 77–95, Mar. 2019.

[10] W. Maurel, D. Thalmann, Y. Wu, and N. M. Thalmann, *Biomechanical Models for Soft Tissue Simulation*. Springer, 1998, vol. 48.

[11] M. Hoffman and MD, “The skin (human anatomy): Picture, definition, function, and skin conditions,” https://www.webmd.com/skin-problems-and-treatments/picture-of-the-skin.

[12] A. Pissarenko and M. A. Meyers, “The materials science of skin: Analysis, characterization, and modeling,” *Progress in Materials Science*, vol. 110, p. 100634, May 2020.

[13] J. F. M. Manschot and A. J. M. Brakkee, “The measurement and modelling of the mechanical properties of human skin in vivo—I. The measurement,” *Journal of Biomechanics*, vol. 19, no. 7, pp. 511–515, Jan. 1986.

[14] F. Khatyr, C. Imberdis, P. Vescovo, D. Varchon, and J.-M. Lagarde, “Model of the viscoelastic behaviour of skin in vivo and study of anisotropy,” *Skin Research and Technology*, vol. 10, no. 2, pp. 96–103, 2004.

[15] K. H. Lim, C. M. Chew, P. C. Y. Chen, S. Jeyapalina, H. N. Ho, J. K. Rappel, and B. H. Lim, “New extensometer to measure in vivo uniaxial mechanical properties of human skin,” *Journal of Biomechanics*, vol. 41, no. 5, pp. 931–936, Jan. 2008.

[16] E. Jacquet, S. Joly, J. Chambert, K. Rekik, and P. Sandoz, “Ultra-light extensometer for the assessment of the mechanical properties of the human skin in vivo,” *Skin Research and Technology*, vol. 23, no. 4, pp. 531–538, 2017.

[17] W. A. B. Wan Abas and J. C. Barbenel, “Uniaxial tension test of human skin in vivo,” *Journal of Biomedical Engineering*, vol. 4, no. 1, pp. 65–71, Jan. 1982.

[18] W. A. Sodeman and G. E. Burch, “A direct method for the estimation of skin distensibility with its application to the study of vascular states,” *J. Clin. Invest.*, vol. 17, no. 6, pp. 785–793, Nov. 1938.

[19] E. Jacquet, J. Chambert, J. Pauchot, and P. Sandoz, “Intra- and inter-individual variability in the mechanical properties of the human skin from in vivo measurements on 20 volunteers,” *Skin Research and Technology*, vol. 23, no. 4, pp. 491–499, 2017.

[20] C. Pailler-Mattei, S. Bec, and H. Zahouani, “In vivo measurements of the elastic mechanical properties of human skin by indentation tests,” *Medical Engineering & Physics*, vol. 30, no. 5, pp. 599–606, Jun. 2008.

[21] N. Krueger, S. Luebberding, M. Oltmer, M. Streker, and M. Kerscher, “Age-related changes in skin mechanical properties: A quantitative evaluation of 120 female subjects,” *Skin Research and Technology*, vol. 17, no. 2, pp. 141–148, 2011.

[22] S. Luebberding, N. Krueger, and M. Kerscher, “Mechanical properties of human skin in vivo: A comparative evaluation in 300 men and women,” *Skin Research and Technology*, vol. 20, no. 2, pp. 127–135, 2014.

[23] J. L. Leveque, J. de Rigal, P. G. Agache, and C. Monneur, “Influence of ageing on the in vivo extensibility of human skin at a low stress,” *Arch Dermatol Res*, vol. 269, no. 2, pp. 127–135, Nov. 1980.

[24] M. Blair, J. Jones, A. Woessner, and K. Quinn, “Skin structure-function relationships and the wound healing response to intrinsic aging,” *Advances in Wound Care*, vol. 9, no. 3, pp. 127–143, 2020.

[25] J. Lim, C. J. Lim, S. Kim, G. Nam, M. Chang, K. Park, K. Park, H. J. Kim, J. K. Ahn, and S. Jeong, “Antiaging and antioxidant effects of topical autophagy activator: A randomized, placebo-controlled, double-blinded study,” *Journal of Cosmetic Dermatology*, vol. 18, no. 1, pp. 197–203, 2019.

[26] J. Willard, “Mechano-modulation of burn wound repair,” Thesis, The Ohio State University, Jun. 2012.

[27] W. Yang, V. R. Sherman, B. Gludovatz, E. Schaible, P. Stewart, R. O. Ritchie, and M. A. Meyers, “On the tear resistance of skin,” *Nat Commun*, vol. 6, no. 1, p. 6649, May 2015.

[28] Z. Moore, D. Patton, S. L. Rhodes, and T. O’Connor, “Subepidermal moisture (SEM) and bioimpedance: A literature review of a novel method for early detection of pressure-induced tissue damage (pressure ulcers),” *International Wound Journal*, vol. 14, no. 2, pp. 331–337, 2017.

[29] L. Russell, “Pressure ulcer classification: Defining early skin damage,” *Br J Nurs*, vol. 11, no. Sup3, pp. S33–S41, Sep. 2002.

[30] A. Gefen and G. Ross, “The subepidermal moisture scanner: The technology explained,” *J Wound Care*, vol. 29, no. Sup2c, pp. S10–S16, Feb. 2020.

[31] H. Okonkwo, R. Bryant, J. Milne, D. Molyneaux, J. Sanders, G. Cunningham, S. Brangman, W. Eardley, G. K. Chan, B. Mayer, M. Waldo, and B. Ju, “A blinded clinical study using a subepidermal moisture biocapacitance measurement device for early detection of pressure injuries,” *Wound Repair and Regeneration*, vol. 28, no. 3, pp. 364–374, 2020.

[32] S. L. Swisher, M. C. Lin, A. Liao, E. J. Leeflang, Y. Khan, F. J. Pavinatto, K. Mann, A. Naujokas, D. Young, S. Roy, M. R. Harrison, A. C. Arias, V. Subramanian, and M. M. Maharbiz, “Impedance sensing device enables early detection of pressure ulcers in vivo,” *Nat Commun*, vol. 6, no. 1, pp. 1–10, Mar. 2015.

[33] J. Wang, D. M. Brienza, P. Karg, and G. G. Bertocci, “Viscoelastic properties of buttock soft tissues with pressure ulcer susceptibility,” in *Proceedings of the RESNA 25th International Conference: Technology and Disability: Research, Design, Practice and Policy. Arlington, VA: RESNA*, 2002, pp. 330–2.

[34] A. Scheel-Sailer, A. Frotzler, G. Mueller, S. Annaheim, R. M. Rossi, and S. Derler, “Biophysical skin properties of grade 1 pressure ulcers and unaffected skin in spinal cord injured and able-bodied persons in the unloaded sacral region,” *Journal of Tissue Viability*, vol. 26, no. 2, pp. 89–94, May 2017.

[35] C. Dagdeviren, Y. Shi, P. Joe, R. Ghaffari, G. Balooch, K. Usgaonkar, O. Gur, P. L. Tran, J. R. Crosby, M. Meyer, Y. Su, R. Chad Webb, A. S. Tedesco, M. J. Slepian, Y. Huang, and J. A. Rogers, “Confor-

mal piezoelectric systems for clinical and experimental characterization of soft tissue biomechanics," *Nature Mater*, vol. 14, no. 7, pp. 728–736, Jul. 2015.

[36] M. Rakotondrabe, Ed., *Smart Materials-Based Actuators at the Micro/Nano-Scale*. New York, NY: Springer New York, 2013.

[37] "Piezoelectricity," *Wikipedia*, Dec. 2022.

[38] A. Jbaily and R. W. Yeung, "Piezoelectric devices for ocean energy: A brief survey," *J. Ocean Eng. Mar. Energy*, vol. 1, no. 1, pp. 101–118, Feb. 2015.

[39] C.-L. Yang, K.-W. Chen, and C.-D. Chen, "Model and characterization of a press-button-type piezoelectric energy harvester," *IEEE/ASME Transactions on Mechatronics*, vol. 24, no. 1, pp. 132–143, Feb. 2019.

[40] Y.-F. Su, G. Han, Z. Kong, T. Nantung, and N. Lu, "Embeddable piezoelectric sensors for strength gain monitoring of cementitious materials: The influence of coating materials," *Engineered Science*, vol. Volume 11 (September 2020), no. 10, pp. 66–75, Jul. 2020.

[41] R. Darleux, B. Lossouarn, and J.-F. Deü, "Broadband vibration damping of non-periodic plates by piezoelectric coupling to their electrical analogues," *Smart Mater. Struct.*, vol. 29, no. 5, p. 054001, Mar. 2020.

[42] Q.-M. Wang, X.-H. Du, B. Xu, and L. Cross, "Electromechanical coupling and output efficiency of piezoelectric bending actuators," *IEEE Transactions on Ultrasonics, Ferroelectrics, and Frequency Control*, vol. 46, no. 3, pp. 638–646, May 1999.

[43] Y. Fuda, M. Murata, and Y. Matsuo, "Multilayer piezoelectric ceramic bimorph actuator," *Jpn. J. Appl. Phys.*, vol. 24, no. S2, p. 485, Jan. 1985.

[44] T. Hemsel, R. Stroop, D. Oliva Uribe, and J. Wallaschek, "Resonant vibrating sensors for tactile tissue differentiation," *Journal of Sound and Vibration*, vol. 308, no. 3, pp. 441–446, Dec. 2007.

[45] L. Sienkiewicz, M. Ronkowski, G. Kostro, R. Ryndzionek, and J. Rouchon, "Identification of the mechanical properties of the skin by electromechanical impedance analysis of resonant piezoelectric actuator," in *IECON 2013 - 39th Annual Conference of the IEEE Industrial Electronics Society*, Nov. 2013, pp. 3940–3945.

[46] L. K. Sienkiewicz, "Concept, implementation and analysis of the piezoelectric resonant sensor/actuator for measuring the aging process of human skin," Ph.D. dissertation, Toulouse, INPT, 2016.

[47] Q. Wang and V. Hayward, "In vivo biomechanics of the fingerpad skin under local tangential traction," *Journal of Biomechanics*, vol. 40, no. 4, pp. 851–860, Jan. 2007.

[48] “Introduction to ultrasonic drivers,” Apr. 2019.

[49] E. M. Sales de Castro, F. Giraud, B. Lemaire-Semail, and M. Amberg, “Vector controlled ultrasonic transducer applied to soft material mechanical impedance estimation,” in *2021 IEEE International Workshop of Electronics, Control, Measurement, Signals and Their Application to Mechatronics (ECMSM)*, Jun. 2021, pp. 1–5.

[50] E. M. Sales De Castro, F. Giraud, and B. Semail, “Low-frequency ultrasound skin mechanical impedance sensor for Pressure Ulcer diagnostic,” 2022.

[51] D. A. Torres, A. Kaci, F. Giraud, C. Giraud-Audine, M. Amberg, S. Clenet, and B. Lemaire-Semail, “PCA model of fundamental acoustic finger force for out-of-plane ultrasonic vibration and its correlation with friction reduction,” *IEEE Transactions on Haptics*, vol. 14, no. 3, pp. 551–563, Jul. 2021.

[52] “IEEE Standard on Piezoelectricity,” *ANSI/IEEE Std 176-1987*, pp. 0_1–, 1988.

[53] M. Goldfarb and N. Celanovic, “Modeling piezoelectric stack actuators for control of micromanipulation,” *IEEE Control Systems*, p. 11, 1997.

[54] S. Devasia, E. Eleftheriou, and S. O. R. Moheimani, “A Survey of Control Issues in Nanopositioning,” *IEEE Transactions on Control Systems Technology*, vol. 15, no. 5, pp. 802–823, Sep. 2007.

[55] D. Sabarianand, P. Karthikeyan, and T. Muthuramalingam, “A review on control strategies for compensation of hysteresis and creep on piezoelectric actuators based micro systems,” *Mechanical Systems and Signal Processing*, vol. 140, p. 106634, Jun. 2020.

[56] S. R. Moheimani and A. J. Fleming, *Piezoelectric Transducers for Vibration Control and Damping*. Springer, 2006, vol. 1.

[57] M. Mohammadzaheri, S. Grainger, and M. Bazghaleh, “A system identification approach to the characterization and control of a piezoelectric tube actuator,” *Smart Mater. Struct.*, vol. 22, no. 10, p. 105022, Oct. 2013.

[58] M. Bazghaleh, S. Grainger, and M. Mohammadzaheri, “A review of charge methods for driving piezoelectric actuators,” *Journal of Intelligent Material Systems and Structures*, vol. 29, no. 10, pp. 2096–2104, Jun. 2018.

[59] M. Goldfarb and N. Celanovic, “A lumped parameter electromechanical model for describing the nonlinear behavior of piezoelectric actuators,” *Journal of Dynamic Systems, Measurement, and Control*, vol. 119, no. 3, pp. 478–485, Sep. 1997.

[60] C. Yang and K. Youcef-Toumi, “Principle, implementation, and applications of charge control for piezo-actuated nanopositioners: A comprehensive review,” *Mechanical Systems and Signal Processing*, vol. 171, p. 108885, May 2022.

[61] M. Rakotondrabe, I. A. Ivan, S. Khadraoui, P. Lutz, and N. Chaillet, “Simultaneous displacement/force self-sensing in piezoelectric actuators and applications to robust control,” *IEEE/ASME Transactions on Mechatronics*, vol. 20, no. 2, pp. 519–531, Apr. 2015.

[62] P. Ronkanen, P. Kallio, and H. N. Koivo, “Current control of piezoelectric actuators with power loss compensation,” in *IEEE/RSJ International Conference on Intelligent Robots and Systems*, vol. 2, Sep. 2002, pp. 1948–1953 vol.2.

[63] G. M. Clayton, S. Tien, A. J. Fleming, S. O. R. Moheimani, and S. Devasia, “Inverse-feedforward of charge-controlled piezopositioners,” *Mechatronics*, vol. 18, no. 5, pp. 273–281, Jun. 2008.

[64] M. Mridha and S. Ödman, “Characterization of subcutaneous edema by mechanical impedance measurements,” *Journal of Investigative Dermatology*, vol. 85, no. 6, pp. 575–578, Dec. 1985.

[65] J. G. Smits, S. I. Dalke, and T. K. Cooney, “The constituent equations of piezoelectric bimorphs,” *Sensors and Actuators A: Physical*, vol. 28, no. 1, pp. 41–61, Jun. 1991.

[66] Qi Wang and V. Hayward, “Biomechanically optimized distributed tactile transducer based on lateral skin deformation,” *The International Journal of Robotics Research*, vol. 29, no. 4, pp. 323–335, Apr. 2010.

[67] R. Seethaler, S. Z. Mansour, M. G. Ruppert, and A. J. Fleming, “Position and force sensing using strain gauges integrated into piezoelectric bender electrodes,” *Sensors and Actuators A: Physical*, p. 112416, Nov. 2020.

[68] H. Hu and R. Ben Mrad, “On the classical Preisach model for hysteresis in piezoceramic actuators,” *Mechatronics*, vol. 13, no. 2, pp. 85–94, Mar. 2003.

[69] V. M. Miron, S. Lämmermann, U. Çakmak, and Z. Major, “Material characterization of 3D-printed silicone elastomers,” *Procedia Structural Integrity*, vol. 34, pp. 65–70, Jan. 2021.

[70] D. A. Hall, “Review nonlinearity in piezoelectric ceramics,” *Journal of Materials Science*, vol. 36, no. 19, pp. 4575–4601, Oct. 2001.

[71] P. Ge and M. Jouaneh, “Generalized preisach model for hysteresis nonlinearity of piezoceramic actuators,” *Precision Engineering*, vol. 20, no. 2, pp. 99–111, Mar. 1997.

[72] S. Xiao and Y. Li, “Modeling and High Dynamic Compensating the Rate-Dependent Hysteresis of Piezoelectric Actuators via a Novel Modified Inverse Preisach Model,” *IEEE Transactions on Control Systems Technology*, vol. 21, no. 5, pp. 1549–1557, Sep. 2013.

[73] W. T. Ang, P. K. Khosla, and C. N. Riviere, “Feedforward Controller With Inverse Rate-Dependent Model for Piezoelectric Actuators in Trajectory-Tracking Applications,” *IEEE/ASME Transactions on Mechatronics*, vol. 12, no. 2, pp. 134–142, Apr. 2007.

[74] Y. Chen, J. Qiu, J. Palacios, and E. C. Smith, “Tracking control of piezoelectric stack actuator using modified Prandtl–Ishlinskii model,” *Journal of Intelligent Material Systems and Structures*, vol. 24, no. 6, pp. 753–760, Apr. 2013.

[75] T. S. Low and W. Guo, “Modeling of a three-layer piezoelectric bimorph beam with hysteresis,” *Journal of Microelectromechanical Systems*, vol. 4, no. 4, pp. 230–237, Dec. 1995.

[76] M. Rakotondrabe, “Bouc–Wen modeling and inverse multiplicative structure to compensate hysteresis nonlinearity in piezoelectric actuators,” *IEEE Transactions on Automation Science and Engineering*, vol. 8, no. 2, pp. 428–431, Apr. 2011.

[77] J. Gan and X. Zhang, “An enhanced Bouc-Wen model for characterizing rate-dependent hysteresis of piezoelectric actuators,” *Review of Scientific Instruments*, vol. 89, no. 11, p. 115002, Nov. 2018.

[78] S. Kang, H. Wu, Y. Li, X. Yang, and J. Yao, “A Fractional-Order Normalized Bouc–Wen Model for Piezoelectric Hysteresis Nonlinearity,” *IEEE/ASME Transactions on Mechatronics*, vol. 27, no. 1, pp. 126–136, Feb. 2022.

[79] Y. Liu, C. Ni, D. Du, and N. Qi, “Learning Piezoelectric Actuator Dynamics Using a Hybrid Model Based on Maxwell-Slip and Gaussian Processes,” *IEEE/ASME Transactions on Mechatronics*, vol. 27, no. 2, pp. 725–732, Apr. 2022.

[80] J. Gan and X. Zhang, “A review of nonlinear hysteresis modeling and control of piezoelectric actuators,” *AIP Advances*, vol. 9, no. 4, p. 040702, Apr. 2019.

[81] F. Ma, H. Zhang, A. Bockstedte, G. C. Foliente, and P. Paevere, “Parameter analysis of the differential model of hysteresis,” *Journal of Applied Mechanics*, vol. 71, no. 3, pp. 342–349, Jun. 2004.

[82] L. Ma, Y. Shen, J. Li, H. Zheng, and T. Zou, “Modeling hysteresis for piezoelectric actuators,” *Journal of Intelligent Material Systems and Structures*, vol. 27, no. 10, pp. 1404–1411, Jun. 2016.

[83] F. Giraud and C. Giraud-Audine, *Piezoelectric Actuators: Vector Control Method*. Elsevier, 2019.

[84] M. Malm, M. Samman, and J. Serup, “In vivo skin elasticity of 22 anatomical sites,” *Skin Research and Technology*, vol. 1, no. 2, pp. 61–67, 1995.

[85] N. Nitta, T. Shiina, and E. Ueno, “Hysteresis parameter imaging of soft tissue under quasi-static deformation,” in *IEEE Symposium on Ultrasonics, 2003*, vol. 2, Oct. 2003, pp. 1606–1609 Vol.2.

[86] M. A. Meyers and K. K. Chawla, *Mechanical Behavior of Materials*, 2nd ed. Cambridge ; New York: Cambridge University Press, 2009.

[87] R. Lundström, H. Dahlqvist, M. Hagberg, and T. Nilsson, “Vibrotactile and thermal perception and its relation to finger skin thickness,” *Clin Neurophysiol Pract*, vol. 3, pp. 33–39, Feb. 2018.

[88] E. Yalcin, M. Akyuz, B. Onder, H. Unalan, and I. Degirmenci, “Skin thickness on bony prominences measured by ultrasonography in patients with spinal cord injury,” *J Spinal Cord Med*, vol. 36, no. 3, pp. 225–230, May 2013.

[89] J. F. J. Soetens, M. van Vijven, D. L. Bader, G. W. M. Peters, and C. W. J. Oomens, “A model of human skin under large amplitude oscillatory shear,” *Journal of the Mechanical Behavior of Biomedical Materials*, vol. 86, pp. 423–432, Oct. 2018.

[90] B. Babaei, A. J. Velasquez-Mao, S. Thomopoulos, E. L. Elson, S. D. Abramowitch, and G. M. Genin, “Discrete quasi-linear viscoelastic damping analysis of connective tissues, and the biomechanics of stretching,” *Journal of the Mechanical Behavior of Biomedical Materials*, vol. 69, pp. 193–202, May 2017.

[91] H. Alexander and T. Cook, “Variations with age in the mechanical properties of human skin in vivo,” *Journal of Tissue Viability*, vol. 16, no. 3, pp. 6–11, Aug. 2006.

[92] C. Pailler-Mattei, C. Guerret-Piécourt, H. Zahouani, and S. Nicoli, “Interpretation of the human skin biotribological behaviour after tape stripping,” *Journal of The Royal Society Interface*, vol. 8, no. 60, pp. 934–941, Jul. 2011.